New Dynamical Insights on the Global Behavior of Chaotic Attractors

A Thesis

Submitted to the Faculty

of

Drexel University

by

Timothy Douglas Jones

in partial fulfillment of the

requirements for the degree

of

Doctor of Philosophy

January 2012

Dedications

Dedicated to my mother, Linda Jones, to all of my nieces and nephews,

to 文錩,

and to Lisa Ferrara, Michel Vallieres, and Bob Gilmore for pushing me across the finish line.

Acknowledgments

Drexel University has given me the privilege to work with a great number of professionals from whom I've learned much and owe much in return.

Maryann Fitzpatrick and Wolfgang Nadler have been endlessly generous with their time in resources in both my roles as graduate student and Linux system administrator. My gratitude towards them is matched only by my deep respect and awe for their skills and knowledge. Lisa Ferrara was incalculable help when I taught labs, helping me overcome the limitations of inexperience by sharing her vast knowledge and experience. Since then she has been a wonderful mentor and has made my annual science parties, thrown for my nieces and nephews, much more engaging.

Janice Murray and Jackie Sampson have been endlessly patient and helpful. Janice's help with Dr. Gilmore and I in navigating the paper-work with our NSF grant has saved us much time and confusion. Laura D'Angelo has always been an encouraging force in my career, from the early days when Dr. Narducci was on my oral defense committee, to her current role as research coordinator. Our department was lucky that she stayed on board.

Drs. Daniel Cross has been an entertaining and informative colleague. Dr. Cross's mathematical background has been a source of inspiration which he has generously shared.

Dr. David Goldberg's early influence on my career has benefited me greatly along the way. He taught me, amongst other things, that science is an incremental effort that requires patience. I look forward to reading the many books he is sure to publish.

Dr. Michel Vallieres has provided consistent and lively challenges with computer troubles, but most of all, the breadth of his knowledge, from computational shop-talk, to physics, to mathematical finance, has lead to many great conversations that I will deeply miss.

Finally, of course, Dr. Robert Gilmore has provided his patience and knowledge month after month, and I thank him for the honor and privilege of working with him.

Table of Contents

List of Tables

List of Figures

Abstract

New Dynamical Insights on the Global Behavior of Chaotic Attractors
Timothy Douglas Jones
Robert Gilmore, Ph.D.

A paraphrase of Tolstoy that has become popular in the field of nonlinear dynamics is that while all linear systems are linear in the same way, all nonlinear systems are nonlinear in their own ways. Despite this being quite true, there can be found a number of universal features in nonlinear systems which unify them in ways that enhance our understanding of their behavior.

That nature is replete with nonlinear systems has proven to be a great challenge to our scientific understanding of the world. And while mathematics has proven to be apt at describing a multitude of physical phenomenon in the form of deterministic equations which describe future behavior based on a system's current state, it in and of itself held a rather shocking surprise which is now called Chaos. In Chaos we find deterministic systems which, due to our lack of omniscience, and the physical impossibility of building computers with infinite precision, become wildly unpredictable as they evolve in time. A number of new tools were developed to understand these systems, including a powerful program of topological analysis which has been completed for three dimensions. Yet, there still remains a number of unanswered dynamical questions about chaotic systems. Two such questions are the primary focus of this thesis.

The first question we will address is regarding the general shape of the strange attractor. Specifically, what can we learn about the shape of strange attractor from the dynamical equations without numerically integrating them? For example, the Rössler and Lorenz attractors have remarkably similar dynamical equations, and yet are topologically very distinct. There is no self-evident relation between the dynamical equations that describe a strange attractor and its shape in phase space. Previously, we only had the fixed points to act as general guides as to the shape of the attractor, but these point sets are not exceedingly descriptive. We will outline work done to find more interesting sets of points from the dynamical equations themselves, sets of points which provide a sort of

skeletal-structure for the strange attractors. We have examined these structures for a large number of strange attractors of varying topological nature.

The second question is one which has been treated by only a small number of researchers, and not as descriptively as we do here. When viewed in co-dimension-2 space (that is, two parameters of the attractor varied, all others kept constant), one finds some remarkable regular patterns in the mapping of the intensity of Lyapunov exponents. While progress has been made in addressing the origin of these shapes, there has not yet been a full explanation to the simple question: where do these patterns come from, and what do they tell us about the dynamical system? We will examine these patterns in detail and provide a broad explanatory mechanism for them, with a particular focus on the Rössler attractor. We will also show how these findings can be used to predict the occurrence of super-stable periodic orbits as the parameters of the attractor are varied, predictions that were previously unobtainable except by purely numerical means.

Chapter 1: Introduction and Background Information

> If, therefore, those cultivators of physical science from whom the intelligent public deduce their conception of the physicist, and whose style is recognized marking with a scientific stamp the doctrines they promulgate, are led in pursuit of the arcana of science to the study of the **singularities** and **instabilities**, rather than the continuities and stabilities of things, the promotion of natural knowledge may tend to remove that prejudice in favour of determinism which seems to arise from assuming that the physical science of the future is a mere magnified image of that of the past.
>
> —**James Clark Maxwell, 1873** [1]

A dynamical system is a mathematical formalization intended to represent a real physical process with exacting verisimilitude. In an idealized dynamical system, knowledge of the current state of a finite number of variables will give one exact knowledge of the precise conditions of that system at all times in the future and, in the best-case scenario, the state at all times in the past. The success of physics in formulating such idealized models, which reflected the world with great accuracy, lead to a philosophical vision of the universe in which it was supposed that, given enough time, the entire universe could be understood as a vast deterministic system. Just as a classic clock, if tuned properly, could accurately account for time through a complex series of mechanisms, and yet each mechanism could be described with a precise idealized model, so too, it was thought by many, the workings of the entire universe could be described and predicted with great accuracy if only we were to study all of the individual mechanisms that constitute it.

This "clockwork-vision" of the universe that was once popular with physicists and philosophers[1] was relaxed by necessity as thermodynamics and statistical mechanics attempted to bring determinism to the realm of gasses and liquids in the nineteenth century. In this branch of physics, knowing the past conditions from the current conditions was no longer a viable option, and predicting the

[1] Also called the Newtonian World View, though Newton was a notable opponent of this world-view for theological reasons.

future state of a thermodynamical system became a matter of both mechanics and statistics. Even so, the success of thermodynamics in describing the behavior of gasses and fluids didn't quite bring a closure to the classical vision of the universe, as we can see by the quote from Maxwell which began this chapter.

Such a closure was to come in the twentieth century with two major revolutions in how the physics community saw determinism. Quantum mechanics undermined the vision of determinism at the very small scales of the subatomic realm. Long after these revolutionary insights became conventional physics, a third revolution, this time originating from the very heart of dynamics, undermined the classical vision of predictable determinism for what is now considered the classical scale.

This later revolution, chaos theory, is central to the topics of this thesis. Chaos is, essentially, apparent disorder from deterministic dynamics. What we mean by this will be made precise.

Research in chaos theory is typically an effort to understand complex systems in such a way that behavior that seems superficially mysterious and unpredictable can be cast more accurately in precise deterministic form. Although we can never return to the paradise of clockwork-determinism, we can at least try to make sense of the far more complex, and far more interesting universe that physicist have found themselves working with once the "prejudice in favour of determinism" was shed once and for all.

This thesis approaches this effort in two ways. We first look at mathematical objects called strange attractors, finding an analytical way to predict the major features of their shapes without the need to computationally integrate their dynamical equations. We do this by adopting definitions of vortex curves from fluid mechanics.

Then, we approach strange attractors from a much broader perspective, considering an open question about features they exhibit in their parameter space. In particular, a large set of strange attractors exhibits something called a spiral hub in their parameter space, a round, nearly symmetrical shape in which bands of stability spiral inwards towards a center point. We present here a dynamical and topological explanation for these shapes, locating their origin in the topology and route to chaos that these systems exhibit. Furthermore, we locate the precise locations of asymmetry in this spiral structure and explain their origin, offering for the first time a comprehensive explanation for these features.

1.1 Historical Background

Before the name "chaos" took root as accepted convention, alternative names had been used throughout the literature, including "dynamical stochasticity", "self-generated noise", "intrinsic stochasticity", and "Hamiltonian stochasticity" [2]. The problem with these names is that they seem to attempt to define the phenomenon of chaos using words that originate from pre-chaos classical dynamics. For example, "self-generated noise" fails since the term "noise" implies a lack of determinism. On the other hand, the term "Hamiltonian stochasticity" is doubly-loaded, first with the term "Hamiltonian" which seems to preclude dissipative systems, and the term stochasticity which again wrongly implies a lack of determinism. The term chaos, short for "deterministic chaos" seems to be the better fit because it is a new term[2] and thus can be made as inclusive as necessary.

The root of modern chaos theory is generally traced back to the works of Henri Poincaré on the three-body problem (1890) [3], where he discovered the existence of nonperiodic orbits. His work on this problem introduced the concept of approaching a topic qualitatively rather than just quantitatively [4]. Poincaré's qualitative geometrical techniques were adopted shortly thereafter by Jacque Hadamard in his landmark analysis of non-Euclidean billards (1898) [5]. It was Hadamard who was first to note the existence of dynamical systems which behaved with sensitivity to initial conditions[3] [5–7], and who first introduced the use of symbolic dynamics in the very same publication [7–10]. Poincaré later championed the concept of sensitivity to initial conditions, and his geometrical methods were developed further in the twentieth century by Birkhoff with his ergodic theorem, and Kolmogorov, Arnol'd, and Moser with KAM-theory [2, 4], amoungst others. Their exploration of complex behavior found in Hamiltonian mechanics is not directly related to the type of systems which we will study, which happen to be dissipative. From a more experimental point of view, Van der Pol had observed "irregular noise" in approximately 1927 [11, 12], but it was not

[2]Boltzmann used the term chaos in statistical thermodynamics, but not as we now use it today. [2]
[3]Physicists too often attribute this finding, incorrectly, to Poincaré.

recognized as a significant new phenomenon until a few decades later with the works of Cartwright and Littlewood. They discovered chaos in differential equations modeling problems arising in radio and radar engineering and later pursued chaos-like behavior in forced non-autonomous systems such as the Van der Pol model [13–16][4]. More famous is the work of Lorenz in 1963 [17] who rediscovered the nonperiodicity and sensitivity that Poincaré and Hadamard has previously found. This time, the discovery was made using the quantitative output of a computational integration of a simplified three dimensional model of convection roles in Earth's atmosphere [4, 18]. He discovered that the output to his simulations, when plotted in three dimensions, produced a fractal[5] attractor with a characteristic butterfly shape. This object was later classified as a "strange attractor", an attractor with non-integer (fractal) dimension, a term coined by Ruelle and Takens in 1971 [19] in the context of their seminal work on fluid dynamics. Takens would later introduce a key theorem for the embeddings of observed time-series in higher dimensions to reconstruct the essence of the strange attractor of an experimental system [20], and recent work has identified topological invariants and degrees of freedom for such embeddings [21, 22].

Another remarkable development was the analysis of chaos in maps, best typified by the works of Parry [23, 24] and Sharkovsky in the 1960s [25–28], Li and Yorke in 1975[6] [29] who seem to be the first to use the term "chaos" as it is currently understood [2], Metropolis et al. who produced a seminal paper exploring stable limit sets in unimodal maps in 1973 [30], Milnor and Thurston who developed Kneading Theory for unimodal maps [31] in 1977, and May who, in 1976 [32], published a landmark paper in Nature in which he explored the chaotic dynamics that came from the discretized version of the Logistic function.

These remarkable findings about chaotic maps were to hold even greater surprises when Feigenbaum found that patterns of universality applied to chaotic maps [33], and his introduction of renormalization group ideas into chaos helped put the field on more solid mathematical ground.

In 1967, Smale published a seminal paper [34] on a map now known as the Smale Horseshoe

[4]Cartwright and Littlewood strongly endorsed the conclusion that both topological and analytical methods were necessary to understand nonlinear dynamics, which can be seen as an extension of Poincaré's original program.

[5]By fractal we mean that it had a non-integer dimension due to the complexity of its overall shape

[6]The work of Li and Yorke turns out to be a weaker variation of the work of Sharkovsky, but due to the barriers of communication between Soviet and Western scientist during the cold war, the former were unaware of the work of the latter.

Map, which has been called a hallmark of chaos. We will return to this map in greater detail later in this chapter as it provides a broad explanatory mechanism for the most common route to chaos in dissipative systems, including the ones that we focus on in this thesis.

From the 1970s forward, the number of publications about chaos theory expanded rapidly, and a full account of the history of the field in the latter decades of the twentieth century is beyond the scope of this chapter. Instead, we will discuss more details of the historical background of chaos theory in later chapters as it becomes directly pertinent.

In this chapter, we will focus on introducing the fundamental concepts from dynamics and chaos theory which will be the foundation for the new research we present in later chapters.

1.2 A Definition of Chaos for Maps

Before we can discuss chaos in greater detail, we need to settle on a more rigorous definition of chaos. We adopt the most common definition in the literature [35–37] (though see, e.g., [38, 39] for technical objections which do not affect our results, and [4, 40, 41] for less technical, more intuitive definitions).

A mapping $f : J \to J$ is topologically transitive if for any open sets $U, V \subset J \; \exists \; k > 0 \; : \; f^k(U) \cap V \neq \emptyset$. That is, any open subinterval will, after enough mappings, be mapped into, in part or whole, any other open subinterval. We say that f exhibits sensitivity to initial conditions if $\exists \delta > 0 \; : \; \forall x \in J$, and any neighborhood N of x, $\exists \; y \in N, n \geq 0 \; : \; \|f^n(x) - f^n(y)\| > \delta$. That is, if we select any two points, one as arbitrarily close to the other as we wish, we will find them separated by substantially larger distances given enough iterations of the map.

A mapping is chaotic if it is topologically transitive, exhibits sensitivity to initial conditions, and periodic points are dense in its domain/range. A subset of an interval is dense in that interval if its closure is the entire interval. A point is in the closure of an interval if every open neighborhood centered at that point contains a point of the interval, even though that point itself may not be in the set. In simpler terms, this condition says that for a mapping to be chaotic, we require that the location of its periodic orbits be distributed in such a way that for any randomly chosen point on the interval, we will find ourselves arbitrarily close to at least one periodic orbit (which may be stable or unstable). It can be shown that for a range of parameters, the Logistic Map and all topologically conjugate unimodal maps satisfy all of the above conditions [35–37] for some parameter values.

There exist a wide number of mappings which exhibit chaotic behavior, with a varying level of complexity. For this introduction, we focus only on unimodal maps, and in Chapter Five we will review the literature on bimodal maps, where both unimodal and bimodal maps will play an important part in Chapter Six. While maps may represent simpler systems than do flows, we will find that they offer a rich insight into chaos with tremendous implications for flows. In fact, for flows which are highly dissipative, i.e. flows which are non-Hamiltonian, one finds a partial conjugacy with unimodal maps at lower parameters. The details of this point will be expanded upon in Chapter Six.

Of all the unimodal maps, the Logistic Map is the most widely studied, and we focus on it in the next sections.

1.3 Dynamics of Unimodal Maps of the Interval Onto Itself

It is quite remarkable that the dynamics of one dimensional maps can lead to the existence of chaos. What is even more remarkable is that these dynamics also govern much of the behavior of higher dimensional strange attractors. This later point will be discussed in greater detail in the next chapters.

The dynamics of the Rössler system [42], at lower parameter values (what we mean by lower parameter values will be made clear), can be partially described by a unimodal-type return map. As the Rössler system becomes more complicated with increasing parameter, which is to say, as the branched manifold describing the Rössler attractor [36] acquires additional branches[7], the return map becomes first cubic-type, and so on. The mathematics of the unimodal (one critical point) and cubic-type mappings (two critical points) are well developed and will provide insight into the dynamical behavior of attractors which exhibit unimodal and cubic-type return-maps in certain parameter regimes. In this chapter, we introduce the basics of unimodal maps.

[7]We use the term branches for both the branched manifold and the return maps, such that for the latter, a branch is equivalent to a "lap", which is a term used in some of the mathematics literature on unimodal maps [31].

1.3.1 The Logistic function

Mathematical modeling of species populations, first introduced in 1798 by Malthus who described such growth as exponential [43, 44], lead to the formulation of the Logistic function, which was given its name by Verhulst 1838 [45]. Presented as a statistical law for population growth, it was not generally accepted as scientifically valid when it first appeared [46], this being long before the blossoming of the field of chaos theory. The twentieth century was a kinder one for the Logistic function. First, Lotka rediscovered it in 1910 [47, 48] as a form of what we now call the predator-prey model, followed by Pearl and Reed [49], who, working from a polynomial best-fit model of observed population growth in the United States by Pritchett [50], rediscover the logistic function and prematurely declare it a universal law [44].

When experiments with bacterial strains in non-renewed mediums [51] found growth which couldn't be fitted with exponential or Logistic functions, Volterra modified the Logistic function to an integro-differential form to account for the poisoning of environment [52], work later extended by Kostitzin [53] in 1937. This modified form of the Logistic function, called the Volterra-Kostitzin integro-differential model of population dynamics, continues to be used in population modeling and economics, amongst other fields [46].

1.3.2 Background

However, it is the simpler form of the Logistic function that we will find useful for our discussions. For historical interest, we will trace the independent derivation of the Logistic function by Pearl and Reed [49]. They begin by citing the least-squares polynomial best-fit that Pritchett [50] found by analyzing US census data from 1790 to 1880. His fit took the form,

$$P(t) = A + Bt + Ct^2 + Dt^3 \tag{1.1}$$

where P represent the total population, t is time since 1790, and $\{A, B, C, D\}$ are parameters. Pearle et al. [54] had previously found that a logarithmic curve such as,

$$P(t) = a + bt + ct^2 + d \log t \tag{1.2}$$

provided an excellent fit to growth rates of the aquatic plant Ceratophyllum, and noted that later research found it to fit a wide range of growth curves, such as the milk production by age of cows and brain growth in rats [55]. They speculated that a curve of this type might better approximate the growth rate recorded in US census records than that of a simple third-order polynomial[8]. After fitting an updated census data set to both their logarithmic model and Pritchett's polynomial model, they were able to show that indeed the logarithmic model was approximately twice as accurate.

But then they also note that if their model were extended to the year 3000 C.E., it predicts that the United States would have a population of $11,822,000,000$ persons, a population density of 3116 persons per square mile[9]. As they noted, this figure represents an unlikely outcome, as natural resources are not infinite in supply[10] This seemingly absurd prediction motivated their rediscovery of the Logistic function.

They proposed that a more accurate model of population growth should account for:

- The magnitude of the population existing at a reference time t.
- The remaining capacity of the environment to support further population increases.

and should fulfill the following conditions:

- Asymptotic to line $\lim_{t \to \infty} P(t) = P_{max}$.
- Asymptotic to line $\lim_{t \to -\infty} P(t) = P_{min} = 0$.

[8]Pearl would later attempt the leap from speculation to positing that the Logistic function was a universal law of biological growth, an unwarranted leap that slowed the acceptance of the Logistic function in some quarters as a valid scientific model [44].

[9]The actual number they cite is 3968 persons per square mile, but since the US has gained a number of states since 1920, including the sparsely populated Alaska, I've adjusted the figure accordingly.

[10]Though perhaps this seems slightly less absurd today, with a global population of nearly seven billion and increasingly sophisticated agricultural technologies; the global population in 1920 is estimated to have been approximately 1.86 billion [56].

- An inflection point (where population growth starts to slow as it approaches P_{max}) at some time $t = \alpha$ with $P(\alpha) = \beta < P_{max}$.

- Concave upwards for $t < \alpha$, Concave down for $t > \alpha$ (i.e. $\frac{d^2P(t)}{dt^2} > 0$ for $t < \alpha$ and $\frac{d^2P(t)}{dt^2} < 0$ for $t > \alpha$).

- $P(t)$ is continuous with $\frac{dP(t)}{dt} = 0$ only in the limits of $t = \pm\infty$.

One such an equation is,

$$P(t) = \frac{be^{at}}{1 + ce^{at}}, \{a, b, c\} > 0 \tag{1.3}$$

The derivative of this function is,

$$\frac{dP(t)}{dt} = \frac{ay(b - cy)}{b} \tag{1.4}$$

As a final note, we can say nearly one hundred years later that none of the three population models proved to be accurate in the long term. The Logistic model comes closest to approximating US population growth well into the twentieth century, but adjusted to 1900, begins to underestimate US population around 1950 (Figure 1.1). However, to their credit, Pearl and Reed anticipate this failure, indicating that such models need to be modified based on changes in historical trends.

1.3.3 Unimodal Maps of the Interval

Maps Conjugate to the Logistic Map

It 1976, May [32] published an article introducing the Logistic Map as a sort of discreetization (via Euler-method) of the Logistic function of the form,

$$y(t+1) = y(t)\left(1 + \frac{ay(t)(b - cy(t))}{b}\right) \tag{1.5}$$

This form can be converted through an affine transformation [37, 57] to the standard form of the class of Logistic maps,

$$L(x_n, r) = x_{n+1} \equiv rx_n(1 - x_n) \tag{1.6}$$

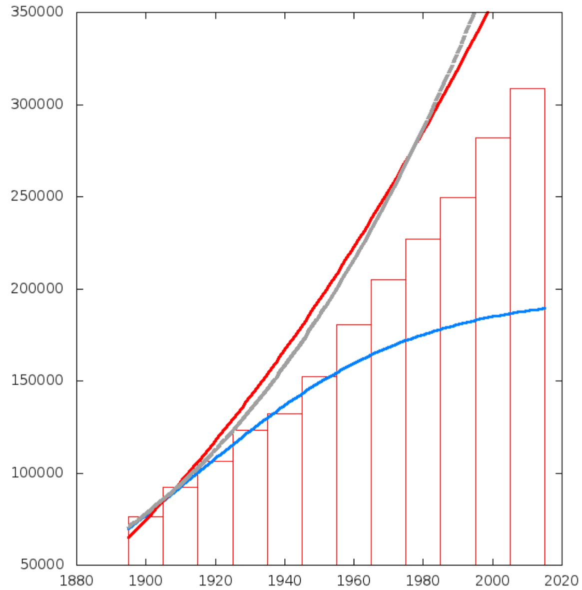

Figure 1.1: Population models of Pearl/ Reed, and Pritchett, verses census data. (Color online). The Logistic model is remarkably accurate up to the census data for 1950 but then greatly underestimates the actual population thereafter. Pritchett's cubic model (dashed gray line) and Pearl and Reed's log model (red line) both overestimate the population. Models have been adjusted to each fit the data for 1900 and to compensate for apparent rounding errors in the original works.

This map seems to be, by far, the most commonly studied unimodal map, and this is why we have chosen to focus much of our attention, in discussing unimodal maps, to the Logistic Map. However, for convenience, we now use the fact that the Logistic Map is just one of a class of maps of the unimodal type, and is in fact topologically conjugate to generic maps of the form

$$x_{n+1} = x_n^2 + \lambda \tag{1.7}$$

where λ is a generic unimodal parameter which will not necessarily have a one-to-one relation with the lambda of the Logistic Map. This means that the dynamics found in Equation 1.6 will be the same as those found in Equation 1.7. All maps which are smooth, continuous, and unimodal, will exhibit the same order of orbit formation, with the same route to chaos via a period-doubling cascade. Thus in exploring the dynamics of unimodal maps, we have the freedom to chose whichever conjugate map we may prefer. This point of conjugacy will be helpful in Chapter Six, and to emphasize the point here, we will introduce some of the basic details about unimodal maps using both Equations 1.6 and 1.7.

Because the critical point of the map of Equation 1.7 is located at $x = 0$, it is sometimes more convenient to use this form when discussing the dynamical properties of unimodal maps.

Bifurcations in Unimodal Maps

In order to sketch the basic behavior of these types of mappings, we briefly consider bifurcations in the quadratic family $Q_\lambda(x) = x^2 + \lambda$. We will discuss bifurcation in more detail later, but in this context, a bifurcation involves the sudden change in the behavior of a system from one state to another that happens over a small change in a parameter. We can speak of period-doubling bifurcations which involve a periodic orbit suddenly doubling in period, we can speak of a saddle-node bifurcation where the sudden intersection of two nullclines or the transition of a solution from imaginary to real brings about the appearance of a doubly degenerate fixed point which then splits into two non-degenerate fixed points as the bifurcation parameter is increased.

We find the fixed points via $x^2 + \lambda = x$ where,

$$x_f = \frac{1 \pm \sqrt{1 - 4\lambda}}{2} \tag{1.8}$$

This is only real for $\lambda < 1/4$:

We note the right-hand fixed point will always be repulsive since $Q'_\lambda(x) = 2x$ and the right-hand fixed point is greater than 1/2 for $\lambda \in (-\infty, 1/4)$. Thus we have no fixed points for $\lambda > 1/4$ and we focus on $\lambda \in (-\infty, 1/4)$. One also finds that $Q'_\lambda(x) = 2x$, $Q''_\lambda(x) = 2$, $\frac{\partial Q_\lambda(x)}{\partial \lambda} = 1$, $Q^2_\lambda(x) = (x^2 + \lambda)^2 + \lambda = x^4 + 2x^2\lambda + \lambda^2 + \lambda$, and $\frac{\partial (Q^2_\lambda)'(x)}{\partial \lambda} = 4x$

For mappings of the interval, saddle-node bifurcation are found under the following conditions [35–37]:

1. $Q_\lambda(x_f) = x_f$. A newly formed fixed point will initially map to itself.

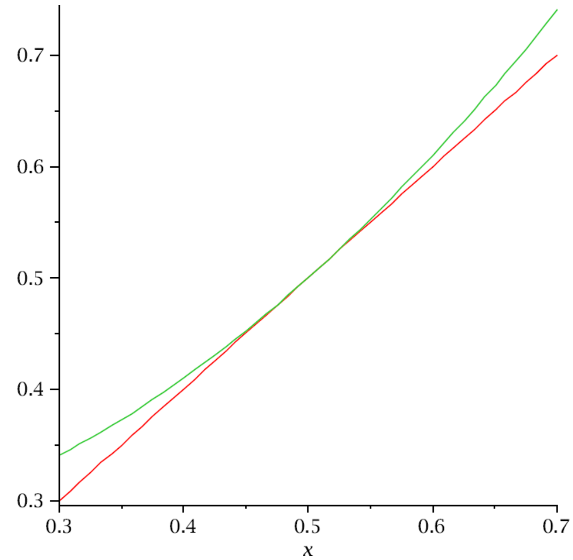

Figure 1.2: For $\lambda = 0.25$, red line is the line $x = y$, green line is the plot of $Q_{1/4}$.

2. $Q'_\lambda(x_f) = 1$. For maps, Hyperbolic fixed points are such that the $f'(p) \neq \pm 1$. These bifurcations only occur for non-hyperbolic fixed points, which this condition entails.

3. $Q''_\lambda(0) \neq 0$. The signs of $Q''_\lambda(0)$ and $\frac{\partial Q_\lambda}{\partial \lambda}\|_{\lambda=\lambda_0}(0)$ determine the direction of the bifurcation. See Devaney [35] for technical details.

4. $\frac{\partial Q_\lambda}{\partial \lambda}\|_{\lambda=\lambda_0}(0) \neq 0$

For the mapping Q_λ, we will have a saddle-node bifurcation as follows:

1. $Q_\lambda(x_f) = x_f$ is satisfied for $x_f = (1 \pm \sqrt{1 - 4\lambda})/2$.

2. The second condition is satisfied at $\lambda = 1/4$, where $x_f = 1/2$.

3. $Q''_\lambda \neq 0$ is always satisfied since $Q''_\lambda = 2$

4. $\frac{\partial Q_\lambda}{\partial \lambda}\|_{\lambda=\lambda_0}(0) \neq 0$ is satisfied for all $x \neq 0$

Thus we have a saddle-node bifurcation at $\lambda = 1/4$, where $x_f = 1/2$, a doubly degenerate period one orbit.

The initial starting point of the first period-doubling bifurcation cascade is found under the following conditions [35–37]:

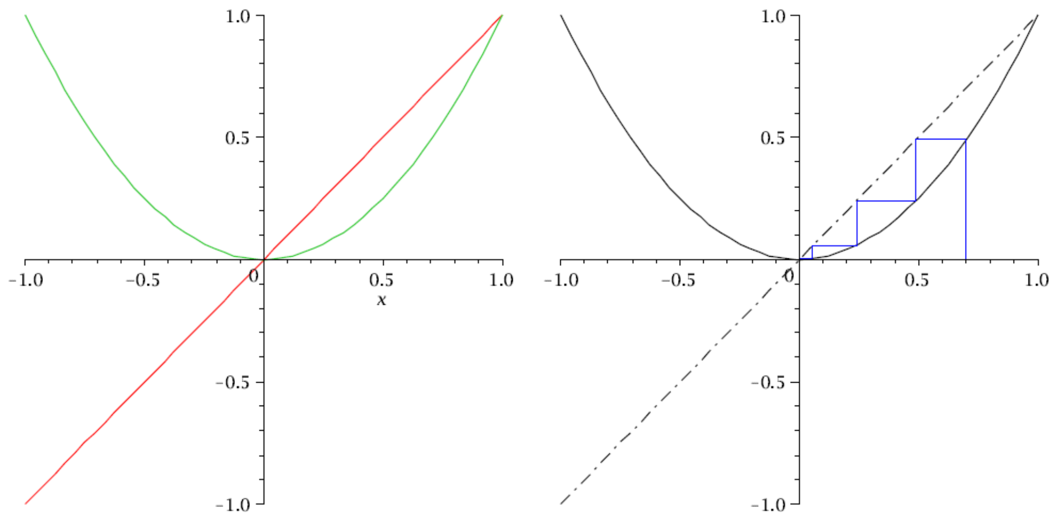

Figure 1.3: For $\lambda = 0$; the right figure represents the Verhulst (or cobweb) diagram for the forward orbit of the point $x_0 = 0.7$. One begins with a point x_0 and traces it to the graph of Q_λ; from that intersection, a line is drawn to the $x = y$ line; from that intersection a line is drawn upwards or downwards back to the function graph, and so on.

1. $Q_\lambda(x_f) = x_f$
2. $Q'_{\lambda_0}(x_f) = -1$
3. $\frac{\partial (Q^2_\lambda)'}{\partial \lambda} \|_{\lambda=\lambda_0}(0) \neq 0$

The conditions are fulfilled for the Q_λ mapping as follows:

1. $Q_\lambda(x_f) = x_f$ for all λ in an interval about λ_0.
2. $Q'_{\lambda_0}(x_f) = -1$. Since we have that $Q'_\lambda(x) = 2x$, this can only occur at $x = -1/2$. Thus we must solve the equation, $\sqrt{1-4\lambda} = 2$ giving $1 - 4\lambda = 4$, that is, $\lambda = -3/4$.
3. $\frac{\partial (Q^2_\lambda)'}{\partial \lambda} \|_{\lambda=\lambda_0}(0) \neq 0$. We found that $\frac{\partial (Q^2_\lambda)'(x)}{\partial \lambda} = 4x$. This also is satisfied at $x = -1/2$, and we find that $Q^2_\lambda(-1/2) = -1/2$.

Standard Logistic Map

The Logistic map will be the basis from which we discuss unimodal maps of the type that will later become important in our research with the Rössler attractor. For convenience, we shall drop the n

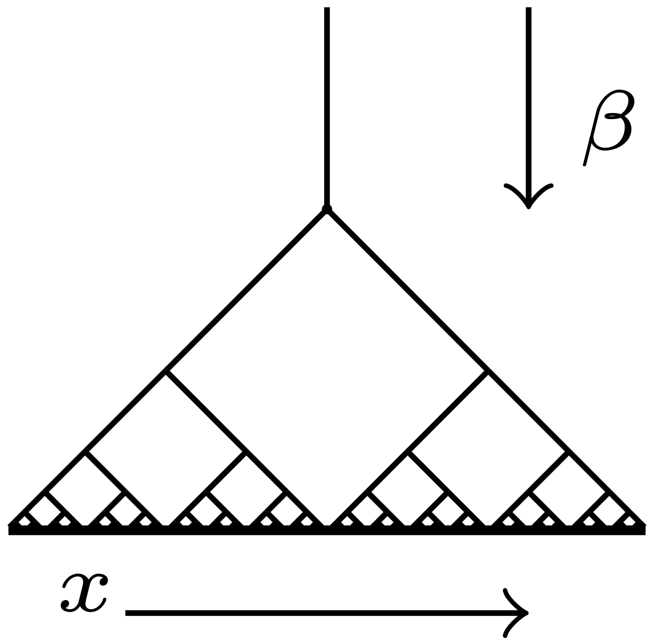

Figure 1.4: Graphical representation of a period-doubling cascade which accumulates at the Feigenbaum point leading to a fully chaotic system as the bifurcation parameter β is changed.

subscripts on the map and write it as [35],

$$F_r(x) = rx(1-x) \tag{1.9}$$

The Stability of the Logistic Map

We define the forward orbit of a point $x \in (0,1)$ as $F_r^n(x), n \in \mathbf{Z}$. If a point satisfies $x = F_r^1(x)$, x is called a fixed point, and if $x = F_r^p(x)$, $p \in \mathbf{Z}$, with p the smallest possible value (i.e. relatively prime), then the orbit of x is a periodic point of period p, denoted $Per_p(F_r)$. A point is called eventually periodic if its forward orbit ends up in a periodic orbit p, and all such points comprise the stable set of that point, $W^s(p)$. For non-periodic fixed points, x is forward asymptotic to x_p if $\lim_{i\to\infty} \|F_r^i(x) - F_r^i(x_p)\| = 0$, and is backwards asymptotic to p if $\lim_{i\to-\infty} \|F_r^i(x) - F_r^i(x_p)\| = 0$. Such backwards (forward) asymptotic points comprise the unstable (stable) set of x_p, $W^u(x_p)$ $(W^s(x_p))$.

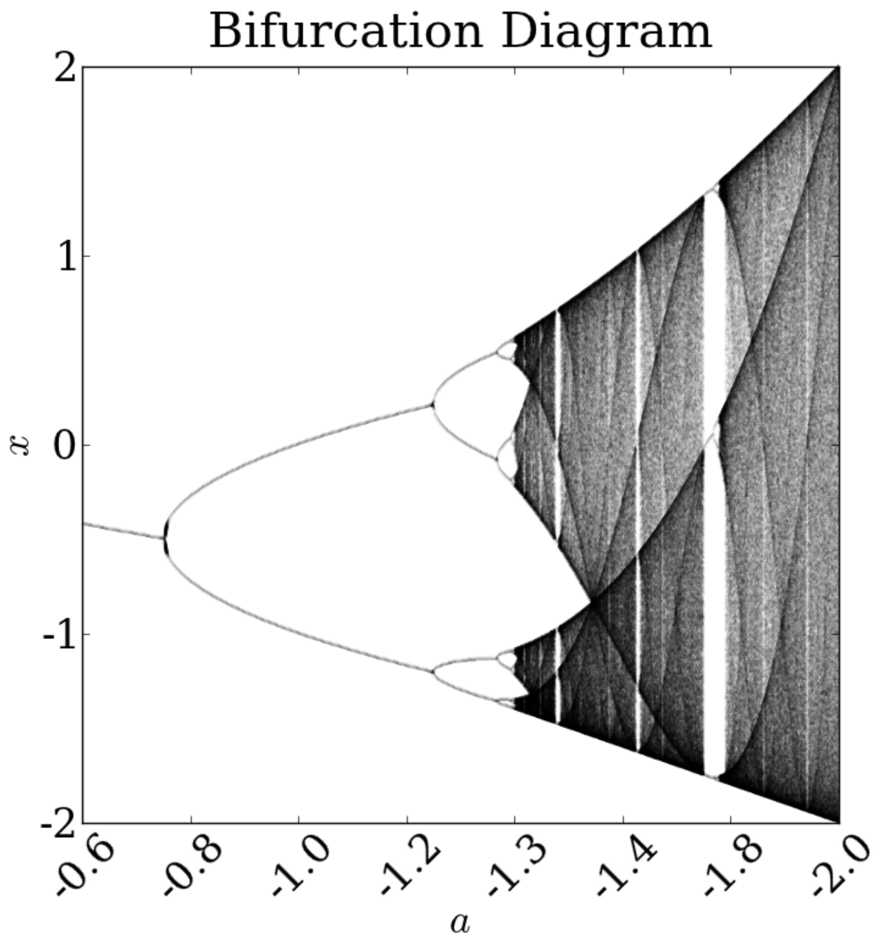

Figure 1.5: a (x-axis) verses x bifurcation diagram. The first period-doubling bifurcation happens at $a = -3/4$ for Q_a.

If $dF_r(x)/dx = 0$, x is called a critical point. A periodic point x_p is hyperbolic if $\|(F^p)'(x_p)\| \neq 1$, where here the prime mark denotes derivation with respect to the x variable.

Equation 1.9 has fixed points $x = 0$ and $x = (r-1)/r$ with a critical point at $x_{crit} = 1/2$ (the first derivative of the map is zero here). All orbits outside of the interval $[0, 1]$ escape to infinity. Having thus placed bounds of interest on the x interval, we proceed to place similar bounds on the parameter interval.

For r, the obvious minimum bound will be $r = 1$, which is the point where both fixed points merge into one (inverse saddle-node bifurcation). The upper bound of interest for r can be obtained by finding the point where $F_{r_{max}}(x_{crit}) = 1$, that is, $r_{max} = 4$. For $r > r_{max}$, almost all initial conditions escape to $-\infty$, and what remains on the interval $[0, 1]$ constitutes a chaotic repellor.

1.4 Symbolic dynamics of the Logistic Map

Symbolic dynamics is a means of simplifying the essential dynamical features of a system in a systematic way. We will find that symbolic dynamics is quite a useful tool that has tremendous explanatory power for the dynamics of Logistic type mappings.

Historical background

The first use of symbolic dynamics in the scientific literature [7–10] was by Jacques Hadamard in 1898 [5] to describe geodesic flows on surfaces of negative curvature in the context of dynamical systems (a model also known in the context of quantum mechanics as the Hadamard-Gutzwiller model [58]). Hadamard interpreted his model as non-Euclidean billiards [59], and using the qualitative techniques pioneered by Poincaré, and was also the first to point out the significance of the phenomenon of sensitivity to initial conditions [5–7]. In 1938 and 1940, Morse and Hedlund [60, 61] named [9, 10] and gave the first systematic abstract treatment to the subject of symbolic dynamics. The application of symbolic dynamics to dynamical systems was further developed in the 1970s by Bowen, Ruelle, and Sinai [62–64], who applied symbolic dynamics to dynamical systems which satisfy Smale's axiom-A.

In the early 1960s, Parry applied symbolic dynamics and Markov partitions to mappings of the unit interval [23, 24], work that was later extended by Metropolis et al. [30] and Milnor and Thurston [31][11]. Crutchfield and Packard [65], inspired by the work of Shaw [66], first studied the topological and metric entropies of the Logistic Equation using symbolic dynamics.

Symbolic Dynamics and the Logistic Map

A unimodal map of an interval I can be divided into two or more partitions (laps in Milnor and Thurston's terminology) by dividing the interval into sections on which the map is either monotonically increasing or decreasing. The critical point of the map is a natural dividing point for these partitions and is the dividing point that leads to the smallest number of possible partitions (two). We then label each partition with a *symbol*. In the case of two partitions, 0 and 1 are natural choices,

[11] Though the reference for Milnor and Thurston is dated to 1988, their work was actually done by 1977 and circulated widely in preprints [65] but wasn't formally published until 1988.

with all points on the interval I less than the critical point defined as I_0, and the remaining interval labeled I_1. The symbol for each position x is defined as $s(x) = 0 \iff x \in I_0,\ s(x) = 1 \iff x \in I_1$. Orbits of a point x of the logistic map, defined by the sequence, $\{x, F_r(x), F_r^2(x), \cdots, F_r^n(x), \cdots\}$ are associated with an corresponding sequence of symbols,

$$\Sigma(x) = \{s(x), s(F_r(x)), s(F_r^2(x)), \cdots, s(F_r^n(x)), \cdots\} \tag{1.10}$$

The mapping itself is replaced with a shift operator denoted by $\sigma(s) = s' = s(F_r(x))$ where $s = s(x)$. The projection operator is defined as $\pi\left(\cdots s_{-1}, s_0, s_1, \cdots\right) = \bigcap_{i=-\infty}^{\infty} F^{-i} I_{s_i}$. The operator projects the symbol sequence of an orbit onto the interval via the intersection of the backwards and forwards iterates of the intervals corresponding to the symbol number (i.e. $0 \to I_0$ and $1 \to I_1$). It can be shown [31, 36, 65] that for the Logistic Map under a partition taken at the critical point, we have a faithful representation between the mapping and the symbolic dynamics such that,

$$\begin{array}{ccc} \Sigma_{F_r} & \xrightarrow[\sigma_f]{} & \Sigma_{F_r} \\ \Big\downarrow \pi & & \Big\downarrow \pi \\ I & \xrightarrow[F_r]{} & I \end{array} \tag{1.11}$$

is commutable, or more simply put, $x_1 \neq x_2 \iff \Sigma(x_1) \neq \Sigma(x_2)$ [36].

Symbolic dynamics offers a set of tools which can be used to study these systems in greater detail. However, for the purposes of this thesis, we only need symbolic dynamics in order to distinguish between orbits of the same period. For example, in unimodal maps, there are three pairs of unstable/stable period five orbits, where the stable pairs are identified as $C1011$, $C1001$, and $C1000$.

Number of Stable Periodic Orbits

A superstable orbit is an orbit which contains the critical point of the map. Since the stability of an orbit is proportional to the product of the derivatives of the map at each point on the orbit, and since the derivative of the critical point is zero, such orbits are called superstable. The orbit will remain stable if perturbed slightly off of the critical point, but it will no longer be superstable. Since the unimodal maps only have one critical point, such maps can only have one stable or superstable periodic orbit at a time. As we will discuss in Chapter Five, bimodal maps which have two critical points can contain two stable periodic orbits simultaneously, albeit in different basins of attraction (i.e. some initial values will lead to one stable period, others initial values will lead to the other stable period), one for each critical point.

1.5 Discussion

The dynamics of unimodal mappings is a well-studied topic, and a full description of the mathematics that define the Logistic map is well beyond the scope of this thesis. The behavior of bimodal maps is richer still, and will be introduced in Chapter Five. We will examine an example of a two-dimensional chaos map later in this chapter.

We now turn our attention to chaos in flows, and find that for a particular class of chaotic flows, an analysis of their behavior will lead us right back to chaotic mappings.

1.6 Basic flow Dynamics and a Definition of Chaos

A typical dynamical system can be described by a set of ordinary differential equations (ODE),

$$\frac{d\vec{x}}{dt} = \vec{F}\left(\vec{x}, \alpha\right) \tag{1.12}$$

where $\vec{x}(t)$ is a state vector representing the state of the system at time t, and α is a set of parameters that characterize a class of systems. We will often speak of two different spaces for such systems. The first space we call *state-space* in $\mathbb{R}^n$ where n is the dimension of the system, which contains the state vectors $\vec{x}$, and where parameters are held fixed. In the use of the term *state-space*, we differ in meaning from the term typically used in Physics, that of the complex Hilbert space of quantum mechanics. Technically, we should more properly use the term *phase-space*, a term introduced by Willard Gibbs in 1901. However, *state-space* has become an unstated conventional term, and so we use it to mean *phase-space* throughout this thesis.

The second space is called *parameter-space* in $\mathbb{R}^k$, where k is the number of free parameters. Typically, for a system with k parameters, the interesting behavior of the system occurs in only a small subspace. This space represents a more global perspective of a dynamical system, populated by a multitude of bifurcations and, in chaotic systems, punctuated by regions of chaos and stability which characterize the system and are seen as a global manifestation of the perestroikas of the orbits [36].

That is, the only way to fully understand a chaotic system is to consider the union of these two spaces[12]. For example, we will find that the Rössler system has a three-dimensional state-space and a three-dimensional parameter-space. The union of these spaces would be a six-dimensional space in which, for each point in parameter space, we have a corresponding three-dimensional state-space. The reason for us making this point will become clear in Chapter Six.

1.6.1 Dynamics and State-Space

If the equation F is linear for all $x \in \mathbb{R}^n$, we call it a linear ODE [67]. Otherwise it is a nonlinear ODE. All chaotic systems result from nonlinear ODEs, though not all nolinear ODEs result in chaos. If a dynamical system which can be described by Equation 1.12 is explicitly dependent upon time, that is, if $\partial F/\partial t \neq 0$, we call this system nonautonomous, and otherwise we call it autonomous. In later chapters, we will be considering both types of systems, but for now we focus only on autonomous systems.

It is often the case that first order ODEs can be expressed as a set of second order ODEs and vice versa. For example, we consider the nonlinear oscillator, a simplification of the simple pendulum equation, described by

$$\ddot{x} = -\sin(x) \tag{1.13}$$

We can write an equivalent system of two equations:

$$\dot{\vec{x}} = \vec{F}(\vec{x}) = \left\{ \begin{array}{ccc} \dot{x_1} & = & x_2, \\ \dot{x_2} & = & -\sin(x_1) \end{array} \right\} \tag{1.14}$$

[12] Technically, this might be seen as simply pursuing the definition of phase space to its logical conclusion, but conventionally, phase space has been used to describe the dynamics where parameters are held fixed.

Fixed Points

One of the key findings of Poincaré's qualitative program was a focus on the fixed points of a system. For the above example, we can find the fixed points where $\vec{F}(\vec{x}) = 0$, which we write as $\vec{F}(\vec{\bar{x}}) = 0$ for the fixed points $\vec{\bar{x}}$. It is most clear that $\vec{\bar{x}}$ must take the form $(\bar{x}_1, 0)$ since $\dot{x}_1 = x_2 = 0$. Our other equation, $\dot{x}_2 = -\sin(\bar{x}_1)$ is satisfied for $x_1 = n\pi$, $n \in \mathbb{Z}$. Thus we will have fixed points at all points that satisfy $\bar{x} = (n\pi, 0),\ n \in \mathbb{Z}$.

We now introduce the typical change of coordinates, $\vec{\zeta} = \vec{x} - \vec{\bar{x}}$, so that $\dot{\vec{\zeta}} = \dot{\vec{x}}$. The Taylor expansion is

$$\dot{\vec{\zeta}} = F(\vec{\bar{x}}) + DF(\vec{\bar{x}})\hat{\zeta} + \mathcal{O}(\zeta^2) \approx DF(\vec{\bar{x}})\hat{\zeta}$$

The second term on the right hand side of this equation includes a term which is called the Jacobian of the system, denoted as,

$$J = DF(\vec{\bar{x}}) \tag{1.15}$$

With this linearization we can compute the eigenvalues of the linearized matrix at the fixed points:

$$DF(\vec{\bar{x}}) = \begin{pmatrix} 0 & 1 \\ -\cos(n\pi) & 0 \end{pmatrix} = \begin{cases} \begin{pmatrix} 0 & 1 \\ -1 & 0 \end{pmatrix} & \text{n even} \implies \lambda^2 + 1 = 0,\ \lambda = \pm i \\ \\ \begin{pmatrix} 0 & 1 \\ 1 & 0 \end{pmatrix} & \text{n odd} \implies \lambda^2 - 1 = 0,\ \lambda = \pm 1 \end{cases} \tag{1.16}$$

Hartman-Grobman Theorem

The Hartman-Grobman theorem [68, 69] applies to hyperbolic fixed points, that is, fixed points for which the real values of the eigenvalues are all non-zero. Given a smooth function and a hyperbolic fixed point, the Hartman-Grobman theorem tells us that the smooth function is topologically conjugate to its linerization at the fixed point. That is to say, the dynamics of such a function in a neighborhood around the hyperbolic fixed point is equivalent to the dynamics of its linearization around that fixed point.

Thus for our example above, we see that the Hartman-Grobman theorem does not apply to the n-even case, but does to the n-odd case. However, that doesn't preclude the possibility that the linearization of the function at a non-hyperbolic fixed point may also be topologically conjugate. The theorem only guarantees such conjugacy for hypberbolic fixed points, and in our example, we will find that conjugacy holds for both the even and odd cases. In general, to test for the stability or instability of a fixed point, if the Hartman-Grobman theorem doesn't apply, it is best to apply a more general Lyapunov stability test [70].

For n-even we have the following eigenvalue and eigenvector combination:

$$\begin{cases} \begin{pmatrix} -i & 1 \\ -1 & -i \end{pmatrix}\begin{pmatrix} x_1 \\ x_2 \end{pmatrix} = \begin{pmatrix} 0 \\ 0 \end{pmatrix} \quad \text{for } \lambda_1 = i \;\Rightarrow\; \mathcal{E}_1 = \begin{pmatrix} 1 \\ i \end{pmatrix} \\ \begin{pmatrix} i & 1 \\ -1 & i \end{pmatrix}\begin{pmatrix} x_1 \\ x_2 \end{pmatrix} = \begin{pmatrix} 0 \\ 0 \end{pmatrix} \quad \text{for } \lambda_2 = -i \;\Rightarrow\; \mathcal{E}_2 = \begin{pmatrix} 1 \\ -i \end{pmatrix} \end{cases} \tag{1.17}$$

We can confirm these are correct by noting that $DF(\vec{\bar{x}}) = \mathcal{E}D\mathcal{E}^{-1}$, i.e.,

$$\begin{pmatrix} 0 & 1 \\ -1 & 0 \end{pmatrix} = \begin{pmatrix} 1 & 1 \\ i & -i \end{pmatrix}\begin{pmatrix} i & 0 \\ 0 & -i \end{pmatrix}\begin{pmatrix} \frac{1}{2} & -\frac{i}{2} \\ \frac{1}{2} & \frac{i}{2} \end{pmatrix} \tag{1.18}$$

We note that the Wronskian of $\mathcal{E}$ is not zero, and so these solutions are linearly independent. We have solutions of the form $\vec{x} = \mathcal{E}_i e^{\lambda_i t}$, specifically,

$$\mathcal{X}_1 = \begin{pmatrix} 1 \\ i \end{pmatrix} e^{it}, \quad \mathcal{X}_2 = \begin{pmatrix} 1 \\ -i \end{pmatrix} e^{-it} \tag{1.19}$$

The Wronskian is,

$$\begin{Vmatrix} e^{it} & e^{-it} \\ ie^{it} & -ie^{-it} \end{Vmatrix} = -i - i = -2i \tag{1.20}$$

which is never zero, so the above solutions form a fundamental set of solutions, and our general solution is

$$\mathcal{X} = c_1\mathcal{X}_1 + c_2\mathcal{X}_2 = c_1 \begin{pmatrix} 1 \\ i \end{pmatrix} e^{it} + c_2 \begin{pmatrix} 1 \\ -i \end{pmatrix} e^{-it} \tag{1.21}$$

In order to obtain more realistic solutions, we can take one of the solutions and take its real and imaginary values:

$$\mathcal{X}_1 = \begin{pmatrix} 1 \\ i \end{pmatrix} e^{it} = \mathcal{X}_1 = \begin{pmatrix} 1 \\ i \end{pmatrix} (\cos t + i \sin t) = \begin{pmatrix} \cos t \\ -\sin t \end{pmatrix} + i \begin{pmatrix} \sin t \\ \cos t \end{pmatrix} \tag{1.22}$$

Again we apply the Wronskian test:

$$\left\| \begin{matrix} \cos t & \sin t \\ -\sin t & \cos t \end{matrix} \right\| = 1 \tag{1.23}$$

Hence our general solution can now be written:

$$\mathcal{X} = \alpha_1 \begin{pmatrix} \cos t \\ -\sin t \end{pmatrix} + \alpha_2 \begin{pmatrix} \sin t \\ \cos t \end{pmatrix} \tag{1.24}$$

Hence we see that our fixed point is a "center" in that the flow of the state vector will rotate around the fixed point, rather than towards or away from it (Figure 1.6). We will specify the other types of fixed points as the need arises. The **odd case** follows similarly. As before we note that $DF(\vec{\bar{x}}) = \mathcal{E}D\mathcal{E}^{-1}$, i.e.,

$$\begin{pmatrix} 0 & 1 \\ 1 & 0 \end{pmatrix} = \begin{pmatrix} 1 & -1 \\ 1 & 1 \end{pmatrix} \begin{pmatrix} 1 & 0 \\ 0 & -1 \end{pmatrix} \begin{pmatrix} \frac{1}{2} & \frac{1}{2} \\ -\frac{1}{2} & \frac{1}{2} \end{pmatrix}$$

where again the Wronskian is non-zero, affirming that we have a fundamental set of solutions. Furthermore, our case is made easier by the fact that these solutions are all real. Our solution thus

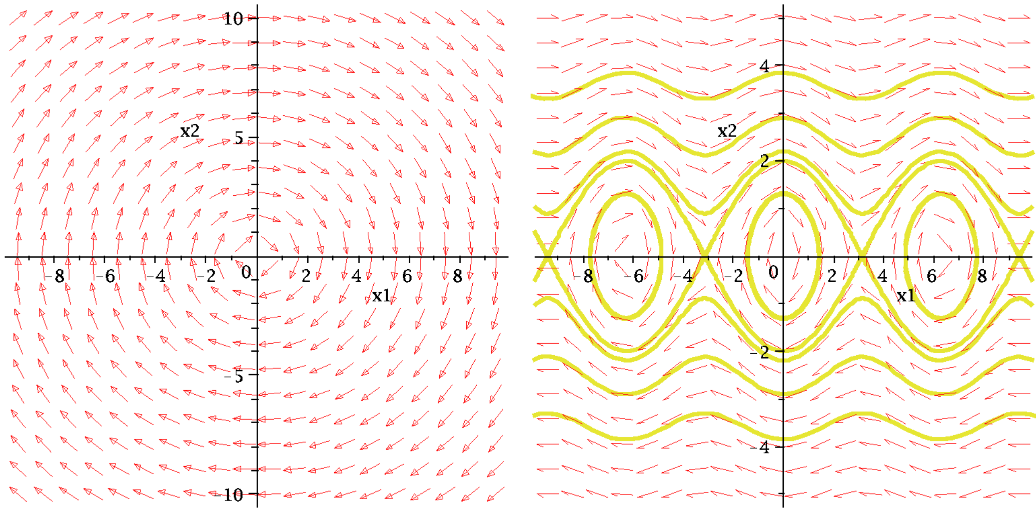

Figure 1.6: Vector plot of the linearized system (left) and the original system (right) are similar only locally for $\vec{\bar{x}} = (n\pi, 0)$, $n \in \mathbb{Z}$ even.

takes the form,

$$\mathcal{X} = c_1\mathcal{X}_1 + c_2\mathcal{X}_2 = c_1 \begin{pmatrix} 1 \\ 1 \end{pmatrix} e^t + c_2 \begin{pmatrix} -1 \\ 1 \end{pmatrix} e^{-t}$$

This suggest an exponential growth in the direction of $(1,1)$ and and exponential decay in the direction of $(-1,1)$ which is indeed the case. The fixed point is an unstable saddle point.

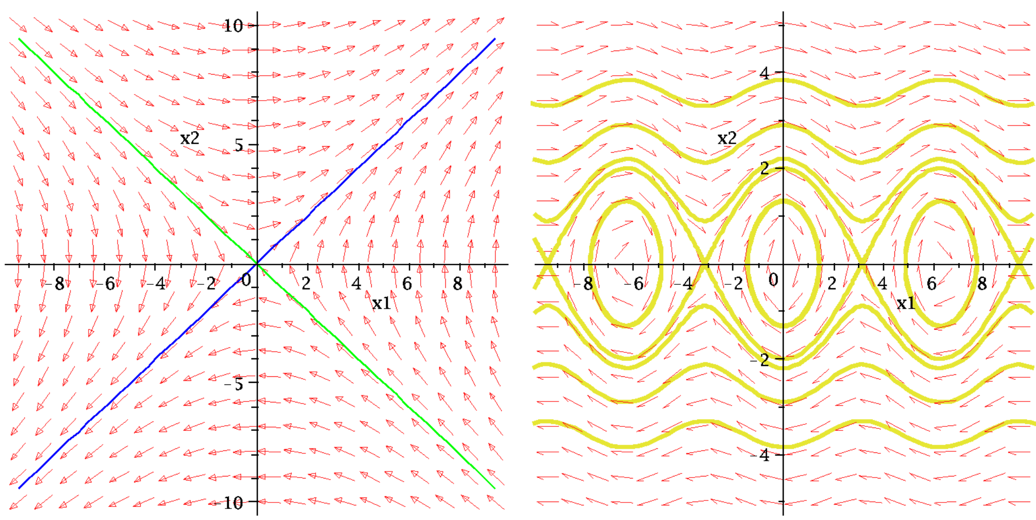

Figure 1.7: Vector plot of the linearized system (left) and the original system (right) are similar only locally for $\vec{\bar{x}} = (n\pi, 0)$, $n \in \mathbb{Z}$ odd.

1.6.2 Dynamics and Parameter-Space

While the information we can gather about a system from its fixed points in state-space with parameters held fixed often indicates some very important features, a more global perspective on a system is gathered by examining how the dynamics around these fixed points change as we vary the system's parameters. In this regard, there exists a rich list of bifurcations in which the dynamics around the fixed points changes in very consequential ways as we change a set of parameters. This is easiest to see in low-dimensional systems (two), where we can visualize these bifurcations quite easily. However, these bifurcations are often easily extended to higher-dimensional systems by holding one or more parameters fixed. For example, in chapter six we consider the codimension-2 parameter space of the Rössler system, in which we hold one parameter fixed and treat the system as if it were a two-parameter system. We judiciously chose which parameter to hold fix, as it will turn out to be the parameter of least consequence to the dynamics of the system.

In the next section, we introduce the pertinent bifurcations which we will be using in later chapters. We introduce them in one or two dimensional systems, where the mathematics and visualization are simplest.

1.7 Some Bifurcations in Dynamical Systems

The term *bifurcation* has a broad meaning in dynamics. The term implies a splitting off of something into two separate branches, but in most instances where we discuss a bifurcation, we have a more ambiguous meaning in mind. In all cases a bifurcation corresponds to a sudden, qualitative change in the behavior of a dynamical system. Having already discussed basic bifurcations for maps, we will now discuss some of the important types of bifurcations that can occur in flows and higher-dimensional systems.

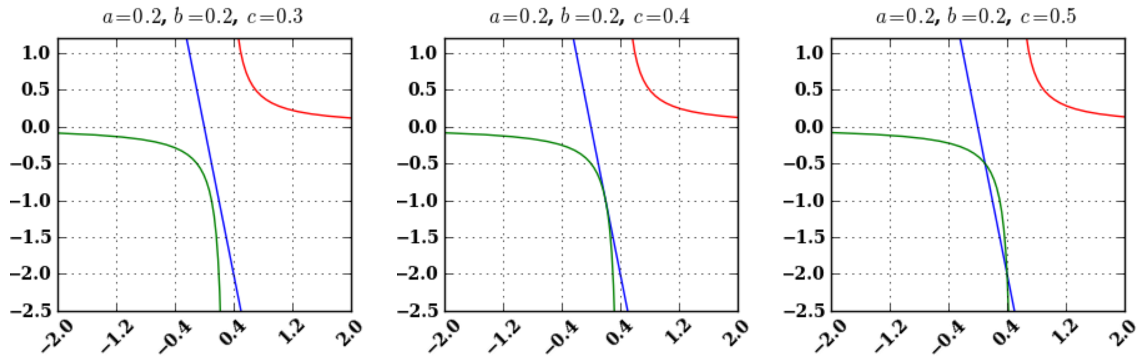

Figure 1.8: A saddle-node bifurcation in the Rössler system. We set $a = 0.2$, $b = 0.2$, and plot the nullclines for $\dot{y}$ and $\dot{z}$ where $z = -y$. Where the nullclines intersect, we have fixed points. At $c = 0.3$, their is no fixed point for the system. At $c = 0.4$, the nullclines make contact at a single point, a saddle-node. At $c > 0.4$, there are two points of contact, corresponding to the existence of a saddle and an node fixed point. Blue line represents $\dot{x}$ nullcline while green and red represent the components of the $\dot{y}$ nullcline.

1.7.1 Saddle-Node Bifurcation

The Rössler system is described by the following set of equations [42],

$$\vec{V}\begin{pmatrix} \dot{x} \\ \dot{y} \\ \dot{z} \end{pmatrix} = \begin{matrix} -y - z \\ x + ay \\ b + z\,(x - c) \end{matrix} \tag{1.25}$$

We can locate the fixed points in this system by setting Equation 1.25 equal to zero. First, we will find that $z = -y$ and $x = -ay$ by setting $\dot{x} = 0$ and $\dot{y} = 0$. We can then plug those values into $\dot{z}$, where we find that,

$$y = \frac{c \pm \sqrt{c^2 - 4ab}}{2a} \tag{1.26}$$

which can be used to solve for x and z. In that we are talking about classical physical systems, we require that these coordinates be real-valued, which is to require that $c^2 > 4ab$. What happens if this is not the case? Figure 1.8 plots the nullclines[13] corresponding to $\dot{y}$ and $\dot{z}$ where we simplify the equations by replacing $z \to -y$, which is a consequence of $\dot{x} = 0$. Wherever these two nullclines intersect, the Rössler system will have a fixed point. If they do not intersect, then the Rössler system

[13]The nullclines are found by setting the equation equal to zero, such that the nullcline for $\dot{y}$ is the line $y = -x/a$

has no fixed points. So, for example, if we set $a = 0.2$, and $b = 0.2$, then $c < 0.4$ corresponds to a region in which we have no fixed points. This made visually clear in Figure 1.8, where for $c < 0.4$ we have no intersections, and for $c > 0.4$ we have two intersections, corresponding to a saddle and a node fixed point. At $c = 0.4$, we have a doubly degenerate fixed point, called a saddle-node fixed point.

1.7.2 Andronov-Hopf Bifurcation

The Andronov-Hopf Bifurcation is the same bifurcation that is commonly called the Hopf Bifurcation in the literature. Working in part with A. A. Witt, Soviet physicist Aleksandr Andronov studied this bifurcation in $\mathbf{R}^2$ in 1929/1930 [71–73]. This work was published in a Paris-based journal, so the Soviet-Western divide didn't prevent its dissemination in Western nations. Eberhard Hopf's work on the bifurcation was definitive, extending it to $\mathbf{R}^n$ in 1942 [73–75]. An alternative name is the Poincaré-Andronov-Hopf Bifurcation [71] due the fact that Poincaré had discussed, in a less rigorous way, the concept as early as 1892 [71, 73, 76, 77].

The theorem can be succinctly stated as follows [78]. We consider a typical dynamical system (Equation 1.12) with fixed points $\vec{F}(\vec{x}, \alpha) = 0$. Suppose that the linearization of the fixed points ($DF(\vec{x})$) has a complex conjugate pair of eigenvalues of the form $c(\alpha) \pm ib(\alpha)$ which cross the imaginary axis for some value α_0, which is to say, the real part of the complex conjugate pair moves from negative (positive) value to positive (negative) value[14] (Figure 1.9). Then a set of periodic orbits bifurcates from the point in state space $(F(\vec{x}), \alpha) = (0, \alpha_0)$. As we will see for the Rössler system, the Andronov-Hopf bifurcation is found to manifest as a curve in codimensional-2 control parameter space. To the left of this curve, no periodic orbits exist. To the right of this curve, we have regions of stable periodic orbits and regions of chaos which persist until the system undergoes a boundary crises, where the attractor makes contact with the boundary of its basin of attraction (and effectively leaks off to infinity) [80].

Since for the research presented in this thesis, particularly that of chapter six, the precise details

[14]There are a few other technical conditions which will be satisfied for the systems we consider. Furthermore, Andronov-Hopf bifurcations are classified as two types: supercritical and subcritical. The Rössler system has a supercritical Andronov-Hopf Bifurcaiton [79].

of the Andronov-Hopf theorem are not pertinent, we discuss it only by way of example.

An example of an Andronov-Hopf Bifurcation

The Morris-Lecar model was formulated to “explain different patterns of electrical activity observed in the barnacle muscle fiber”. It consists of only two differential equations,

$$C\frac{dV}{dt} = -g_{Ca}m_{\infty}(V - E_{Ca}) - g_K n(V - E_K) - g_L(V - E_L) + I \tag{1.27}$$

$$\frac{dn}{dt} = \phi\frac{n_{\infty}(V) - n}{\tau(V)} \tag{1.28}$$

$$m_{\infty}(V) = 0.5\left(1 + \tanh\left(\frac{V - \nu_1}{\nu_2}\right)\right) \tag{1.29}$$

$$n_{\infty}(V) = 0.5\left(1 + \tanh\left(\frac{V - \nu_3}{\nu_4}\right)\right) \tag{1.30}$$

$$\tau(V) = \frac{1}{\cosh\left(\frac{V-\nu_3}{2\nu_4}\right)} \tag{1.31}$$

g_{Ca}	$4.4mS/cm^2$	E_{Ca}	120mV	g_K	$8mS/cm^2$	E_K	-84mV
g_L	$2mS/cm^2$	E_L	-60mV	C	$20\mu F/cm^2$	ν_1	-1.2mV
ν_2	18mV	ν_3	2mV	ν_4	30mV	ϕ	0.04mS^{-1}

The discussion of the deep details of the AH bifurcation are beyond the scope of this chapter. It involves use of the “Center Manifold” on which the dynamics of a fixed point can be reduced for qualitative purposes, and the “Normal Form” of the equations in which the equations are cast in a coordinate system which provides their 'simplest' manifestation. The key result is that at the conditions of an AH bifurcation, the dynamics result in a defining equation that is induced when the real parts of the eigenvalue go through zero and a complex conjugate set of imaginary parts does not [81]. For our current case, we have the linearized matrix of the fixed point in the form,

$$\begin{pmatrix} -\frac{1}{2\nu_2}gC_a\left(1 - \tanh^2(\frac{V-\nu_1}{\nu_2})\right)(V - E_{Ca}) - g_{Ca}m_{\infty} - g_K n - g_L & -g_k(V - E_k) \\ \frac{1}{2\nu_4}\left(\left(1 - \tanh^2\left(\frac{V-\nu_3}{\nu_4}\right)\right)\cosh\left(\frac{V-\nu_3}{\nu_4}\right) + \frac{1}{2}\left(1\tanh\left(\frac{V-\nu_3}{\nu_4}\right) + 2n\right)\sinh\left(\frac{V-\nu_3}{2\nu_4}\right)\right) & -1 \end{pmatrix} \tag{1.32}$$

and so we must numerically calculate the eigenvalues to locate the AH bifurcation due to the transcendental functions (Figure 1.9).

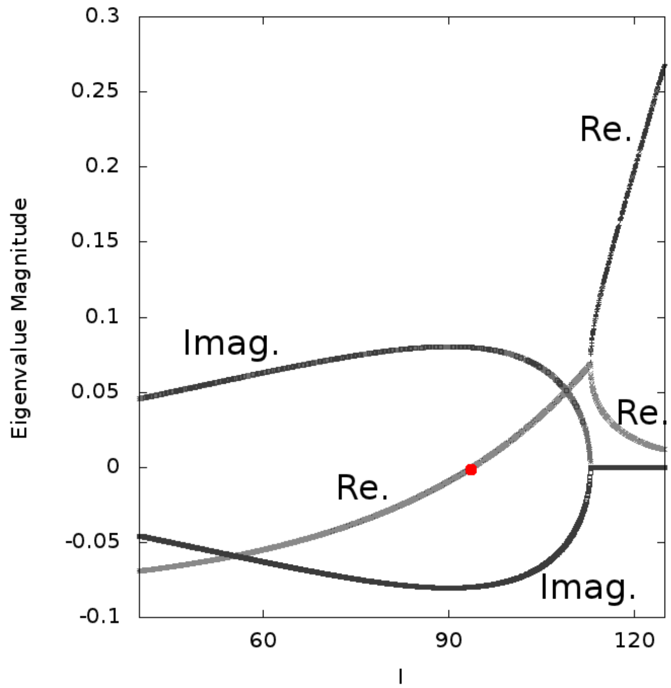

Figure 1.9: Magnitudes of the real and imaginary parts of the eigenvalues of the Morris-Lecar system as a function of bias current I. Notice that at nearly $I = 93.85$, the real part of the eigenvalues goes through zero while the imaginary parts do not vanish; under conditions satisfied by this system, this locates the AH bifurcation.

1.7.3 Homoclinic Bifurcations

Another system from neuroscience which undergoes an Andronov-Hopf bifurcation is the Chay system [82, 83] which was the first biophysically realistic model for neuronal type cells that demonstrated chaotic behavior. This model is three-dimensional, but by use of an analysis method called "fast-slow decomposition" [84] we find which of three dynamical equations evolves the slowest, and if this evolution is substantially slower than the other two, then we set the corresponding vector component to be a constant, reducing the system for analysis to a two-dimensional model. For the Chay system, the fast-system is given by two equations [83],

$$\dot{v} = \frac{1}{\epsilon}\left(am_\infty^3(v)h_\infty(v)\,(E_I - v) + n^4\,(E_k - v) + \frac{\delta u}{1+u}\,(E_k - v) + l\,(E_l - v)\right) \tag{1.33}$$

$$\dot{n} = \frac{n_\infty(v) - n}{\tau(v)} \tag{1.34}$$

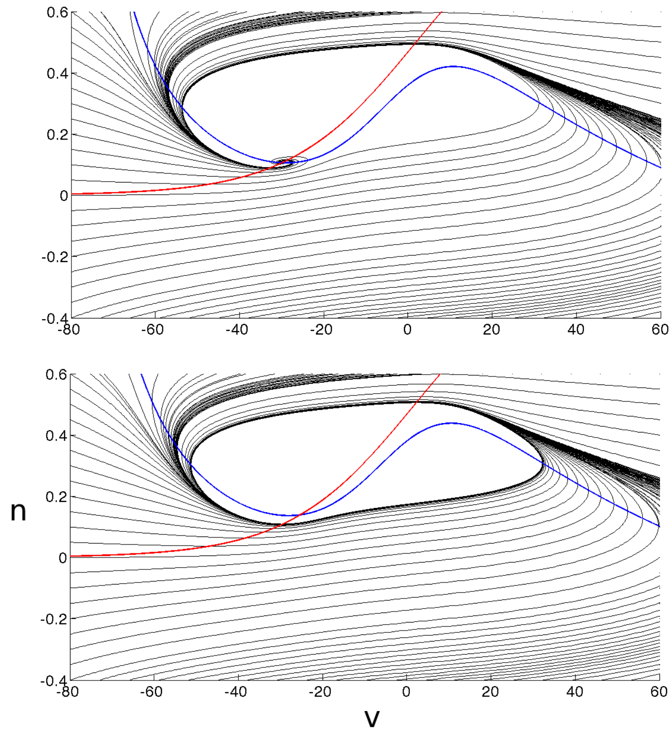

Figure 1.10: Phase space plot of Morris-Lecar system before (top, $I = 80.0$) and after (bottom $I = 93.7$) an AH bifurcation has formed. Black lines represents trajectories of test initial conditions which are evenly placed at the left edges of the figures. Red and blue lines represent nullclines for n and V respectively. Nullclines correspond to locations in phase space where either $\dot{V}$ or $\dot{n}$ is equal to zero. Where the nullclines intersect we have a fixed point for the system. For $I = 80$, we see that the fixed point is a stable spiral attracting point for nearby initial conditions (test initial conditions and their trajectories are marked with black lines). After an Andronov-Hopf bifurcation, the fixed point becomes unstable and a small limit-cycle has developed around the fixed point.

where,

$$\alpha_m = \frac{2.5 + v}{1 - \exp(-(v + 2.5))} \tag{1.35}$$

$$\beta_m = 4\exp(-(v + 5)/1.8) \tag{1.36}$$

$$\alpha_h = 0.07\exp(-(v + 5)/2) \tag{1.37}$$

$$\beta_h = \frac{1}{1 + \exp(-(v + 2))} \tag{1.38}$$

$$\alpha_n = \frac{0.1(2 + v)}{1 - \exp(-(v + 2))} \tag{1.39}$$

$$\beta_n = 0.125\exp(-(v + 3)/8) \tag{1.40}$$

and,

$$\tau(v) = \frac{1}{\alpha_n + \beta_n} \quad (1.41)$$

$$m_\infty = \frac{\alpha_m}{\alpha_m + \beta_m} \quad (1.42)$$

$$n_\infty = \frac{\alpha_n}{\alpha_n + \beta_n} \quad (1.43)$$

$$h_\infty = \frac{\alpha_h}{\alpha_h + \beta_h} \quad (1.44)$$

and we use the variables $E_I = 10$, $\epsilon = 0.1353$, $\gamma = 0.01833$, $E_K = -7.5$, $a = 1.059$, $\delta = 0.02$, $E_{Ca} = 10$, $l = 0.00412$, and $E_l = -4$. The variable u will be used as our bifurcation parameter.

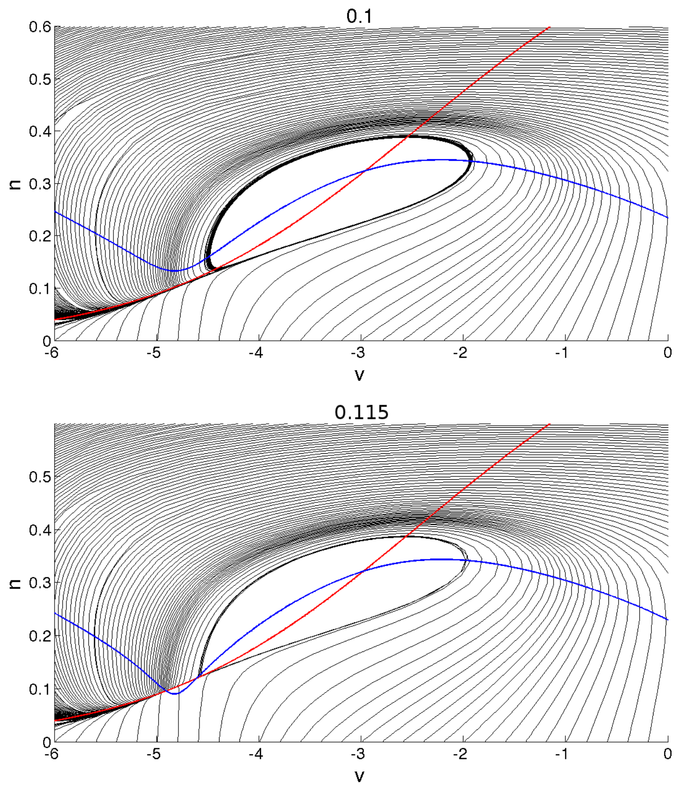

Figure 1.11: Phase space plot of Chay system before (top) and approximately at (bottom) a homoclinic bifurcation which follows an Andronov-Hopf bifurcation. Black lines represent trajectories of test initial conditions which are evenly placed at the bottom of the figures. Where the nullclines intersect we have a fixed point for the system. For $u = 0.1111667$, a saddle-node bifurcation results in new fixed points. The saddle fixed point drifts rightward and eventually collides with the limit cycle at $u \approx 0.115$. This terminates the limit-cycle created by the Andronov-Hopf bifurcation such that the unstable manifold of the new fixed point is connected to the stable-manifold of the same fixed point.

For $u < 0.1111667$ and $u > 0.296801$, there is only one fixed point (Figure 1.11, top panel, and Figure 1.12). Between two saddle-node bifurcations there exist three fixed points ($0.1111667 < u < 0.296801$). In the bottom figure, we superimpose the $v-$axis projection of the radius of the limit-cycle induced by the Andronov-Hopf bifurcation onto the bifurcation diagram. At $u \approx 0.115$, this limit-cycle collides with one of the three fixed points which results in a homoclinic orbit. This saddle homoclinic orbit bifurcation terminates the limit-cycle. Labels on the figures are H for Andronov-Hopf bifurcation, and LP for limit-point corresponding to a saddle-node bifurcation.

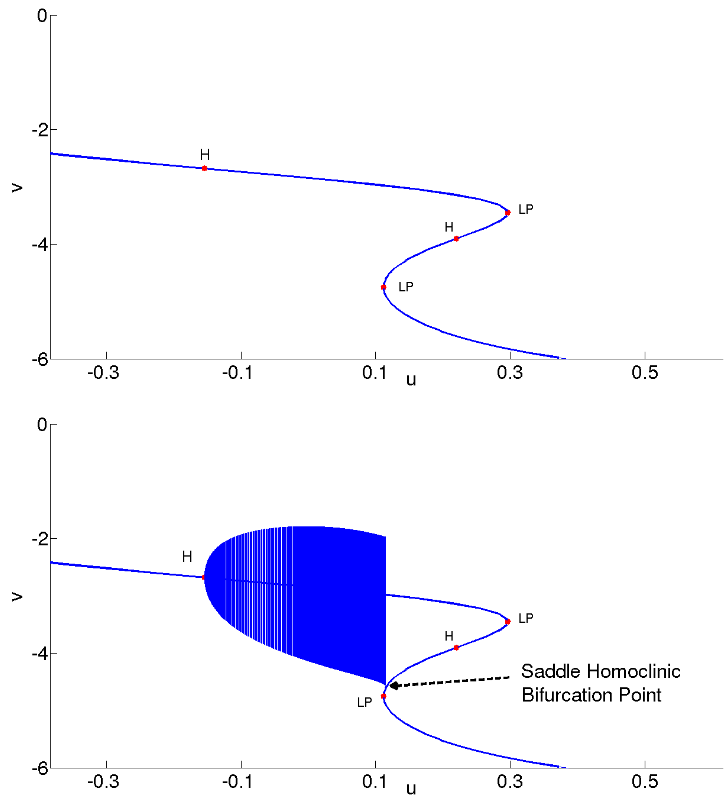

Figure 1.12: Bifurcation diagram for Chay fast-subsystem (Equation 1.34). The curve traces out the position of the system's fixed points in the $u - v$ plane with bifurcation points found using the MATCONT continuation software [85]. We use u as the bifurcation parameter. For $u < 0.1111667$ (top panel) and $u > 0.296801$, there is only one fixed point. Between two saddle-node bifurcations there exists three fixed points ($0.1111667 < u < 0.296801$). In the bottom figure, we superimpose the $v-$axis projection of the radius of the limit-cycle induced by the Andronov-Hopf bifurcation onto the bifurcation diagram. At $u \approx 0.115$ (bottom panel), this limit-cycle collides with one of the three fixed points which results in a homoclinic orbit. This saddle homoclinic orbit bifurcation terminates the limit-cycle. Labels on the figures are H for Andronov-Hopf bifurcation, and LP for limit-point corresponding to a saddle-node bifurcation.

The period of the limit-cycle, induced by the Andronov-Hopf bifurcation at $u = -0.15455969$, increases with increasing parameter u. The limit-cycle expands as u increases. In the meantime, at

$u = 0.1111667$, a saddle-node bifurcation results in new fixed points. As the limit-cycle continues to expand and the saddle fixed point drifts closer to the original fixed point, the period of the limit-cycle increases. As the distance between the saddle fixed point and the limit-cycle decreases, the period of the limit-cycle begins to grow exponentially (Figure 1.13). Theoretically, when the limit-cycle makes contact with the saddle fixed point, the period is infinite. This is because the cycle consists of the unstable manifold of the saddle fixed point which circles back around as the stable manifold of the same fixed point. Of course, in three-dimensional chaotic systems, a homoclinic bifurcation point

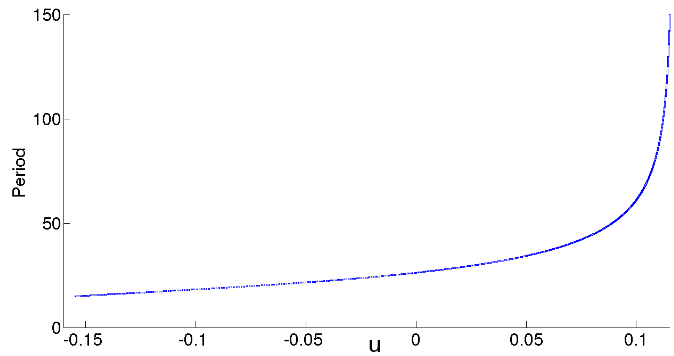

Figure 1.13: The period of the limit-cycle, induced by the Andronov-Hopf bifurcation at $u = -0.15455969$, increases with increasing parameter u. The limit-cycle expands as u increases. In the meantime, at $u = 0.1111667$, a saddle-node bifurcation results in new fixed points. As the limit-cycle continues to expand and the saddle fixed point drifts closer to the original fixed point, the period of the limit-cycle increases. As the distance between the saddle fixed point and the limit-cycle decreases, the period of the limit-cycle begins to grow exponentially. Theoretically, when the limit-cycle makes contact with the saddle fixed point, the period is infinite. This is because the cycle consists of the unstable manifold of the saddle fixed point which circles back around as the stable manifold of the same fixed point.

will *not* necessarily result in the termination of cyclic behavior. For example, in the Rössler system, a strange attractor is found in the system after an Andronov-Hopf bifurcation induces a limit-cycle. This limit-cycle undergoes a period-doubling cascade and then transitions to being a fully chaotic attractor. This strange attractor contains of an infinite number of unstable periodic orbits. Only a finite number of these periodic orbits get trapped as homoclinic orbits as the system undergoes a homoclinic bifurcation [86]. Thus, though we will find the notion of homoclinic bifurcation very useful in Chapter Six, unlike in the Chay system, this bifurcation will not result in the termination of the Rössler strange attractor.

1.8 A Definition of Chaos for Flows

The definition of chaos we use for flows will be similar to that we used for maps. However, before we can make this definition more precise for flows, we must introduce a few key concepts.

In order to have chaos in flows, we need a mechanism that induces chaos in a deterministic system. There are a number of such mechanisms. For example, in the Lorenz system, the topological mechanism that generates chaos is called stretch-tear-squeeze [87, 88]. Dynamically speaking, the Lorenz transitions to chaos upon undergoing a "homoclinic explosion" [89–91]. For the Rössler system, on the other hand, the topological mechanism is one of stretch-fold-squeeze [36, 87, 92] where, dynamically speaking, chaos begins in the system after it passes through an Andronov-Hopf bifurcation [93, 94] and then undergoes a period-doubling cascade which accumulates at the Feigenbaum point, after which the system is chaotic. The route to chaos taken by the Rössler system happens to be remarkably similar to that taken by the Logistic Map, and we will see in Chapter Six why this is not a coincidence. Later in this chapter, we will provide more details on what is called the Smale Horseshoe, a remarkably simple two-dimensional map which describes the essential dynamics of the stretch-fold-squeeze mechanism (also called the Smale horseshoe mechanism) in highly-dissipative systems, which is the route to chaos taken by a wide variety of systems, including the Rössler system [42], chemical systems [95], lasers [96–99], electro-chemical systems [100], vibrating strings [101], stellar phenomenon [102], radio engineering [13, 16], and so on.

First, having introduced the terms "stretch" and "squeeze", we will want to quantify these terms with a mathematical description, and for that purpose we use the concept of Global Lyapunov Exponents.

1.8.1 Lyapunov Exponents and Global Lyapunov Exponents

Lyapunov Exponents represent a mathematical and numerical means of probing a system for chaotic or stable behavior.

For maps, we can define the Lyapunov number L of an orbit $\{x_1, x_2, x_3, \cdots\}$ as [78],

$$L(x_1) = \lim_{n\to\infty} \left(\|f'(x_1)\|\|f'(x_2)\| \cdots \|f'(x_n)\|\right)^{1/n} \tag{1.45}$$

and the Lyapunov exponent λ by,

$$\lambda(x_1) = \lim_{n\to\infty} (1/n) \left(\ln \|f'(x_1)\| + \cdots + \ln \|f'(x_n)\|\right) \tag{1.46}$$

Whenever λ is positive, and an orbit is not asymptotically periodic (it isn't evolving towards a stable period), we have chaotic behavior. Whenever $\lambda \to -\infty$, an orbit includes a critical point and is thus stable.

For flows, this definition is necessarily somewhat more complicated and involves geometric considerations [78]. A flow described by an n dimensional dynamical system will have n Lyapunov exponents. Assuming we have an n dimensional system, we consider an n-sphere of very small radius r_0 We write this sphere of initial conditions as U [78]. We wish to see how this sphere evolves under the dynamical system. We know that in order to have chaos, there must be an expansion of the sphere in at least one dimension. In order for this system to not be divergent, we also require the contraction of the sphere in at least one different direction. Haken showed in 1983 that for systems of ordinary nonlinear differential equations, at least one Lyapunov exponent vanishes [103–105].

We can find the axes of the resulting ellipsoid via a linearization of the dynamical equations, recalling our previous discussion on the Jacobian (Equation 1.15). If we define

$$J_m = D\mathbf{f}^m(\vec{\mathbf{x}}) \tag{1.47}$$

as the linearization of the m^{th} iterate dynamical equations, then for m large enough (but not two large that mixing has significantly changed the shape of the set of initial conditions), $J_m U$ will give us an ellipsoid of images of initial conditions, where the initial sphere U has been contracted in at least one direction and expanded in at least one other. From this linearization we can find an orthogonal set of axes which describe the major and minor axes of the ellipsoid. We will find three

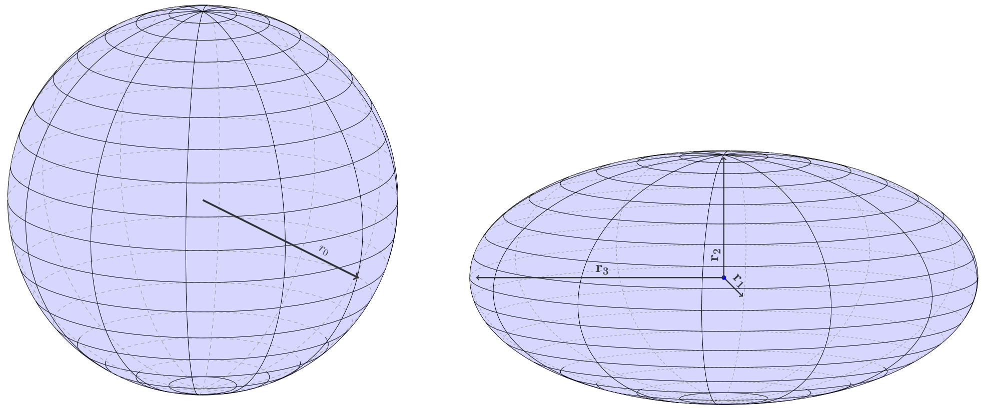

Figure 1.14: Geometric representation of a sphere of initial conditions (radius r_0) which are stretched in the horizontal direction (r_3), squeezed in the vertical direction (r_2), and unchanged in the direction of flow (into/out of page, $r_1 = r_0$). Figures constructed using the Tikz LaTex environment [106].

lengths for the ellipsoid, r_1, r_2, r_3. We refine this notation by adding the superscript m to indicate that we have considered m iterations to calculate the axes lengths. Then we can define the Lyapunov number as,

$$L_i = \lim_{m\to\infty} (r_k^m)^{1/m} \tag{1.48}$$

and the Lyapunov exponent as

$$\lambda_i = \ln(L_i) \tag{1.49}$$

It is conventional to arrange the order of the exponents such that $\lambda_1 \geq \lambda_2 \geq \lambda_3$. Furthermore, for conservative systems, $\sum_i \lambda_i = 0$, while for dissipative systems (such as strange attractors), $\sum_i \lambda_i < 0$ Of course, in the real-world we can't take such a limit to infinity, and so we have to use numerical simplifications. We select a set of orthonormal basis vectors, $\{w_1^0, \cdots, w_m^0\}$ and create corresponding

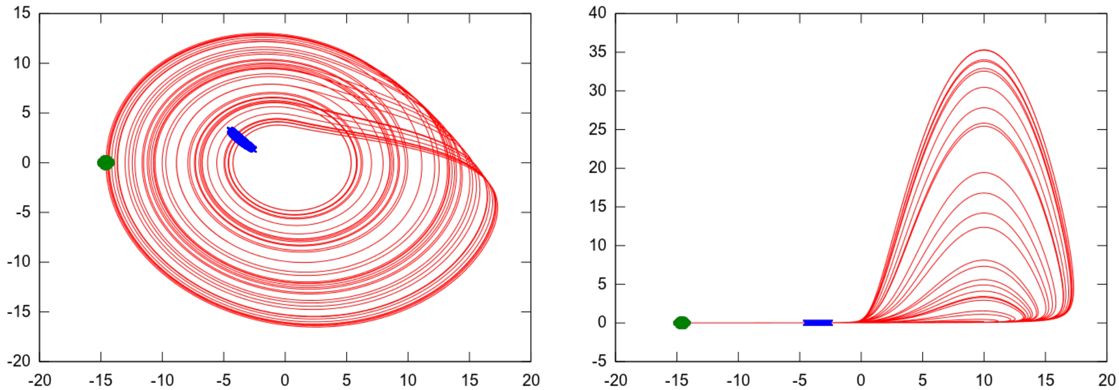

Figure 1.15: The Rössler attractor for $(a, b, c) = (0.15, 0.2, 10.0)$, shown in the x, y projection (left) and the x, z projection (right). We integrate the system for a long enough time period to outline the general shape of the attractor (red). Numerical simulation of the stretching and squeezing of flow on a spherical set of initial conditions (green sphere) and its state after evolving for 500 RK4 time steps on the other side of the attractor (blue blob). The spherical clump of initial conditions has been stretched in a direction perpendicular to the flow within the $x - y$ plane, and squeezed down to a very thin slice in a direction normal to the $x - y$ plane.

vectors,

$$z_1 = Df(\vec{x})w_1^0 \tag{1.50}$$

$$z_2 = Df(\vec{x})w_2^0 \tag{1.51}$$

$$\vdots \quad \vdots \tag{1.52}$$

$$z_m = Df(\vec{x})w_m^0 \tag{1.53}$$

Using a Gram-Schmidt orthogonalization procedure, we orthonormalize the resulting vectors z_i and repeat the procedure described by Equation 1.53. We again orthonormalize those resulting vectors, and repeat again, repeating m times to approximate the resulting ellipsoid and calculate an approximation of the Lyapunov exponents. For a global Lyapunov exponent, we repeat this process over multiple points on the attractor and take an average. In our research, we use the well-documented LESNLS software package [107] to calculate global Lyapunov exponents.

Now we return to the Rössler system. When this system is chaotic, its strange attractor will have $\lambda_1 > 0$, $\lambda_2 = 0$, and $\lambda_3 < 0$. As we vary the parameters, we will encounter regions of stability, in which we find $\lambda_1 = 0$, $\lambda_2 < 0$, and $\lambda_3 < \lambda_2 < 0$.

Thus we see that λ_1 and λ_2 can be used as probes for regions of chaos and stability in parameter space. Figure 1.16 finds that these two exponents give us a very clear map in parameter space of regions of chaos and regions of stability. Furthermore we see fascinating structures within this map

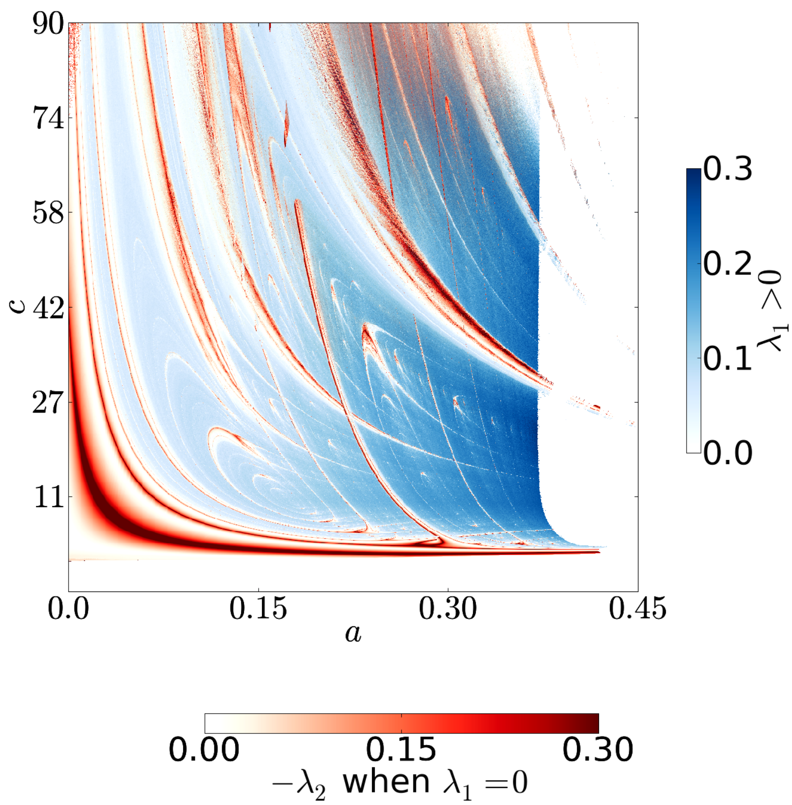

Figure 1.16: Lyapunov diagram for the Rössler system. (Color online). Blue coloration reflects the intensity of the first Lyapunov exponent, red coloring reflects that of the negative of the second exponent when $\lambda_1 = 0$. Blue regions correspond to chaotic behaviors, red regions correspond to regions of stability. White regions correspond to transitional regions or regions where the attractor has undergone a boundary crises. Lyapunov exponents were calculated in a 1000x1000 grid using the LESNLS software package [107].

that indicate a deeper level of order than we might anticipate given a random search for stability in state space. We will return to this topic in greater detail in Chapter Six, where we find that this order is the signature for a number of dynamical and topological features of the Rössler system.

1.9 Smale Horseshoe and the Paths to Chaos

While we have already shown the path to chaos taken by unimodal maps (the period-doubling cascade route, or Feigenbaum scenario), we have yet to explain how flows can exhibit chaotic dynamics. We used two neurological models, which are flows, but we looked at them in their non-chaotic regimes in order to discuss the concept of dynamical bifurcations, a concept which we will need to make use of in Chapter Six. Furthermore, by fast-slow decomposition, we looked at these systems as two-dimensional flows, which cannot exhibit chaos, though their full three-dimensional system can and does exhibit chaos under certain conditions [82, 83][15].

And although we will be examining a number of attractors in Chapters Three and Four, we will be looking at those attractors as flows from the perspective of fluid mechanics. In Chapter Six, we will be very interested in the exact path to chaos taken by one attractor in particular, the Rössler attractor. This path, the stretch-fold-squeeze mechanism, can be understood in the context of chaos in two-dimensional maps by analyzing the Smale Horseshoe and the route taken to chaos is the Feigenbaum scenario. It seems on first reading rather remarkable that a three dimensional flow such as that corresponding to the Rössler attractor exhibits the same path to chaos as that taken by maps such as the Logistic Map, and we will show here why this is the case.

We've included a number of excellent references to texts in the bibliography which give thorough introductions to various other paths to chaos such as the Pomeau-Manneville scenario (crises of periodic oscillations and the intermittency transition route) and the Ruelle-Takens-Newhouse scenario [2, 4, 35, 36, 40, 78, 89, 114–118], though these other paths are off-topic for the purposes of this thesis and will not be discussed further.

1.9.1 Historical Background

Stephen Smale first attempted to prove that chaos does not exist, and published a conjecture to that effect. Shortly thereafter, he received a letter from a mathematician at M.I.T., Norman Levinson, who informed him of a counterexample previously found by Cartwright and Littlewood (and experi-

[15] In fact a number of neurological systems exhibit chaos, including both individual neurons [36, 82, 83, 108, 109] and networks of neurons [110–112]. Other systems can exhibit chaos-like behavior in the presence of noise, or sensitivity to initial conditions [84, 113].

mentally by Van der Pol, though he didn't realize it) which invalidated his conjecture [119]. Having already won the Fields medal for his work on the Poincaré conjecture (a problem in topology with no direct relation to chaos theory), this invalidation would not have been a great embarrassment to Smale, but it nevertheless propelled him to find out precisely why he was wrong.

It is frequently found, in the telling of the history of chaos theory, that the starting point for our modern understanding of chaos is Lorenz and his discovery in the early 1960s of chaotic behavior in the Lorenz attractor from computational rounding errors. This is unfortunate, as it neglects very important work by a number of mathematicians, especially the contributions of Cartwright and Littlewood who essentially proved, mathematically, that chaos could exist in nonlinear equations [13, 16]. Their work virtually resurrected previous findings by Van der Pol, who had discovered experimental chaos decades before Lorenz [13]. It was the work of Cartwright and Littlewood which lead Stephen Smale to investigate in a geometrically intuitive fashion how certain classes of nonlinear dynamical systems could produce chaotic behavior.

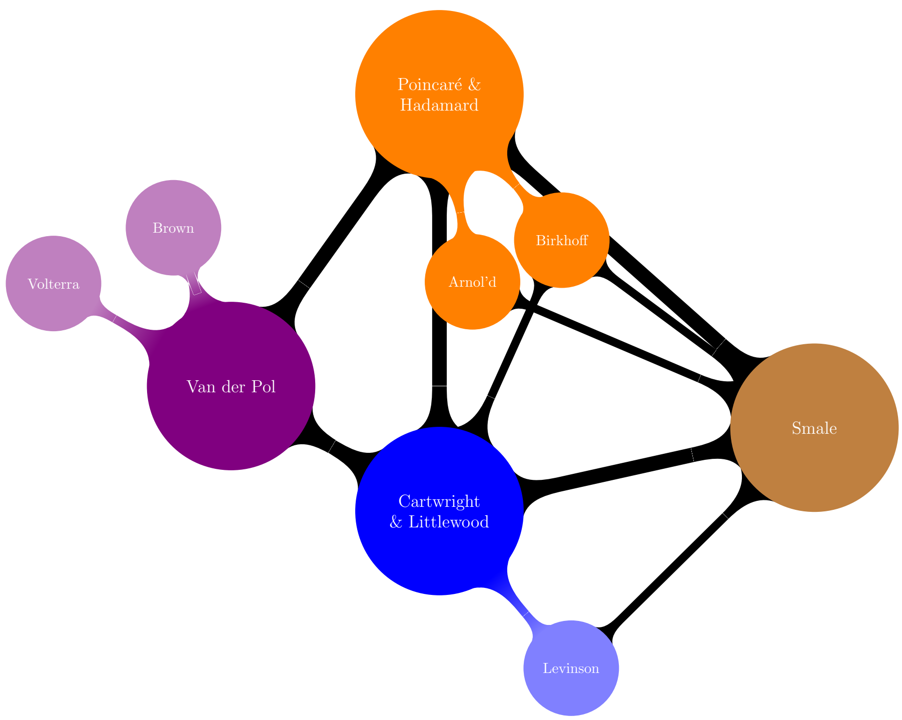

Figure 1.17: Map of the most important influences leading to the development of the Smale Horseshoe Map [13, 16, 119].

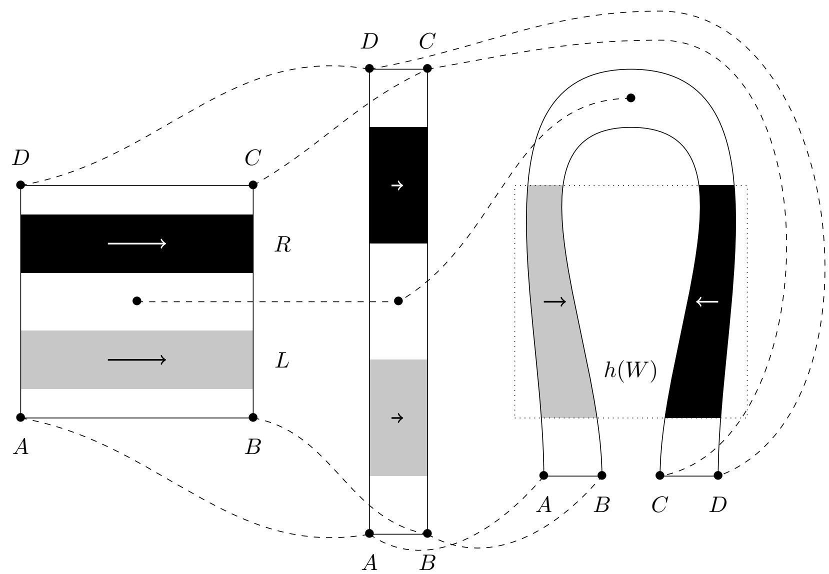

Figure 1.18: The Smale Horseshoe Map first elongates the square $ABCD$ (stretch) and then folds the elongated form at midpoint (folding) to create a horseshoe like pattern. We label the light-gray region L for left and the dark region R for right. This map overlaps with the original square in two disconnected regions. We've placed arrows in the two disconnected regions to show the direction reversing effect of the mapping. The region which is mapped to the left side of the horseshoe is labeled L, and the region mapped to the right side is labeled R. Figure constructed using the Tikz LaTex environment [106].

1.9.2 The Horseshoe Map

The Smale Horseshoe Map (SHM) [34, 119] represents a surprisingly simple yet rich path to chaos, and any discussion of this topic is worthy of an entire thesis. However, we will cover the most pertinent points as they relate to the Rössler system and its route to chaos. The SHM is an injective map, which we will denote $h : \mathbf{R}^2 \to \mathbf{R}^2$ [78], on $\mathbf{R}^2$. Begin with a square $W \in \mathbf{R}^2$ and label its four corners $ABCD$. As shown in Figure 1.18, the SMH stretches this square so that AD and BC elongate while DC and AB shorten. We then fold this elongated region at the midpoint (this is not necessary, but we do for introductory purposes). Keeping track of the edges of the region W, we find that $h(A) \to A'$, $h(B) \to B'$, $h(C) \to C'$, and $h(D) \to D'$. The resulting shape resembles a horseshoe, and overlaps with the original square W as shown in Figure 1.18. We can discover which parts of the original square W are mapped, by the SHM, back onto W by reversing the mapping process and keeping track of the regions of overlap. The SHM maps W onto itself in two disjoint vertical regions, which we label L for the one on the left side of the square, and R for the one on the right side of the square (see Figure 1.18 for a visualization) such that $L \cup R = W \cap h(W)$. As we follow these regions on a reversal of the mapping, by first unfolding the horseshoe and then resizing it to fit the square W, we find that the two vertical regions L And R are mapped from two horizontal strips in the original space W.

This labeling is convenient for applying symbolic dynamics. As we apply further iterations of the SHM, we keep track of which region a point is mapped to. Starting from W, we can label the first symbol sequence $S_1 \in \{L, R\}$. The next iteration of the SHM will map the horseshoe into a more complicated horseshoe as follows. We take the original horseshoe and elongate it in the vertical direction (shrinking it correspondingly in the horizontal direction). The elongated horseshoe is then folded such that the arch of the horseshoe becomes the bottom left leg of the new horseshoe. Figure 1.19 demonstrates this process. Instead of introducing more symbols to describe the second iteration of the map, we simply attach the symbols L or R to the original regions depending on whether or not that particular piece lands on the left side of the new horseshoe or on the right side (this is called a Markov partition [78]). That is, the second iterate will map W into four disconnected regions. As is apparent in Figure 1.19, $S_2 \in \{LL, RL, RR, LR\} \equiv \{LS_1, RS_1\}$. Now if we were to reverse this second iteration while keeping track of the disconnected regions, we would be able to locate where on the original space W the regions LL, RL, RR, and LR originated. We would do so by unfolding the second iteration of the horseshoe, resizing it, unfolding once more, and then resizing to the space of W. In doing so we will find that the regions of $h^2(W) \cap W$ originate from four horizontal strips of W (from top to bottom: RL, RR, LR, LL). This can be seen by visualizing the unfolding and resizing of the second-iterate horseshoe in Figure 1.19. These strips coincide with those on the right side of Figure **??** with a center piece removed.

Following this pattern, we can see that each mapping h^n results in 2^n disjoint vertical regions in $h^n(W) \cap W$ which originate from to 2^n disjoint horizontal regions of the square W. Another way to look at this is to start with the pre-image of the intersection of h^1 and subtract out the middle region of the shaded regions for the next iterate h^2, resulting in four disjoint shaded regions. Then

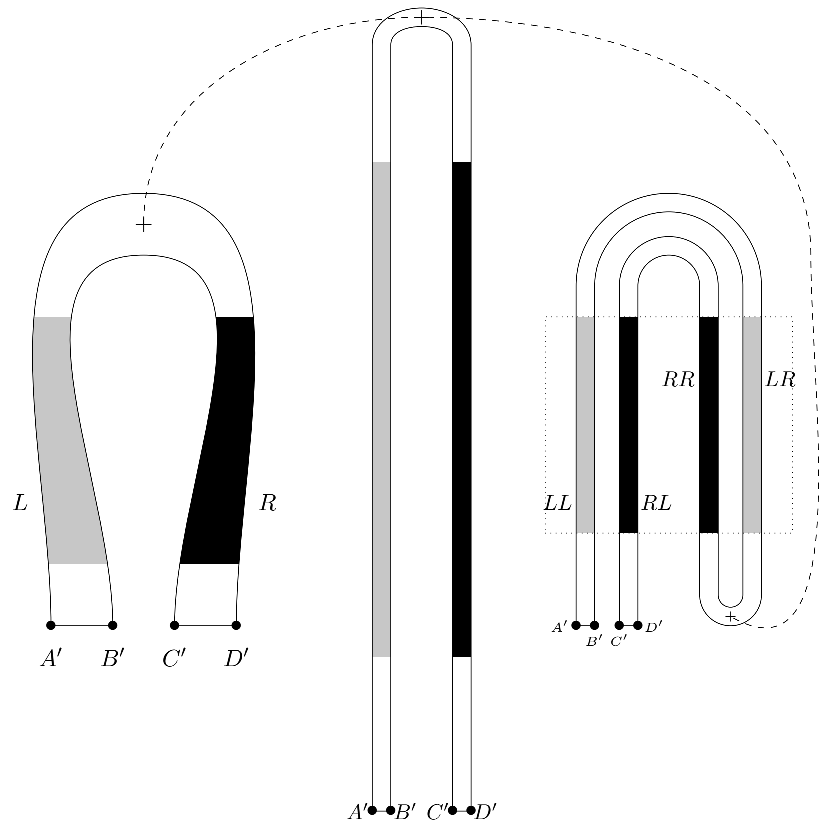

Figure 1.19: The second iteration of the Smale Horseshoe Map first elongates the horseshoe of the first iteration (stretch) and then folds the elongated form at midpoint (folding) to create a more complicated horseshoe-like pattern. We mark the center of the arch of the horseshoe with a + symbol and trace its position over the mapping. Figure constructed using the Tikz LaTex environment [106].

for h^3, subtract out a middle region for each of the four shaded regions, resulting eight disjoint shaded regions, and so on. In this way, the SHM constructs a Cantor set in which we have repeated iterations of removing the "middle-third" section of each shaded region This is our first hint that there may be chaotic dynamics within the SMH. We can describe the construction of a Cantor set with the iterative equation,

$$C_n = \frac{C_{n-1}}{3} \cup \left(\frac{2}{3} + \frac{C_{n-1}}{3} \right) \tag{1.54}$$

where C_n represents the n^{th} line in Figure 1.20. This line is the union of the first thirds of the previous line and the last thirds of the previous line.

The Cantor ternary set has a very rich mathematical background, but finding a mapping which

Figure 1.20: The first four iterations of the process to create a Cantor ternary set using a unit line. The Cantor set is a fractal with self-similarity at all levels. Figure constructed using the Tikz LaTex environment [106].

manifests a mechanism for creating a Cantor set should remind us of the Logistic Map, which itself can create a Cantor set for $r = 4.5$, as we have already discussed.

As we continue to iterate the SHM ad infinitum, we will limit to an infinite uncountable number of infinitesimally thick horizontal lines, each identifiable by a sequence $S_{-1}S_{-2}\cdots S_{-n}\cdots$ where each $S_{-i} \in \{L, R\}$. This infinite collection of horizontal lines represent the vertical coordinates (the y coordinates) of the invariant set H of the SHM, that is, the set of all points which remain in W for all forward and backward iterations of the SHM. To find the horizontal (x) coordinates for this set, we apply repeated intersections of h with W. From Figure 1.19, for example, we see the first two intersection of iterations (h^1 on the left, h^2 on the right). These intersections represent vertical lines where, upon each successive iteration, the middle third of each shaded region is removed. We can symbolically label these vertical lines based on their positions on the left (L) or right (R) of W. To denote that these are forward iterations, we write them as $L.$ and $R.$ with a period. For the intersection corresponding to h^2, we take the original designation of each piece ($L.$ or $R.$) and insert a new label X corresponding to their new position ($LX.$ or $RX.$) where $X \in \{L, R\}$. For example, the intersections on the right side of Figure 1.19 will correspond to, from left to right, symbols $LL.$, $RL.$, $RR.$, and $LR.$.

This again produces a Cantor set, an uncountable number of vertical lines. The intersection of these two Cantor sets, the vertical and horizontal, creates a two-dimensional Cantor set called "Cantor Dust". Each point in this uncountably infinite set is described by an infinite symbol sequence $\cdots S_m \cdots S_2 S_1.S_0 S_{-1} S_{-2} \cdots S_{-n} \cdots$. These points are the invariant set H of h, all points in W that forever remain in W under forward and backward iterations of the SHM. In a similar manner in which we had a shift map for the symbolic dynamics of the logistic map, it is easy to see that by applying h to any point $\cdots S_m \cdots S_2 S_1 . S_0 S_{-1} S_{-2} \cdots S_{-n} \cdots$, we are mapped to a point $\cdots S_m \cdots S_2 . S_1 S_0 S_{-1} S_{-2} \cdots S_{-n} \cdots$. Denote this shift operator as σ_h and S as the set of all symbol sequences corresponding to all points in H, then we have,

$$\begin{tikzcd} H \arrow[r, "h"'] \arrow[d, "\pi"] & H \arrow[d, "\pi"] \\ S \arrow[r, "\sigma_h"'] & S \end{tikzcd} \tag{1.55}$$

where π is a homeomorphism mapping of the points of H to the symbol set S.

We also note that due to the stretching and squeezing, the SHM will have two Lyapunov exponents, $\lambda_1 > 0$ and $\lambda_2 < 0$. The Smale Horseshoe Map is a two-dimensional dynamical system that generates an invariant set H that is bounded and unstable. In fact, this map is chaotic [34, 78], possessing one positive and one negative Lyapunov exponent.

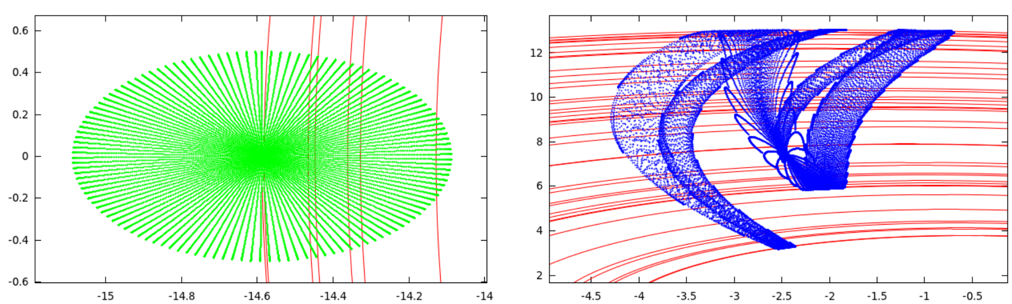

Figure 1.21: The Rössler attractor for $(a, b, c) = (0.15, 0.2, 10.0)$. Similar set up as in Figure 1.15, only now we focus in on the initial sphere of conditions (left, appears elliptical only due to plot scaling) where the regular structure is due to the algorithm for setting the initial conditions. This regularity helps capture the effect of the stretch-fold-squeeze mechanism when we see the evolution of the sphere of initial conditions after 3500 RK4 time steps (right, compare with the 500 RK4 time steps in Figure 1.15). The regular patterns in the distribution of the initial conditions (left) is still partly preserved after many RK4 time steps (right).

In certain dynamical systems which are highly-dissipative, the flow is stretched, squeezed, and then folded back onto itself in such a way that the dynamics mirror the Smale Horseshoe Map mechanism. The Rössler system is an example of such a system, and in Figure 1.21 we show the evolution of a small ball of initial conditions after six cycles. The ball is stretched out and folded onto itself multiple times.

1.10 Conclusions

The mathematics of dynamical systems is a vast and rich field, and we have only given a brief sample in this chapter. These concepts will be used in later chapters. In Chapters 3 and 4, we will examine features of strange attractors which can be extracted analytically from the dynamical information. In Chapter 7, we will call upon the concepts of Andronov-Hopf bifurcations and introduce the concept of Homoclinic and Heteroclinic Bifurcations in order to better understand features in a codimensional-2 phase plane of Rössler type systems.

First, we take a brief detour into the field of fluid dynamics.

Chapter 2: Vortex Tubes for Dynamical Systems

The focus of this thesis is on the global behavior of strange attractors. Specifically, we wish to find characteristics of strange attractors which will lend greater insight into their overall features. Previous work has classified strange attractors based on their global topological features, such a their genus [87]. Long before this, Poincaré's program for dynamical systems based on an invariant set of fixed points (the intersections of all nullclines) has yielded very important local information which had global implications. For example, under some conditions, if a dynamical system has a fixed point with a homoclinic orbit, it will exhibit complex chaotic dynamics (e.g. Shilnikov bifurcation [117], and Smale-like maps which contain homoclinic points [34, 78]).

The limitations on these two avenues of analysis is that dynamical systems that manifest chaotic attractors that are of same genus often have strange-attractors with significantly different shapes. Is there possibly a complementary analysis, a middle-ground, that lies between the focus on fixed points with the focus on global topology? Such an analysis would be based on local behavior but yield global information about the shape of an attractor that complements the genus classification.

Strange attractors are flows, which we can image only by taking numerical snapshots. Under a wide range of parameters, these flows are dominated by vortex-like behavior that hasn't been quantitatively exploited yet. The Rössler attractor, for example, displays a vortex-tube structure that looks remarkably similar to a tornado (Figure 2.1). We will study these vortex tubes in greater detail in the next two chapters, and find that they can be described by extending Poincaré's focus on fixed points in a way which is complementary to the topological classification program.

In order to do so, we need to draw upon some of the work done in the field of fluid dynamics to find a rigorous definition of vortex tubes. To date, there is no consensus on the exact mathematical definition of a vortex, and we have a number of competing definitions to choose from. In this chapter we will briefly review a number of these definitions in the context of an application to strange attractors.

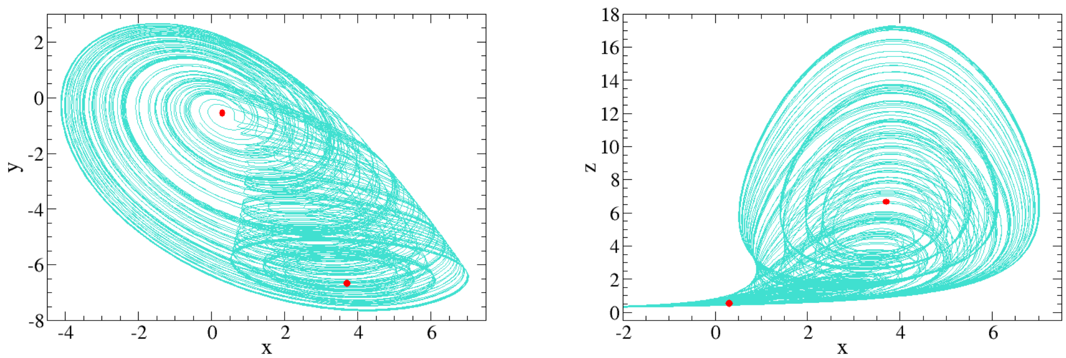

Figure 2.1: The Rössler strange attractor for parameter values $a = 0.0556$, $b = 2.0$, $c = 4.0$. The fixed points for this system are shown as dots.

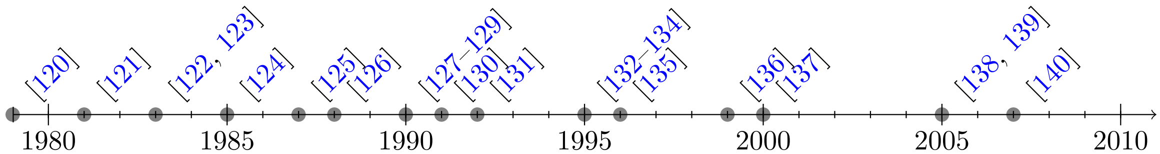

Figure 2.2: Chronology of selected publications on vortex core definition from 1979 to 2011.

2.1 Qualitative Definitions of Vortex Tubes

Considering that computational resources were not widely available to researchers until the 1980s, it is not too surprising that the debate over an adequate definition of a vortex became increasingly important in that decade.

A tornado might perhaps be the most obvious example of a vortex tube, as it nicely satisfies Lugt's intuitive definition: rotating motion of a collection of particles around a common center [120]. In the early days of work on computational fluid mechanics, vortexes were found by visually inspecting graphs of the results. In this case, the standard was that of Justice Stewart: "I know it when I see it". This definition has a number of serious problems, such that it isn't invariant, i.e. it only works if we are in the frame of reference of the tornado [140], and that it depends on viewing angle [127].

Amplitude Thresholding [121, 122] is a more numerically oriented attempt at quantifying the presence of a vortex in which a spectral simulation of isotropic turbulence is used to pick out identifying signatures of a vortex, but this method is not systematic and impractical at the higher resolutions that are common today [131]. As recently as 1990, researchers were still using visual inspection to identify vortex tubes [128], but since the capacity of data storage, computational power, and numerical resolution has grown considerably, such methods are no longer useful.

Another method for identification invokes the fact that at the center of an idealized vortex, the pressure reaches a local minimum. If we were to imagine being swept up by a tornado, the most preferential position would be the very core of the tornado, just as the eye of a hurricane is the safest place to be within such storms. The eye of a hurricane is where the lowest pressure can be found for the entire system [141]. Using pressure minimums to identify vortex cores turns out to fail in systems with large pressure gradients [132]. Due to instances of unsteady irrotational straining, which induces false positives for vortex identification, and viscous effects which can create false negatives where a vortex should be located, the pressure minima method was found to be unsatisfactory for a general definition of vortex curves [139].

None of these methods would be suitable for application to strange attractors. What is needed is a systematic method of identifying vortex tubes.

2.2 Quantitative Definitions of Vortex Tubes

Vortex curves were first observed numerically [131] in the 1980s by Siggia [121] and Kerr [122]. These curves were found using amplitude thresholding (plotting only those velocity vectors which exceed a certain amplitude) and were spotted by graphically plotting the results. This rough method is unsuitable for cases of high Reynolds number[1] and is quite limited for numerical reasons, as specified in the previous section. In this section, we look at systematic mathematically driven methods for defining vortex tubes.

[1] Reynold's number is a dimensionless number that gives a measure of the ratio of inertial forces to viscous forces; in other words, when the magnitude of inertial forces greatly exceeds that of viscous forces, this method does not work.

2.2.1 Vorticity Magnitude Selection

The most basic mathematical definition of vorticity is simply,

$$\vec{\omega} = \nabla \times \vec{u} \tag{2.1}$$

where u is the local velocity field which is determined by the Navier-Stokes Equations [142],

$$\rho\left(\overbrace{\frac{\partial u_j}{\partial t}}^{\text{Acceleration}} + \overbrace{u_k\frac{\partial u_j}{\partial x_k}}^{\text{Convection}}\right) = \overbrace{-\frac{\partial p}{\partial x_j}}^{\nabla\text{Pressure}} + \overbrace{\frac{\partial}{\partial x_j}\left(\lambda\frac{\partial u_k}{\partial x_k}\right) + \frac{\partial}{\partial x_i}\left[\mu\left(\frac{\partial u_i}{\partial x_j} + \frac{\partial u_j}{\partial x_i}\right)\right]}^{\text{Viscosity terms}} + \rho f_j \tag{2.2}$$

where p is pressure, ρ is fluid mass density, $\vec{f}$ is additional forces acting on the liquid, and λ, μ are viscosity coefficients. Since the flows that we will be dealing with are those corresponding to strange attractors, we need not delve too deeply into the details of the Navier-Stokes Equations.

Vorticity Magnitude [124, 125, 129, 131, 136] is one of a number of methods based on isosurfaces of scalars (in this case, $\vec{\omega} \cdot \vec{\omega}$). Villasenor and Vincent [131], who developed this method in greater sophistication than previous researchers, were motivated by storage and processing limits in computation which are still relevant when applied to samples larger and more detailed than were possible in 1992. They were also motivated by data storage and access limitations which are no longer exceedingly relevant. Using the mathematically rigorous concept of "skeleton" developed by Motzkin [143] in the field of mathematical morphology, and starting with a point within the vortex tube (which must be known a priori), the algorithm searches for the vortex tube in the next time increment in a region near its position in the previous time step.

In order to select the starting point inside the vortex tube, and based on statistical/numerical analysis by Vincent and Meneguzzi [144] (but note that Lugt [120] found that for planar wall-bounded flows, the maxima and minima of the vorticity vector occur only on the "wall"), the algorithm detects regions of highest magnitude in vorticity as defined by Equation 2.1. Upon finding a local maximum, the method searches within a spherical neighborhood for other points which could be considered centers of a vortex tube, terminating the search upon reaching a minimum threshold.

This method has a number of weaknesses, including the fact that it will often lose track of the tubes when they pass through high-density regions. Another weakness is that regions of high vorticity magnitude don't necessarily correspond to vortex tubes, such as in the case of flow whose shear is comparable to the vorticity magnitude with the tube [120, 132], the previous mentioned case of planer wall-bounded flows[120], and in turbulent boundary layers[145].

In regards to potential application to the dynamical systems characterized by strange attractors, we would prefer to use analytical means of identifying vortex tubes, using methods such as vorticity magnitude selection for cases where only experimental data is available. The most ideal situation would involve having full state information, through, say, the use of laser-Doppler anemometry [146–148]. A more realistic situation will involve only possessing one dimension of data and having to apply the techniques of embedding in order to recreate a strange attractor, and we will examine the application of some of the results of vortex detection on these systems in a later section.

Banks and Singer [133] use vorticity as a means of finding vortex tubes, combining the pressure minima method with a detection of local vorticity. Starting from a point on the vortex curve, they apply a numerical time step in the direction of vorticity. They then scan a nearby neighborhood in a plane perpendicular to the direction of vorticity at this step, searching for pressure minima. If the predicted step is not the center of the minima in this test plane, they move the next step to that minima. While this method improves that of the pressure minima method in that it incorporates a detection of vorticity direction, it can also fail in systems with large pressure gradients.

2.2.2 Dynamical Criteria

Vorticity magnitude, $\|\omega\|$, has been used as a measure for vortex tubes [124, 125], but gives false positives in turbulent and sheared flow [132] and in the case of walled containers, it has been shown that the maximum and minimum of $\|\omega\|$ is found at the wall boundaries [120].

A class of methods has been developed based on the velocity-gradient tensor, $\nabla\vec{u}$. As early as 1953, Truesdell [149] first formulated the concept of separating the velocity-gradient tensor into symmetric and antisymmetric parts,

$$\nabla \vec{u} = \overbrace{\mathbf{S}}^{\text{Strain-rate Tensor}} + \overbrace{\mathbf{\Omega}}^{\text{Vorticity Tensor}} \tag{2.3}$$

with

$$S = \frac{1}{2}\left(\nabla \vec{u} + (\nabla \vec{u})^T\right) \tag{2.4}$$

The diagonal entries of S are the normal strain rates, and the non-diagonal entries are the shear strain rates,

$$S_{ij} = \frac{1}{2}\left(\frac{\partial u_i}{\partial x_j} + \frac{\partial u_j}{\partial x_i}\right) \tag{2.5}$$

The vorticity tensor,

$$\Omega = \frac{1}{2}\left(\nabla \vec{u} - (\nabla \vec{u})^T\right) \tag{2.6}$$

is so named because its elements are those of the vorticity vector, i.e.,

$$\Omega_{ij} = \frac{1}{2}\left(\frac{\partial u_i}{\partial x_j} - \frac{\partial u_j}{\partial x_i}\right) \tag{2.7}$$

It can be shown [132, 142] that the defining dynamical equation for ω is given by

$$\frac{D\omega_i}{Dt} = S_{ij}\omega_j + \nu \nabla^2 \omega_i \tag{2.8}$$

Here,

$$\frac{D}{Dt} = \frac{\partial}{\partial t} + \mathbf{v} \cdot \nabla \tag{2.9}$$

is the convective derivative (also known as the Lagrangian derivative, the substantive derivative [150], material derivative, and the Stokes derivative, among other names) describing the transport and time dependence of a given vortex. Equation 2.5 is, again, is the rate-of-strain tensor relaying "tearing" information, and $\nu \nabla^2 \omega_i$ relates small scale kinematic viscosity effects of tearing and reconnecting [131]. In 1956, Betchov [151] was the first to point out that equation 2.5 is a symmetric matrix likely to have two positive eigenvalues and one negative eigenvalue, where the sum of all three eigenvalues is required to be zero by the in-compressibility constraint, suggesting that vortex structures might have a sheet-like structure under idealized conditions of uniform and constant strain fields over the vortex structure. She et al. [128] found that in more realistic situations, with nonuniform strain fields, results in a dominance of one of the positive eigenvalues over the other as previously predicted by Ashurst et al. [152]. The result is that vortex structures tend to evolve in tube-like shapes.

Jeong and Hussain (1995) [132] propose a method based on the symmetric/antisymmetric decomposition of the velocity-gradient tensor. They calculate the strain-rate transport equation to be

$$\frac{DS_{ij}}{Dt} - uS_{ij,kk} + \Omega_{ik}\Omega_{kj} + S_{ik}S_{kj} = -\frac{1}{\rho}p_{ij} \tag{2.10}$$

where the latter is the pressure Hessian and contains information on local pressure extrema. If a point is a local pressure minimum, then the the tensor p_{ij} has two positive eigenvalues at that point [140]. This method supposes that we can ignore the irrotational straining and viscous effects such that,

$$-\rho\left(\Omega_{ik}\Omega_{kj} + S_{ik}S_{kj}\right) = p_{ij} \tag{2.11}$$

The vortex is defined as a connected region under the condition that $S^2 + \Omega^2$ has two negative eigenvalues (the swirling plane). The criteria has been named the λ_2-method, due to the fact that because $S^2 + \Omega^2$ is real and symmetric, its three eigenvalues $\lambda_1 \geq \lambda_2 \geq \lambda_3$ are all real, and if $\lambda_2 < 0$, then $\lambda_3 < 0$ and the corresponding point belongs to a vortex. Unfortunately, this method falters when multiple vortices coexist relatively close by [139]. Other criteria based on the symmetric and antisymmetric decomposition of the velocity-gradient tensor, such as the Q and Δ criteria, fair worst in capturing the location of vortex tubes, and we leave their description to the references [139].

2.2.3 Eigenvector Method

The Eigenvector Method [134] is the primary one we chose to apply to chaotic flows. The advantage of this method is computational simplicity coupled with a fair degree of dynamical verisimilitude. While this method is considered an imperfect approximation of the method we'll outline in the next section, it produced satisfactory results when applied to a wide number of strange attractors.

This method invokes a linearization at non-fixed points in the dynamical system, as does the λ_2 method and the parallel vectors method of the next section. We recall from Chapter One that only for hyperbolic fixed points do we have any guarantee that the local linearized dynamics are topologically conjugate to the true dynamics of the system. While it turns out to often be the case that linearization can tell us much about the behavior of the system nearby, this method will frequently fail when the system is highly nonlinear [153].

In dynamical terms, this method proposes to identify vortex curves with the set of points which obeys the following condition,

$$J\vec{u} = \lambda\vec{u} \tag{2.12}$$

Where J is the Jacobian of the velocity vector u. In mechanical terms, this consists of points where the acceleration vector is parallel to the velocity vector. As we will see in the next chapter, this method produces excellent predictions for the overall shape of strange attractors, though it intersects these attractors at certain points for a fairly wide range of parameters.

2.3 Parallel Vectors Method

Roth and Peikert (hereafter RP) [135, 153], survey various methods for visualization of flow for turbomachinery design, giving specific attention to eigenvector methods for finding vortex core lines.

While the mathematical definition of vorticity as a vector field, $\vec{\omega} = \vec{\nabla} \times \vec{u}$, [154], captures the circulatory nature of vorticity, RP further specify that that curving flows should only be considered vortices if the flow is both circularly bent (e.g. by an array of turbine blades) and “detaches” from the overall stream of fluid. We take this to mean that the area of swirling flow disrupts the smoothness of the flow from which it originates.

The Parallel Vectors Method (PVM) was designed to be a more sensitive measure for vortex curves than was the Eigenvalues Method. RP were particularly focused on turbomachinary flow fields, where slowly rotating curved vortices are often not detected by other methods.

Instead of using only the first derivative of the velocity field, Jv, RP also invoke the second derivative,

$$\vec{b} = \mathbf{J}\mathbf{J}\vec{u} + \mathbf{T}\vec{u}\vec{u} \tag{2.13}$$

Here, J is the Jacobian of the velocity vector, as in previous cases, but we also have the term T, a tensor defined by,

$$T_{ijk} = \frac{\partial^2 u_i}{\partial x_j \partial x_k} \tag{2.14}$$

This method proposes to identify a vortex tube along a line where $\vec{b}$ is parallel to $\vec{u}$,

$$\mathbf{J}\mathbf{J}\vec{u} + \mathbf{T}\vec{u}\vec{u} = \lambda\vec{u} \tag{2.15}$$

that is, whenever the second derivative of the velocity field is parallel to the velocity field. Here again, λ is a continuous variable that can be parametrized along the curve.

While this method can be seen as a higher order form of the Eigenvalue Method, computational considerations made it an impractical choice for a vortex detection method for strange attractors. For example, for one strange attractor based on the Thomas System, the analytical algebraic solution from the Eigenvalue Method was output as a text file of many dozens of megabytes in size. The second-order refinement of the PVM, would thus prove to be beyond our current computational capacity.

2.4 Conclusion

While we haven't exhausted the list of vortex detection methods to be found in the literature, we have covered some of the more prominent methods used, and particularly, ones which might have utility for strange attractors. We close this chapter with a summary table of a number of methods for vortex detection. The interested reader can find a more comprehensive listing in Jiang et al. 2005 [139] and Kolar 2007 [140], amongst other sources.

Table 2.1: Various methods, from the literature, for finding vortex core lines [135]. None of these methods are universally successful, and all fail when high levels of non-linearity are involved.

Name	Methodology	Weakness
2D-Graphical representation[127]	Visualization of flowfield	potentially ambiguous, not systematic
Amplitude Thresholding[121, 122]	Thresholding & plotting	Not systematic
Coloration of Field Lines[128]	emphasis of few chosen field lines	needs a priori knowledge of location
Vorticity magnitude[124, 125, 129, 131]	Find regions of high vorticity magnitude	not always imply swirling motion (e.g. sheared flow)
Helicity Density[127]	Projection of curl onto flow vector	bent flow, uneven vector fields give false positives
Minima of pressure	Low pressures at vortex (e.g. tornado core)	fails in flow with large pressure gradients; no sense of swirl
λ_2-method [132]	2/3 Jacobian eigenvalues negative	condition not unique to vortices, low resolution
Streamlines [130]	at $\vec{v} = 0$, integrate towards eigenvectors	unstable and not true for all vortices
Singer & Banks [133]	streamline (vorticity field) + pressure minima	can fail for same reasons as minima method
Curl $\parallel$ flow	where vorticity is parallel to velocity vector	doesn't work for all fields
Single Eigenvector$\in \mathbf{R}$ [135],[134]	one real eigenvalue of Jacobian $\parallel$ to flow	only works properly with linear fields

Chapter 3: Application of Vortex Core Lines to Nonlinear Dynamics: A New Insight into the Morphology of Strange Attractors

The Rössler and the Lorenz systems are defined by dynamical equations which, on first sight, do not look as radically different as do their resulting attractors. The Rössler flow[42],

$$\overrightarrow{V}\begin{pmatrix} \dot{x} \\ \dot{y} \\ \dot{z} \end{pmatrix} = \begin{matrix} -y-z \\ x+ay \\ b+z\left(x-c\right) \end{matrix} \tag{3.1}$$

has one less non-linearity than the Lorenz[17] flow,

$$\overrightarrow{V}\begin{pmatrix} \dot{x} \\ \dot{y} \\ \dot{z} \end{pmatrix} = \overrightarrow{\Im}\begin{pmatrix} f_1\left(x,y,z\right) \\ f_2\left(x,y,z\right) \\ f_3\left(x,y,z\right) \end{pmatrix} = \begin{matrix} \sigma\left(y-x\right) \\ Rx-y-xz \\ -bz+xy \end{matrix} \tag{3.2}$$

These equations result in topologically distinct strange attractors with qualitatively different mechanisms for the creation of chaotic flows[88]. Unless we might be inclined to point towards this additional non-linearity as the source of the topological differences, we have the example of the Lorenz system of 1984, which has more nonlinear terms than either of the two previous systems,

$$\begin{aligned} \overrightarrow{V}\begin{pmatrix} \dot{x} \\ \dot{y} \\ \dot{z} \end{pmatrix} &= \overrightarrow{\Im}\begin{pmatrix} f_1\left(x,y,z\right) \\ f_2\left(x,y,z\right) \\ f_3\left(x,y,z\right) \end{pmatrix} \\ &= \begin{matrix} -y^2-z^2-a(x-F) \\ -y+xy-bxz+G \\ bxy+xz-z \end{matrix} \end{aligned} \tag{3.3}$$

and yet is more similar to the Rössler attractor, topologically, than it is to the Lorenz attractor. Thus it is clear that there is nothing superficially obvious about the form a chaotic attractor will take based on the form of its dynamical equations.

The problem of finding, from the dynamical equations, qualitative information about the morphological features of the trajectories of dynamical systems, is a more general problem in physics that has been solved for a small set of linear systems. It was Poincaré who made the first substantial contribution to addressing this problem with nonlinear dynamical systems. Poincaré found that the equilibrium points of nonlinear dynamical systems provide positions around which trajectories may either tend towards, or diverge away from. These so-called fixed points of the system comprise a zero-dimensional invariant set.

The problem with fixed points is that although their relative positions do provide some indication of the global organization of trajectories, such information is quite limited. Indeed, although these fixed points suggest a distinctly different topology for the Lorenz attractor than that of the other two systems, they tell us little about what sort of distinctions we might expect from the Rössler and Lorenz 1984 systems.

Furthermore, from the Hartman-Grobman theorem[68, 69], we find that the quantitative information which fixed points impart to us about the behavior of the system is limited to a small local neighborhood. That is, given a dynamical system with hyperbolic fixed points, the linearization around a generic fixed point is locally topologically conjugate to the original flow. Thus in seeking to obtain global information about the behavior of dynamical trajectories, the fixed points by themselves offer very limited insight.

Other researchers, such as Andronov, Tikhonov, Levinson, Wasow, Cole, O'Malley and Fenichel [155] have focused on higher dimensional invariant sets such as the slow invariant manifolds of singularly perturbed dynamical systems. These higher dimensional invariant sets can be quite useful in the analysis of systems in which the slow-fast partition offers a realistic simulacrum of the actual system. In systems where such a partition is not applicable, we need other tools to help us understand the morphology of the dynamical trajectories.

The work of Sujudi and Haimes [134] in producing an analytical method to locate "vortex core curves" (the Eigenvalue Method of Chapter 2) is here extended to the realm of nonlinear dynamical systems. The concept was independently considered by two researchers [155], one who sought to directly apply the "vortex core curves" method, and another who came upon the concept in the context of classical differential geometry. In this chapter, we outline the methods used to derive these "core curves", show these curves for a wide range of chaotic attractors, and point towards future research for these curves for driven dynamical systems. Our method has the advantage of being fully analytical, giving exact parametrized results, and limited only by computational time. As we will see, these vortex core curves (also called connecting curves, as they connect fixed points) provide a strong indication of the global morphology of the dynamical flow of systems, well beyond the information provided by the fixed points themselves.

3.1 Algebraic method for deriving connecting curves

3.1.1 Dynamical restrictions

We focus on systems of differential equations defined in a compact E included in $\mathbb{R}^n$ with $\vec{X} = [x_1, x_2, ..., x_n]^t \in E \subset \mathbb{R}^n$:

$$\frac{d\vec{X}}{dt} = \overrightarrow{\Im}(\vec{X}) \tag{3.4}$$

where $\overrightarrow{\Im}(\vec{X}) = \left[f_1(\vec{X}), f_2(\vec{X}), ..., f_n(\vec{X})\right]^t \subset \mathbb{R}^n$ defines a velocity vector field in E whose components f_i are assumed to be continuous and infinitely differentiable with respect to all x_i, i.e., are real-valued C^∞ functions (or C^r for r sufficiently large) in E and which satisfy the assumptions of the Picard-Lindelöf/Cauchy-Lipschitz theorem [156].

We further restrict our analysis to systems which contain fixed points (the Sprott A attractor, for example, does not have fixed points [157]). We will consider non-autonomous systems (systems that depend explicitly on time) in the next chapter.

A solution to this system, which is a parametrized trajectory curve or integral curve, is denoted by $\vec{X}(t)$. This trajectory curve gives the previous and future evolution of the state of the system in a deterministic way. We consider systems here in which the trajectory is not analytically derivable, that is, systems in which the evolution can only be known with limited certainty for a small neighborhood of time centered around the present time of sampling. In such systems, where sensitivity to initial conditions dominates the deterministic behavior, we must numerically integrate the system to find the general shape of the corresponding chaotic attractor. Although we take it for granted that our integration, if done using well studied and understood numerical methods, produces an accurate facsimile of the true attractor, the problem remains that for such systems, a truly accurate numerical integration would require infinite precision. Indeed, it has only been in recent years that mathematicians have proven that numerical simulations of the Rössler and Lorenz attractor represent the true chaotic systems despite the lack of infinite precision [158–160] using normal-form theory and validated interval arithmetic[1]

We represent the instantaneous "velocity vector" of such a dynamical system as

$$\overrightarrow{V}(t) = \frac{d\vec{X}}{dt} = \overrightarrow{\Im}(\vec{X}) \tag{3.5}$$

The instantaneous velocity vector $\overrightarrow{V}(t)$ is tangent to the trajectory except at the fixed points, where it is zero. We note here that the use of the term "velocity vector" does not imply that the description of a physical velocity. Rather, it is a means of abstracting the multitude of dynamical systems by applying a short-hand term to a vector field that, for instance, may represent the instantaneous evolution of a chemical system or the synaptical potentials of a neuron.

We define an "acceleration vector" as a vector function $\vec{\gamma}(t)$, corresponding to the instantaneous acceleration vector of M at the instant t.

$$\vec{\gamma}(t) = \frac{d\overrightarrow{V}}{dt} \tag{3.6}$$

For reasons which will become obvious below, we wish to recast the acceleration vector in terms of

[1] Computer assisted proofs remain controversial in some quarters of the mathematical community for philosophical and technical reasons. Another related note is that the application of the Berman-Williams Theory has only recently been rigorously proven valid for the Lorenz attractor[161] and yet has long been successfully applied in nonlinear dynamics for multiple attractors[36].

the Jacobian of the dynamical equations, assuming $\frac{\partial x}{\partial t} = 0$,

$$\frac{d\overrightarrow{V}}{dt} = \frac{\partial \overrightarrow{\Im}}{\partial \vec{X}} \frac{d\vec{X}}{dt} = J\overrightarrow{V}(t) \tag{3.7}$$

We emphasize here that this localization of the vector field, with the introduction of the Jacobian into the above equation, is not guaranteed to be topologically conjugate to the true system unless conditions of the Hartman-Grobman theorem are satisfied.

3.1.2 Vortex Core Curves

When a dynamical system has fixed points which are hyperbolic (the real parts of the eigenvalues are nonzero), the Jacobian of the vector field defines the local stable and unstable manifolds [68, 69]. For the $\mathbf{R}^3$ case, when such a fixed point produces an unstable manifold that also has nonzero imaginary parts for two out of the three eigenvalues, (in the form of a complex conjugate pair of eigenvalues), with the other being wholly real, the unstable/stable manifold described by the eigenvector corresponding to the purely real eigenvalue will be perpendicular to the stable/unstable plane created by the complex-conjugate pair.

This has been well-described as somewhat analogous to the inner core of an idealized tornado where the absolute center of the wind flow will be vertical with zero rotation.

In our dynamical system, if we could imagine following the eigenvector produced by the real-valued eigenvalue, we would be traveling in a direction in which the velocity and acceleration fields are perfectly parallel. This is mathematically expressed by the equation[135],

$$J\overrightarrow{V} = \lambda\overrightarrow{V} = \vec{\gamma} \tag{3.8}$$

The eigenvalue condition can be written

$$\gamma_i = \frac{d}{dt} f_i = \frac{\partial f_i}{\partial x_s} \frac{dx_s}{dt} = J_{is} f_s = \lambda f_i \qquad 1 \leq i, s \leq 3 \tag{3.9}$$

In phase-space representation, the above equation can be visualized as the intersection of the surfaces defined

$$\frac{\dot{f}_1}{f_1} = \frac{\dot{f}_2}{f_2} = \frac{\dot{f}_3}{f_3} = \lambda \tag{3.10}$$

When we project the eigenvalue solution $\lambda : (x_1, x_2, x_3, \lambda)$ onto phase space in $\mathbb{R}^3$, or take the intersection of the three 3-surfaces defined by Equation 3.10, we have a vortex core curve which, as we shall show, provides a sort of skeletal structure for the chaotic attractor.

Where this vortex curve method has been applied to its native field of fluid dynamics, it has been found to be a reasonable approximation to true vortex core phenomenon when nonlinearities are small, but it becomes less useful as nonlinearities become more important [135]. In the case of the dynamical flows we are considering, we take a less physical view of this curve and see it as a new tool for outlining the shape of strange attractors from a purely analytical direction.

3.2 Computer Algebraic Solutions using Maple

It may seem odd to be discussing purely analytical solutions in the context of computer packages. Even though our solutions to the vortex core equations are purely analytical in form, they are exceedingly complex. Of all the solutions we have produced, only that for the Rössler system is close to being an equation one might solve with pencil and paper, given enough time. For the Rössler system, the vortex curve is parametrized by one of the dimensions of phase space (we choose x) and is the solution to the equation,

$$\sum_{j=0}^{5} D_j \lambda^j = 0 \tag{3.11}$$

where,

$$
\begin{aligned}
D_5 &= a \\
D_4 &= 2a(c-a-x) \\
D_3 &= ax^2 - 2acx + 4a^2x - 4a^2c + a^3 + c + 2a + ac^2 \\
D_2 &= -2a^2x^2 + x^2 - 2a^3x - 2cx + 4a^2cx - 4ax \\
&\quad +ab + 2ac - 2a^2c^2 + 2a^3c + c^2 - 2a^2 \\
D_1 &= a^3x^2 + 4a^2x - 2a^3cx - 2a^2b + a + b + c - 3a^2c + a^3c^2 \\
D_0 &= x^2 - a^2x^2 + 2a^2cx - 2cx - 2ax + ac - a^2c^2 + c^2 \\
&\quad -ab + a^3b
\end{aligned} \tag{3.12}
$$

We emphasize that this equation is an analytical solution which gives exact results parametrized by x.

3.2.1 Computer assisted calculations

Maple is a computer algebra system which has become well established in academia[2]. Maple is capable of a great many analytical and numerical calculations whose complexity or size would otherwise put them out of reach of a solution. We will briefly outline our method of using Maple to solve the vortex curve equations, presenting the Rössler system as one of the simpler examples. We do not wish to misguide readers into thinking that all such solutions were so simple. In fact, for the more complicated systems, the algebraic output becomes large enough to fill a text file dozens of megabytes in size. The most complicated system we considered, the Thomas system, took twenty eight days of computer time on a seven-processor i686 computer. In order to apply these methods to more complicated systems, we were required to split the Maple code into multiple components, sharing the output between components by printing to file so as to not overwhelm program memory space (which causes Maple to crash and terminates the calculation).

[2]In fact, The Symbolic Computing and Problem-Solving Environment (PSE) group here at Drexel University have contributed to the development of Maple under the direction of Bruce Char, who was a member of the original development team of Maple at the University of Waterloo in the early 1980s.

We begin by initializing Maple with the **LinearAlgebra** and **StringTools** packages and defining our dynamical equations,

```
restart:
with(LinearAlgebra):
with(StringTools):
v1 := -y-z;
v2 := x+a*y;
v3 := b+z*(x-c);
```

Our next step is to properly pose the vortex curve equation to the Maple software, which we do so using **LinearAlgebra** tools,

```
v := Vector(3, [v1, v2, v3]);
L := proc (X) options operator, arrow; v[1]*(diff(X, x))+v[2]*(diff(X, ...
    y))+v[3]*(diff(X, z)) end proc:
Lv := Vector(3, [seq(L(v[i]), i = 1 .. 3)]);
```

this produces the output which represents the left-hand side of Equation[REF EQ],

$$Lv := \begin{bmatrix} -x - ay - b - z\,(x - c) \\ -y - z + (x + ay)\,a \\ (-y - z)\,z + (b + z\,(x - c))\,(x - c) \end{bmatrix}$$

We now construct the solution to the Vortex curve equation with the command,

```
sol := solve([seq(Lv[i] = lambda*v[i], i = 1 .. 3)], [lambda, y, z]);
```

where we have arbitrarily chosen x as the parameter value of the solution. The output of the above command is relatively large and is omitted for brevity. A key part of the output is that the solution for (λ, y, z) is expressed in terms of the Maple `RootOf` function. In the case of the Rössler system, it is trivial to extract this function from the solution by hand; for the more complex systems we study later, it was necessary to construct computer code to automatically extract this function from the output results. This `RootOf` is then aliased to a simpler variable in order to simplify the code,

```
alias(R1=RootOf(a*_Z^5+(2*a*c-2*a*x-2*a^2)*_Z^4+(a^3-4*c*a^2+4*x*a^2-2*c*a*x
                                              +2*a+c^2*a+a*x^2+c)*_Z^3
             +(-2*a^3*x+2*c*a^3-2*a^2+4*x*c*a^2-2*a^2*x^2-2*c^2*a^2
                                   +a*b+2*a*c-4*a*x+c^2-2*x*c+x^2)*_Z^2
        +(c^2*a^3-2*x*c*a^3+a^3*x^2-2*a^2*b-3*c*a^2+4*x*a^2+a+b+c)*_Z
      +a^3*b-c^2*a^2+2*x*c*a^2-a^2*x^2-a*b+a*c-2*a*x+c^2-2*x*c+x^2)):
```

and all possible solutions are indexed with the command,

```
soln:=(x,i)->allvalues(rr)[i];
```

We must also extract the solutions for (λ, y, z) from the output and define those as separate functions, say, (λ, yy, zz). Again, for the Rössler system, extracting these components is fairly trivial, but for more complicated systems it became necessary to automate that process.

Up to this point, everything we have done with Maple has been analytical, producing a solution $(\lambda(x), y(x), z(x))$ parametrized by x. In order to extract a solution for a specific state of the Rössler system, as defined by parameters (a, b, c), we need to use the Maple `evalf` routine, which is numerical in nature. Due to the complexity of the evaluating this function, it becomes necessary to have Maple use a higher precision than is standard for the RootOf function, so we set `Digits := 30:` with good results. We finally run a loop for each of the five roots to extract a specific solution:

```
for i from 1 to 5 do
file:=Join(["machine_",convert(i,string),".dat"],"");
fz:=fopen(file,WRITE):
```

```
for x from −9 by 0.01 to 9
do
Re(yy);
Im(yy);
Re(zz);
Im(zz);
Re(lamb);
Im(lamb);
i;
printf("All solutions %f %f %f %f %f %f %f %d \n", x, Re(yy),Im(yy),Re(zz),Im(zz), ...
    Re(lamb), Im(lamb),i):
if Im(var) = 0 then
printf(fzz,"Real solutions %f %f %f %d \n", x,yy,zz,i):
end if
end do:
unassign('x', 'var'):
end do:
```

3.3 Results

3.3.1 Rössler model

For the Rössler system, the curve along which $J\vec{V} = \lambda\vec{V}$ depends on the three control parameters (a, b, c) and is parametrized by one of the three phase space coordinates. Choosing x as the phase space coordinate, the eigenvalue λ satisfies a fifth degree equation

$$\sum_{j=0}^{5} D_j \lambda^j = 0 \tag{3.13}$$

The coefficients D_j are listed Equation 3.12. At each fixed point, the value of λ is the value of the real eigenvalue of the Jacobian matrix at that fixed point. The coordinates y and z are expressed

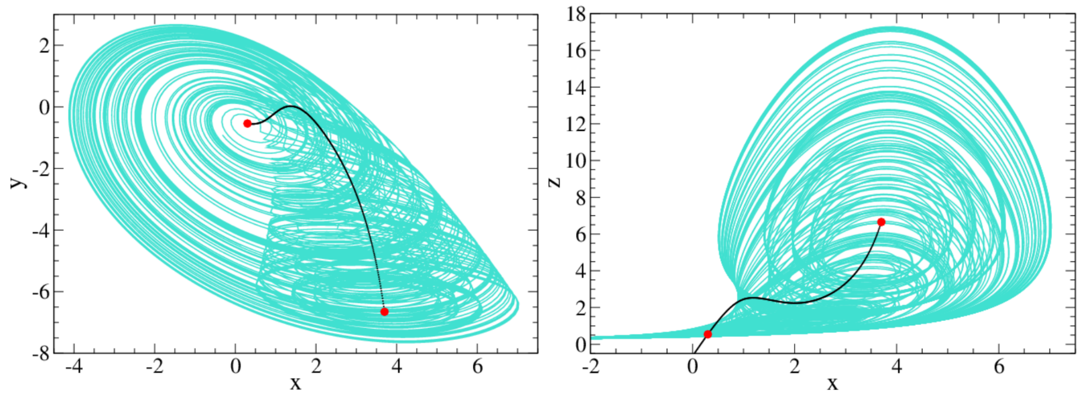

Figure 3.1: Connecting curve of the Rössler model. The curve intersects the attractor, as seen in the x-z projection. Parameter values: $(a, b, c) = (0.556, 2, 4)$.

as rational functions of x and $\lambda(x; a, b, c)$. These rational expressions are

$$y = \frac{-b - x + ax(c - x) + \lambda x(x - c + a - \lambda)}{a + (c - x)(1 - a^2) + \lambda a(c - x + \lambda - a)}$$

$$z = \frac{+b + x + (\lambda x + ab)(\lambda - a)}{a + (c - x)(1 - a^2) + \lambda a(c - x + \lambda - a)} \tag{3.14}$$

The connecting curve between the fixed points is plotted for the Rössler attractor in Fig. 3.1 for control parameter values $(a, b, c) = (0.556, 2.0, 4.0)$. Two projections are shown. Close to the fixed points, this connecting curve produces excellent results in agreement with the general shape of the Rössler attractor. We have found that the shape of this connecting curve changes very little with a change in parameter, only shrinking or expanding as the attractor shrinks or expands with parameter variation.

As is apparent in the x-z projection, the connecting curve intersects the attractor. This result reinforces an observation made by Roth and Peikert that the "eigencurve", i.e. the connecting curve defined by $J\vec{V} = \lambda\vec{V}$, is not the best possible calculation to identify the vortex curve [153], but as we stated in the previous chapter, it represents a compromise between computational practicality and vortex identification. As we will see in further examples, this curve identifies key features in the structure of a strange attractor.

3.3.2 Lorenz model

As briefly stated in Chapter 1, the strange attractor introduced by Edward Lorenz [17] was designed to study a simplified model of atmospheric dynamics. After having developed non-linear partial differential equations starting from the thermal equation and Navier-Stokes equations, Lorenz truncated them to retain only three modes. The most widespread form of the Lorenz model is as follows:

$$\overrightarrow{V}\begin{pmatrix}\dot{x}\\ \dot{y}\\ \dot{z}\end{pmatrix}=\overrightarrow{\Im}\begin{pmatrix}f_1\left(x,y,z\right)\\ f_2\left(x,y,z\right)\\ f_3\left(x,y,z\right)\end{pmatrix}=\begin{pmatrix}\sigma\left(y-x\right)\\ Rx-y-xz\\ -bz+xy\end{pmatrix} \tag{3.15}$$

where σ, R and b are real parameters.

The solutions for this system are too large to present here. We found that three connecting curves pass through the saddle at the origin: one corresponding to each of the three eigendirections with real eigenvalues. The simplest of these curves is the z-axis, which is simple to compute by hand. This particular curve is also a trajectory of the Lorenz model.

A second heads off to $z \to -\infty$ and has little effect on the attractor. The third connecting curve passes through all three fixed points. This curve is shown in Fig. 3.2 in both the x-y and y-z projections for $(R, \sigma, b) = (28, 10, 8/3)$. When R is increased, the return flow from one side of the attractor to the other exhibits a fold and the connecting curve intersects the attractor at the fold.

The connecting curves present additional constraints on the structure of the Lorenz attractor above and beyond those implied by the location and stability of the fixed points. Specifically, the flow spirals around the connecting curve that passes through the two foci.

3.3.3 Lorenz model of 1984

Lorenz continued to contribute to the field of nonlinear dynamics long after his initial contribution, and in 1984 he proposed a global atmospheric circulation model in truncated form [162]. The

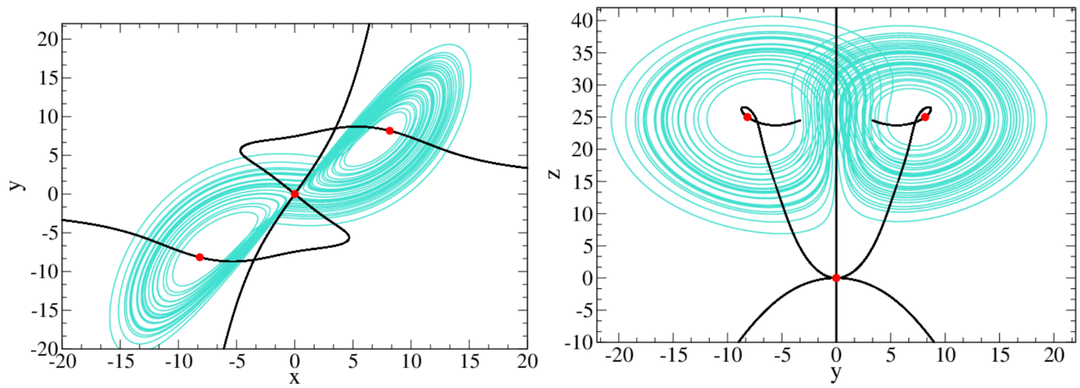

Figure 3.2: Connecting curve of the Lorenz model. One nontrivial connecting curve heads off to $z \to -\infty$ and has little effect on the structure of the attractor. The other nontrivial connecting curve connects all three fixed points, and is plotted extending through the foci. The third connecting curve is the z axis. Parameter values: $(R, \sigma, b) = (28, 10, 8/3)$.

differential equations are,

$$\overrightarrow{V}\begin{pmatrix} \dot{x} \\ \dot{y} \\ \dot{z} \end{pmatrix} = \overrightarrow{\wp}\begin{pmatrix} f_1(x,y,z) \\ f_2(x,y,z) \\ f_3(x,y,z) \end{pmatrix} = \begin{pmatrix} -y^2 - z^2 - a(x-F) \\ -y + xy - bxz + G \\ bxy + xz - z \end{pmatrix} \tag{3.16}$$

In this model the variable x represents the strength of the globally circling westerly wind current and also the temperature gradient towards the pole. Heat is transported poleward by a chain of large scale eddies. The strength of this heat transport is represented by the two variables x and y, which are in quadrature. The control parameters a, F and G represent thermal forcing. The parameter b describes the strength of displacement of the eddies by the westerly current.

In Fig. 3.3 we show two projections of this attractor for control parameters $(a, b, F, G) = (1/4, 4, 8, 1)$ as well as the connecting curve. For this set of parameter values there are three fixed points, only one of which is real at $(x, y, z) = (7.996, -0.00653, 0.0298)$.

The connecting curve passes through this fixed point, but also outlines in dramatic fashion the key features of this attractor, including the central hole and the bending feature seen in the positive y direction.

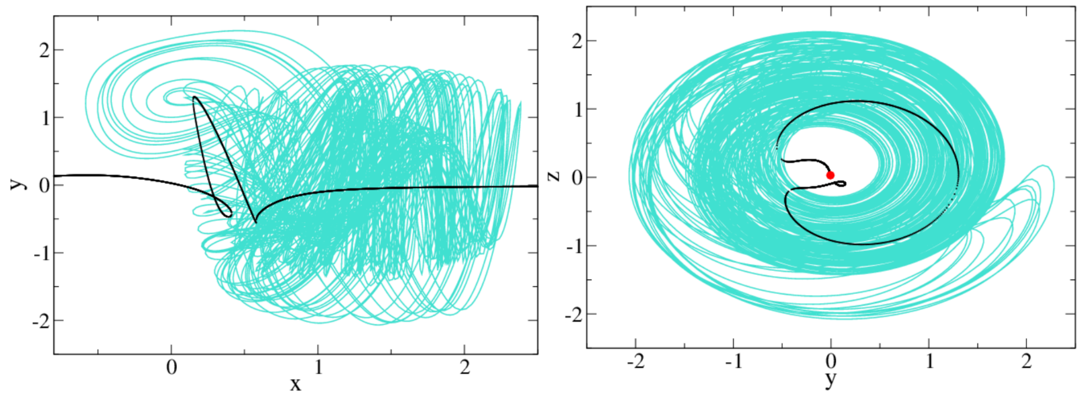

Figure 3.3: Strange attractor generated by the Lorenz global circulation model of 1984. The connecting curve threads through the inside of the attractor, and is caressed by the attractor where the stretching and folding is most pronounced. Parameter values: $(a, b, F, G) = (1/4, 4, 8, 1)$.

3.3.4 Rössler model of hyperchaos

Rössler proposed a simple four-dimensional model in 1979 to study hyperchaotic behavior [163]. This model is

$$\begin{aligned} \overrightarrow{V} \begin{pmatrix} \dot{x} \\ \dot{y} \\ \dot{z} \\ \dot{w} \end{pmatrix} &= \overrightarrow{\Im} \begin{pmatrix} f_1(x,y,z,w) \\ f_2(x,y,z,w) \\ f_3(x,y,z,w) \\ f_4(x,y,z,w) \end{pmatrix} \\ &= \begin{pmatrix} -y-z \\ x+ay+w \\ b+xz \\ -cz+dw \end{pmatrix} \end{aligned} \tag{3.17}$$

Here the state variables are (x, y, z, w) and the control parameters are (a, b, c, d). The resulting connecting curves are shown in Fig. 3.4. The computation was carried out for $(a, b, c, d) =$

$(1/4, 3, 1/2, 1/20)$. The fixed points are shown as large dots along the connecting curve. We thus see that this method of calculating vortex curves extends to higher dimensional systems, as the connecting curves again outline the fundamental shape of the attractor.

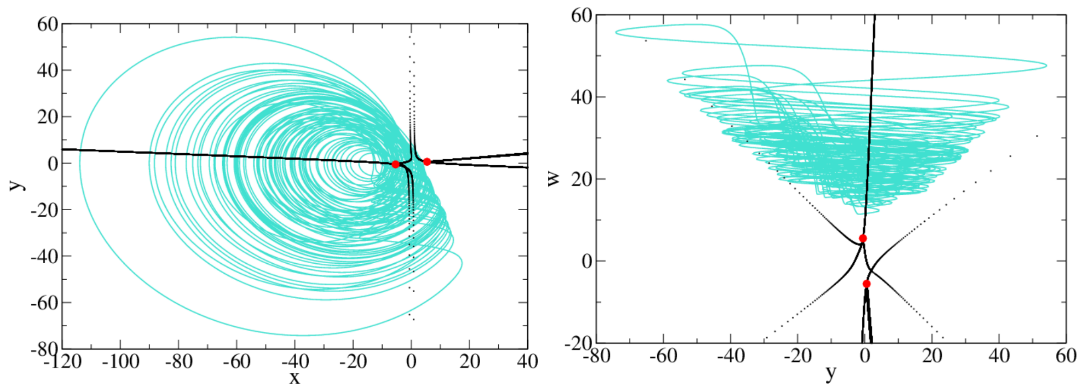

Figure 3.4: Hyperchaotic attractor generated by the 1979 Rössler model for hyperchaos. Parameter values: $(a, b, c, d) = (1/4, 3, 1/2, 1/20)$.

3.3.5 Thomas Model

For our final example, we wanted to examine one of the most complex attractors found in the literature. Thomas proposed the following model of a feedback circuit with a high degree of symmetry [164]:

$$\begin{aligned}\overrightarrow{V}\begin{pmatrix}\dot{x}\\ \dot{y}\\ \dot{z}\end{pmatrix} &= \overrightarrow{\Im}\begin{pmatrix}f_1(x,y,z)\\ f_2(x,y,z)\\ f_3(x,y,z)\end{pmatrix}\\ &= \begin{pmatrix}-bx+ay-y^3\\ -by+az-z^3\\ -bz+ax-x^3\end{pmatrix} \qquad (3.18)\end{aligned}$$

This set of equations exhibits the six-fold rotation-reflection symmetry S_6 about the $(1, 1, 1)$ axis. The symmetry generator is a rotation about this axis by $2\pi/6$ radians followed by a reflection in the

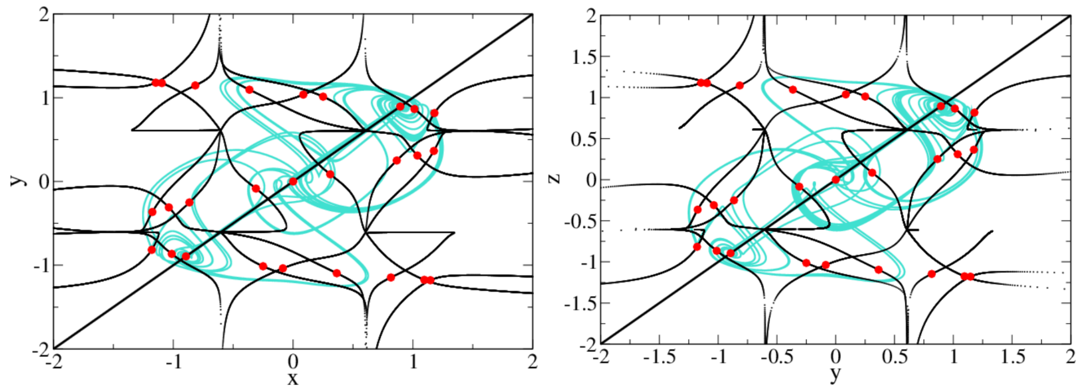

Figure 3.5: Connecting curves for the Thomas attractor. One connecting curve is the symmetry axis $x = y = z$. The remaining connecting curves exhibit the six-fold symmetry of the system and seek out the holes in the attractor. Parameter values: $(a, b) = (1.1, 0.3)$.

plane perpendicular to the axis. The origin is always a fixed point and, for $a - b > 0$, there are two on-axis fixed points at $x = y = z = \pm\sqrt{b - a}$. For $(a, b) = (1.1, 0.3)$ there are 24 additional off-axis fixed points. These fall into four sets of symmetry-related fixed points (sextuplets). One point in each sextuplet is $(0.085, 1.037, 0.309)$, $(0.250, 1.013, 0.865)$, $(0.364, -1.095, 1.175)$, $(1.146, -1.180, -0.816)$. The remaining points in a multiplet are obtained by cyclic permutation of these coordinates: $(u, v, w) \to (w, u, v) \to (v, w, u)$ and inversion in the origin $(u, v, w) \to (-u, -v, -w)$. The chaotic attractor for this dynamical system is shown in Fig. 3.5, along with the symmetry-related connecting curves and the 27 fixed points. One of the connecting curves is the rotation axis. This is an invariant set that connects the three on-axis fixed points. It therefore cannot intersect the attractor. In fact, this set has the same properties as the z-axis does for the Lorenz attractor of 1963 [88].

It is not so clear in two-dimensional images, but the flow of the Thomas system can often be found wrapping itself around the connecting curves, something that is apparent in 3D animations which fly through the attractor. The Thomas system shows both the strengths and limitations of using the Eigenvalue Method to identify Vortex Curves in strange attractors. While it successfully locates the fixed points and regions where the flow has a particularly strong wrapping-around effect, finding the solutions to the eigenvalue equation required large amount of computational resources.

3.4 Conclusion

We have gone beyond the zero-dimensional invariant sets (fixed points) by adapting a definition of vortex curves from fluid mechanics for use with autonomous strange attractors. The resulting curve passes through all real-valued fixed points and outlines structures of the attractor which are not characterized by the fixed points. We have introduced a new way to analyze chaotic attractors which doesn't require numerical integration in order to ascertain general morphological features of the attractor. This method provides a middle ground between Poincaré's program for the analysis of fixed points, and for the topological classification program where attractors are identified by topological invariants.

There exists, however, a class of strange attractors for which this method will not provide satisfactory results. We address this in the next chapter.

Chapter 4: The Search for Vortex Curves for Nonautonomous Systems

A dynamical system is defined by a set of ordinary differential equations which describe the evolution of that system based on its current state. If we denote $\mathbf{x} = (x_1, x_2, \cdots, x_n) \in \mathcal{M} \subset \mathbb{R}^n$ as the state variables in state space $\mathcal{M}$ and $\mathbf{c} = (c_1, c_2, \cdots, c_k)$ as the control parameters, then the dynamical equations can be described as,

$$\frac{d\mathbf{x}_i}{dt} = \vec{F}_i(\mathbf{x}; \mathbf{c}) \tag{4.1}$$

We further classify such dynamical systems as autonomous or nonautonomous:

$$\begin{array}{cc} \text{Autonomous} & \text{Nonautonomous} \\ \forall i \ : \ \frac{\partial F_i}{\partial t} = 0, & \exists i \ \ni \ \frac{\partial F_i}{\partial t} \neq 0 \end{array}$$

In the previous chapter, we identified a characteristic connecting curve for autonomous strange attractors. Our focus now turns to finding a similarly descriptive set of curves for nonautonomous strange attractors, i.e., systems which are explicitly dependent on time in their dynamical equations. We find that the connecting curves used to describe autonomous systems fail to provide useful information for nonautonomous systems, and we propose an alternative based on a variational method.

We begin by using as an example a system that was recently proposed in the scientific literature.

4.1 Dusty Plasma: An Example of a Nonautonomous Nonlinear System

4.1.1 Background

In recent years, an increasing amount of attention has been applied to the properties of dusty plasmas [165–169]. A plasma is an ensemble of electrons and positive ions. When micron and sub-micron sized dust particles are introduced into a plasma, the behavior of the plasma changes considerably [166] as the particles acquire charge. First observed in experiments with argon in glass tubes [170], dusty plasmas have been since theorized about and observed in interstellar space [171, 172], observed in the rings of Saturn [173–176], found to be a major contribution to particulate contamination of semiconductor wafers [177, 178], theorized to negatively affect fusion device operations at high concentrations [179], and pose a potential radiation hazard [180] with fusion reactors. Other observations include dust tails of comets [172], dust streams from Jupiter [172], and noctilucent clouds in Earth's upper atmosphere [181]. Possibly related to the latter observation, dusty plasma has been theorized to be the cause of enhanced polar mesosphere summer radar echoes [182].

4.1.2 Mathematical Description

We can describe the cold inertial dust fluid density $n_d(z,t)$, original charged dust fluid density $n_{d0}(z,0)$, and velocity $u_d(z,t)$ with a density evolution equation (one-dimensional) [165, 183],

$$\frac{\partial n_d}{\partial t} = -n_{d0}\frac{\partial u_d}{\partial z} + \alpha n_d - \frac{\beta n_d^3}{3} \tag{4.2}$$

Here we have assumed that there is only a net drift velocity along the z direction, though there is random motion in the x, y directions which allow for collisions. Equation 4.2 represents a model in which the rate of change in the density of dust is equal to the contributions from the rate of dust grain production plus the contribution due to the dependency of the velocity on position (where the velocity is only taken in the z direction). That is, if we are passing from a region of lower velocity to a region of higher velocity, the density will decrease proportionally to the spacial gradient in the direction of motion. We can rewrite this equation as,

$$\frac{\partial n_d}{\partial t} + n_{d0}\frac{\partial u_d}{\partial z} = \alpha n_d - \frac{\beta n_d^3}{3} \tag{4.3}$$

to better explain the rate of charged dust grain production (right side of Equation 4.3). Dust grain charge is not assumed to be of constant charge, but instead to be a time dependent function. α represents the rate of electron absorption by the dust (electrons are exceedingly faster than ions inside of plasmas and so will dominate charge accumulation on dust particles). β represents the rate of charge loss by dust particles from three-body recombination [184, 185], i.e., an ion-dust particle interaction may result in the loss of an electron from the dust particle to the ion (also see Equation

4.5). The dust momentum equation (one-dimensional) is given as [165, 183],

$$\frac{\partial u_d}{\partial t} = -\frac{q_d}{m_d}\frac{\partial \phi}{\partial z} \tag{4.4}$$

where the electric potential is given by the Poisson equation,

$$\frac{\partial^2 \phi}{\partial z^2} = -4\pi e(Z_i n_i - n_e - Z_d n_d) \tag{4.5}$$

where n_i, n_e represent the ion and electron number density, respectively, and Z_i is the average number of positive charge elements on the ions (Z_d the average number of negative charge elements on the dust). Equations 4.3 and 4.4 are differentiated with respect to time and z to obtain,

$$\frac{\partial^2 n_d}{\partial t^2} - \left(\alpha - \beta n_d^2\right)\frac{\partial n_d}{\partial t} = \frac{n_{d0} q_d}{m_d}\frac{\partial^2 \phi}{\partial z^2} \tag{4.6}$$

Further analysis [165] yields a first order approximation for the potential differential as,

$$\frac{\partial^2 \phi}{\partial z^2} \approx -\frac{4\pi q_d k^2}{k^2 + k_D^2} n_d \tag{4.7}$$

Assuming a fluctuating dust charge given by $q_d = q_{d0}\left(1 + h\cos\gamma t\right)^{1/2}$, and writing $\omega_{pd} = \left(4\pi n_{d0} q_{d0}^2/m_d\right)^{1/2}$ and $\omega_0 = \omega_{pd} k/\left(k^2 + k_D^2\right)^{1/2}$, Momeni et al.[165] find,

$$\frac{d^2 n_d}{dt^2} - \left(\alpha - \beta n_d^2\right)\frac{dn_d}{dt} + \omega_0^2\left(1 + h\cos\gamma t\right) n_d = 0 \tag{4.8}$$

Finally, by defining dimensionless variables $\tilde{t} = \omega_0 t$, $x = n_d/n_{d0}$, $\tilde{\alpha} = \alpha/\omega_0$, $\tilde{\beta} = \beta n_{d0}^2/\omega_0$, and $\tilde{\gamma} = \gamma/\omega_0$, we have

$$\frac{d^2 x}{d\tilde{t}^2} - \left(\tilde{\alpha} - \tilde{\beta} x^2\right)\frac{dx}{d\tilde{t}} + \tilde{\omega}_0^2\left(1 + h\cos\tilde{\gamma}\tilde{t}\right) x = 0 \tag{4.9}$$

For simplicity, we drop the ˜ marks. We note that when $h \to 0$, we recover the Van der Pol equation[36, 186, 187], and when $\alpha = \beta = 0$, we recover the Matthieu equation. The total equation represents a nonlinear dynamical equation which is nonautonomous due to the $\cos \gamma t$ contribution.

Following Momeni et al. [165], we refer to Equation 4.9 as the Van der Pol-Matthieu (VdPM) equation and recast it as a set of coupled ordinary differential equations (ODEs) with the form

$$\begin{aligned} \frac{dx}{dt} &= y \\ \frac{dy}{dt} &= \left(\alpha - \beta x^2\right) y - \omega_0^2 \left(1 + h\cos(\gamma t)\right) x \end{aligned} \tag{4.10}$$

We take one more step to cast this as a three dimensional system, replacing γt by a variable θ so that,

$$\begin{aligned} \frac{dx}{dt} &= y \\ \frac{dy}{dt} &= \left(\alpha - \beta x^2\right) y - \omega_0^2 \left(1 + h\cos(\theta)\right) x && (4.11) \\ \frac{d\theta}{dt} &= \gamma && (4.12) \end{aligned}$$

For certain parameter values, this system can exhibit chaotic behavior [165]. We examine the application of our previous connecting curve method for this system in a more stable, well-behaved region.

4.1.3 Connecting Curves for a Nonautonomous System

We recall that our equation for the analytical form of the connecting curve was given as,

$$\gamma_i = \frac{d}{dt} f_i = \frac{\partial f_i}{\partial x_s}\frac{dx_s}{dt} = J_{is} f_s = \lambda f_i \qquad 1 \leq i, s \leq 3 \tag{4.13}$$

We immediately notice where this equation will fail for nonautonomous systems similar to that given in Equation 4.12: the inclusion of a transcendental function requires that $\lambda = 0$ is the only possible solution. For example, Equation 4.13, when written out for the VdPM equation with $\gamma = 1$ for simplicity, gives,

$$\begin{bmatrix} y \\ \left(\alpha - \beta\, x^2\right) y - \omega^2 \left(1 + h \cos\left(\gamma\, t\right)\right) x \\ 1 \end{bmatrix} = \tag{4.14}$$

$$\lambda \begin{bmatrix} \left(\alpha - \beta\, x^2\right) y - \omega^2 \left(1 + h \cos\left(\gamma\, t\right)\right) x \\ y \left(-2\,\beta\, xy - \omega^2 \left(1 + h \cos\left(\gamma\, t\right)\right)\right) + \left(\left(\alpha - \beta\, x^2\right) y - \omega^2 \left(1 + h \cos\left(\gamma\, t\right)\right) x\right) \left(\alpha - \beta\, x^2\right) + \omega^2 h \sin\left(\gamma\, t\right) \gamma\, x \\ 0 \end{bmatrix}$$

Thus the connecting curve condition simply becomes a search for points at which the in-plane acceleration vector has zero magnitude. We plot two instances in Figure 4.1, where in one instance

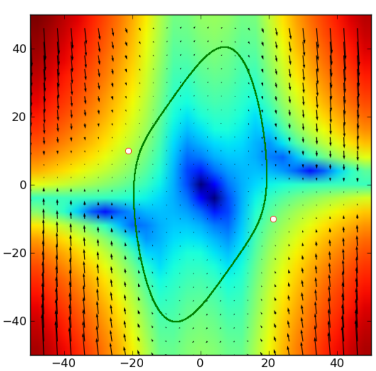

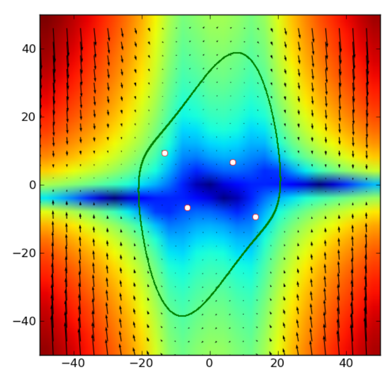

Figure 4.1: Vector field, cross section of VdPM attractor, and connecting curve plot for the VdPM for $\omega t = 0.14(2\pi)$ (left) and $\omega t = 0.325(2\pi)$ right. These figures represent cross-sectional slices through the resulting attractor parametrized by time. Variables are $\alpha = 1.0$, $\beta = 0.01$, $\omega = 1.0$, $h = 0.4$, and $\gamma = \pi/2$. Arrows represent the direction of the vector field, where their length corresponds to magnitude; colors represent relative magnitude of the vector field, where blue represents relatively weak vector fields and red represents strong vector fields. The white dots are where the connecting curve found using the method of Chapter Three intersects the cross-sectional slice. The green curve is the VdPM attractor. The attractor was calculated using GNU Scientific Library software, the vector field information was calculated using NumPY, and the connecting curves were calculated using Maple, with similar methods as in the previous chapter.

the resulting curves are found interior to the attractor, and in the other they are found outside the attractor, demonstrating the failure of this method to indicate the global shape of the dynamical system.

4.2 Standard Examples of Nonautonomous Curves

In order to demonstrate that the failure of the connecting curve to produce useful information for nonautonomous system is not limited to the VdPM system, we will show the results of its application to two other, more standard examples of nonautonomous systems.

4.2.1 Van der Pol Oscillator

The van der Pol (VdP) oscillator is a widely studied system [36] which results from driving the van der Pol dynamical equations with a driving term $A\sin(\omega t)$. The equations can be cast in the form,

$$\begin{aligned} \dot{x} &= by + \left(c - dy^2\right) x \\ \dot{y} &= -x + A\sin(\omega t) \end{aligned} \tag{4.15}$$

Using the same methodology as we used for the VdPM case, we find again that the connecting curve methodology fails to consistently provide useful information for the system. While in some cases the “curves” do indicate centers of rotation, they do not consistently do so (Figure 4.2).

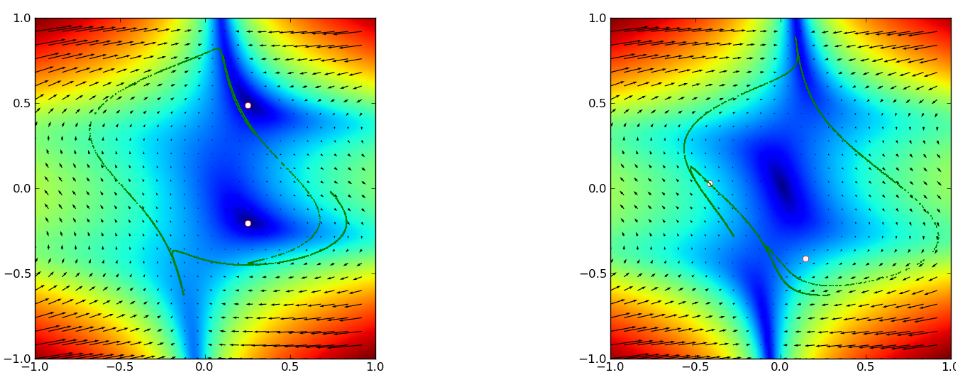

Figure 4.2: Modeling of Equation 4.15 with $A = 0.25$, $b = 0.7$, $c = 1.0$, $\omega = \pi/2$, and $d = 10.0$. These figures represent cross-sectional slices through the resulting attractor parametrized by time. In the left figure, $\omega t = \pi/2$, and in the right figure, $\omega t = \pi$. Arrows represent the direction of the vector field, where their length corresponds to magnitude; colors represent relative magnitude of the vector field, where blue represents relatively weak vector fields and red represents strong vector fields. The white dots are where the connecting curve intersects the cross-sectional slice. The green curve is the intersection of the VdP attractor with a plane. The attractor was calculated using GNU Scientific Library software, the vector field information was calculated using NumPY, and the connecting curves were calculated using Maple, with similar methods as in the previous chapter.

4.2.2 Duffing Oscillator

Another common nonautonomous system is the Duffing Oscillator, which can be cast in the following equations [36],

$$\begin{aligned}\dot{x} &= y \\ \dot{y} &= -\delta y - x^3 + x + A\sin(\omega t)\end{aligned} \tag{4.16}$$

In the case of the Duffing Oscillator, the connecting curves we find tend to be somewhat more useful than in the previous two examples, as the curves tend to indicate the direction which the Duffing attractor drifts as it evolves with ωt. However, again we find that the information provided by the

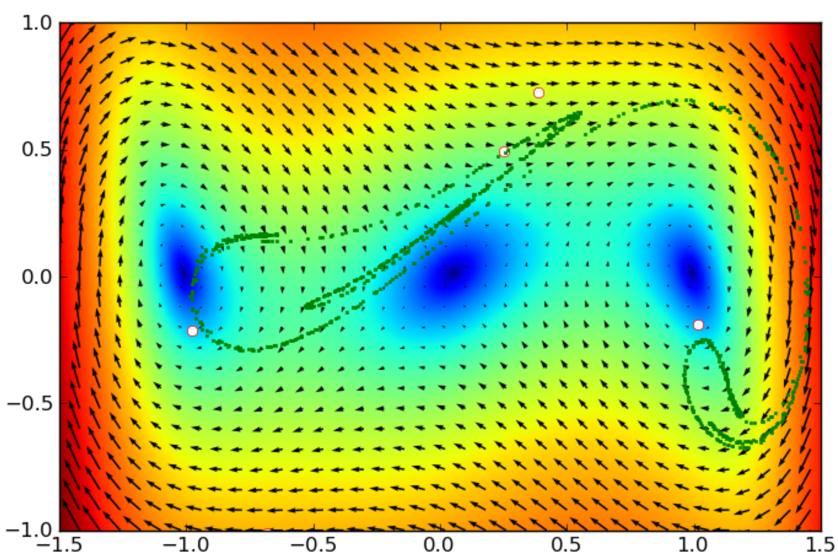

Figure 4.3: Modeling of Equation 4.16 with $\delta = 0.4$, $A = 0.4$, and $\omega = 1.0$. In the above figure, $\omega t = \pi$. The figure represents a cross-sectional slices through the resulting attractor parametrized by time. Arrows represent the direction of the vector field, where their length corresponds to magnitude; colors represent relative magnitude of the vector field, where blue represents relatively weak vector fields and red represents strong vector fields. The white dots are where the connecting curve intersects the cross-sectional slice. The green curve is the Duffing forced system attractor. The attractor was calculated using GNU Scientific Library software, the vector field information was calculated using NumPY, and the connecting curves were calculated using Maple, with similar methods as in the previous chapter.

connecting curves doesn't give the sort of spinal structure that we found in the autonomous cases. We turn next to an alternative method for finding an analogue for connecting curves for autonomous systems that might provide more interesting information.

4.3 Variational Approach to Nonautonomous Connecting Curves

It is clear that no method based on parallel vectors will provide an adequate connecting curve for systems which incorporate transcendental functions. We thus turn to an alternative method and use variational methods in an attempt to find a more descriptive connecting curve. It is not uncommon in physics to turn to variational principles when other methods fail to provide a satisfactory answer.

We begin by assuming that the skeletal curve we seek for nonautonomous systems can be approximated by a truncated Fourier series of the form,

$$\begin{aligned} F(x,t) &= x_0 + \sum_{m=1}^{p} \left(c_{x,m}\cos(mt) + s_{x,m}\sin(mt)\right) \\ F(y,t) &= y_0 + \sum_{m=1}^{p} \left(c_{y,m}\cos(mt) + s_{y,m}\sin(mt)\right) \end{aligned} \tag{4.17}$$

We will assume that the velocity associated with the ith coordinate is $\dot{R}_i \pm f_i(R)$ in which we are counting both the velocity associated with the velocity field at that point, and the velocity of a test particle tracing out this curve, so that the energy equation we wish to minimize along the eye curve trajectory is

$$\mathfrak{E} = \frac{1}{2}\sum_i \left(\dot{R}_i \pm f_i(\mathbf{R})\right)^2 \tag{4.18}$$

Our task is then to minimize this energy function. Physically, this is essentially equivalent to the minimal pressure method for vortex core searches (see Chapter 2), where we assume that some linear combination of the velocity field at the center of the vortex curve and the rate of change in the shape of the vortex curve itself are minimized.

Applying the Euler-Lagrange equations to Equation 4.18 yeilds,

$$
\begin{aligned}
\frac{\partial \mathfrak{E}}{\partial R_j} &= \frac{d}{dt}\frac{\partial \mathfrak{E}}{\partial \dot{R}_j} && (4.19)\\
\frac{\partial \mathfrak{E}}{\partial R_j} &= \sum_i \left(\frac{\partial f_i(\mathbf{R})}{\partial R_j}\left[\pm \dot{R}_i + f_i(\mathbf{R})\right]\right) && (4.20)\\
\frac{d}{dt}\frac{\partial \mathfrak{E}}{\partial \dot{R}_j} &= \frac{d}{dt}\sum_i \left(\dot{R}_i \pm f_i(\mathbf{R})\right) && (4.21)\\
\sum_i \left(\frac{\partial f_i(\mathbf{R})}{\partial R_j}\left[\pm \dot{R}_i + f_i(\mathbf{R})\right]\right) &= \ddot{\mathbf{R}} \pm \mathbf{J} f(\mathbf{R}) && (4.22)
\end{aligned}
$$

This equation doesn't entail the sort of eigenvalue-like solutions we were able to find for autonomous strange attractors in the previous chapter, so we proceed instead to use a numerical technique to minimize the energy functions. A simplified example follows to outline the method.

4.3.1 A Truncated Example

The Duffing Oscillator (Equation 4.16) is considered in the remainder of this chapter as it represents the attractor with the most interesting shape in terms of locating vortex tubes.

We set $A = 0.4$, $\delta = 0.4$, and $\omega = 1$. Using an extremely abbreviated Fourier series for the x and y coordinates of our vortex core, we have,

$$
\begin{aligned}
F_x(t) &= \alpha_x + \beta_x \cos(t) + \gamma_x \sin(t) && (4.23)\\
F_y(t) &= \alpha_y + \beta_y \cos(t) + \gamma_y \sin(t) && (4.24)
\end{aligned}
$$

We make a simplifying assumption (which is not necessary, but will make calculations simpler) that $F(y,t) = \frac{dF(x,t)}{dt}$, (and we drop the x, y subscripts on the coefficients), so that the energy equation (Equation 4.18) simplifies to,

$$
E(t) = \begin{cases} \int_0^{2\pi} \left(\frac{dF_x(t)}{dt} - F_y(t)\right)^2 dt = 0 \\ \int_0^{2\pi} \left(\left[\frac{d^2F_x(t)}{dt^2}\right] - \left[-\delta\frac{dF_x(t)}{dt} - F_x^3(t) + F_x(t) + A\sin(\omega t)\right]\right)^2 dt \end{cases} \quad (4.25)
$$

Using Maple, we plot this energy function in Figure 4.4. Next we construct the functions

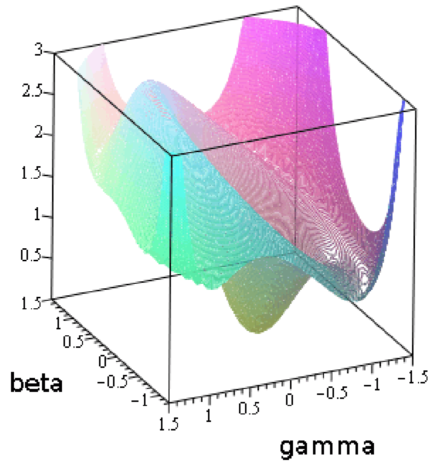

Figure 4.4: The energy function of Equation 4.25 as a function of β and γ with $\alpha = 0$.

$$\Delta\alpha = \frac{dE(t)}{d\alpha} \tag{4.26}$$

$$\Delta\beta = \frac{dE(t)}{d\beta} \tag{4.27}$$

$$\Delta\gamma = \frac{dE(t)}{d\gamma} \tag{4.28}$$

Using the method of steepest descent, we minimize the energy function. We begin with initial guesses (to be detailed in the next section) and iterate each of these guesses through a loop such that,

$$\alpha_{i+1} = \alpha_i - \epsilon\Delta\alpha \tag{4.29}$$

$$\beta_{i+1} = \beta_i - \epsilon\Delta\beta \tag{4.30}$$

$$\gamma_{i+1} = \gamma_i - \epsilon\Delta\gamma \tag{4.31}$$

where ϵ is a step factor we set equal to $0.005/\sqrt{(\Delta\alpha)^2 + (\Delta\beta)^2 + (\Delta\gamma)^2}$. We repeat this iteration until the change in coefficients becomes negligible, as we have reached a minima.

This minimal value identifies the coefficients used to compose the proposed vortex curve. Of course, a more accurate result will require that we truncate our Fourier series at higher coefficients, and in this case, the energy landscape will be higher-dimensional. While this makes visualization of such a landscape impossible, we can still safely use the numerical techniques of steepest-descent.

4.4 Minimization Technique Applied to Duffing Driven Oscillator

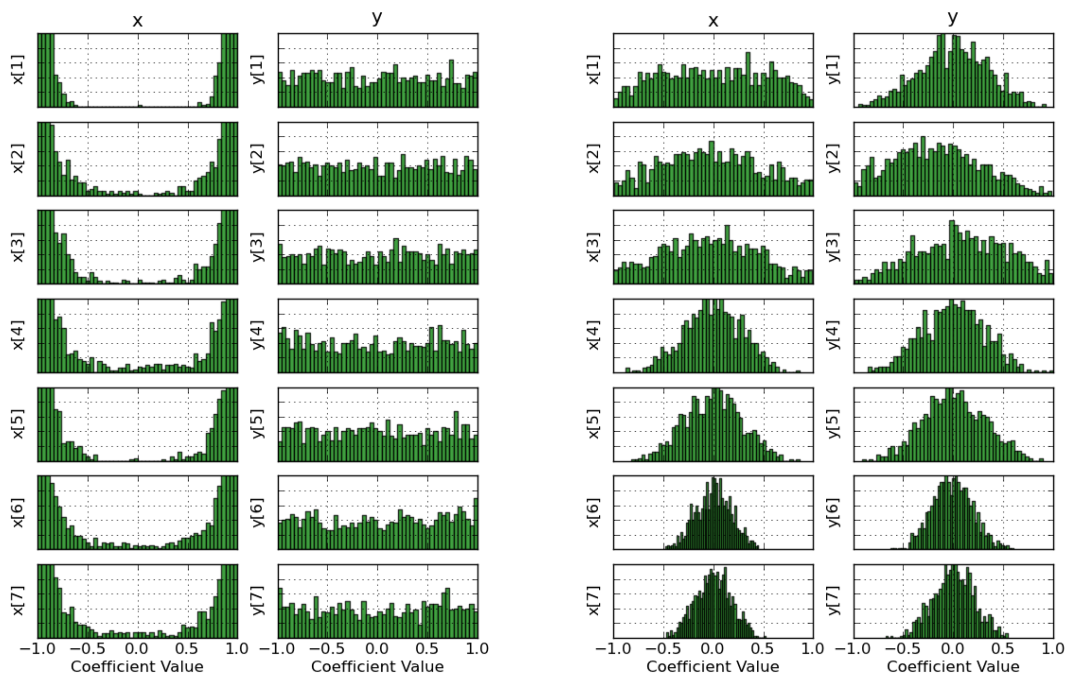

Figure 4.5: Statistical analysis of the curve functions for the Duffing system. From a sample size of 10,000,000 cases where all coefficents were randomly and independently chosen with values between -1.0 and 1.0. From this ensemble we selected the cases with the highest and lowest energy to compare and contrast their statistical profiles. Left: A histogram plot of the 1,000 cases with the highest energy indicates a very strong bias for the coefficients of F_x towards ± 1, with no such bias for F_y. Right: A histogram plot of the 1,000 cases with the lowest energy indicates an initial starting guess of zero for coefficients greater than three is reasonable. The coefficients $y[2]$ and $y[3]$ show assymetrical biases.

For our analysis, we truncate our fourier series at $p = 3$ such that the coefficents of our substitute connecting curve will be

$$
\begin{aligned}
R_x(t) &= x[1] + x[2]\cos(t) + x[3]\sin(t) + x[4]\cos(2t) + x[5]\sin(2t) + x[6]\cos(3t) + x[7]\sin(3t) \\
R_y(t) &= y[1] + y[2]\cos(t) + y[3]\sin(t) + y[4]\cos(2t) + y[5]\sin(2t) + y[6]\cos(3t) + y[7]\sin(3t)
\end{aligned}
\tag{4.32}
$$

We start by conducting a statistical analysis of the energy (Equation 4.18) for a randomly selected set of coefficients of Equation 4.32. From a sample size of 10,000,000 cases where all coefficents were randomly and independently chosen with values between −1.0 and 1.0, we calculate the corresponding energy. We sort the output by energy and select the 1,000 with the highest energy, and the 1,000 with the lowest energy. A histogram of these coefficients are shown in Figure 4.5. What is most noticeable from these results is that we can make a fair first approximation for this curve by setting $x[p], y[p] = 0$ for $p > 3$ since these coefficients are concentrated near zero in the histogram for the lowest energy values. We also make the ansatz that we can set the first coefficient to zero in our initial guess, since it isn't multiplied by a cosine or sine function. This is necessary to reduce the number of free parameters to just four, making it possible to analytically find the minimum for a curve approximated by the form,

$$\begin{aligned} R_x(t) &= x[2]\cos(t) + x[3]\sin(t) \\ R_y(t) &= y[2]\cos(t) + y[3]\sin(t) \end{aligned} \tag{4.33}$$

we do this for both cases in Equation 4.18 of ±. Using the widely used algebraic software Maple, and the simplified equation for the curve (Equation 4.33), we can solve for coefficients which give us zero energy as follows:

```
restart; a := .4; Δ := .4;
xxx := x[1]*cos(t)+x[2]*sin(t);
yyy := y[1]*cos(t)+y[2]*sin(t);
g1 := diff(xxx, t)+yyy;
g2 := diff(yyy, t)-Δ*yyy-xxx^3+xxx+a*sin(t);
energy := int(g1*g1+g2*g2, t = 0 .. 2*Pi);
dx1 := diff(energy, x[1]);
dx2 := diff(energy, x[2]);
dy1 := diff(energy, y[1]);
dy2 := diff(energy, y[2]);
solns := {RealDomain:-solve({dx1, dx2, dy1, dy2}, {x[1], x[2], y[1], y[2]})};
```

In both cases, this gave us three sets of solutions. Our next task was to numerically take these solutions as initial guesses in a minimization method of steepest-descent applied to all fourteen coefficients of Equation 4.32, where all coefficients are set to zero accept the solutions found in the previous step. Upon convergence, we found three sets of curves for both the $+$ and $-$ case of Equation 4.18. It is customary to visualize driven attractors, parametrized by t from $0 \to 2\pi$, by a homotopy $t \to S^1$. This does not affect the dynamics.

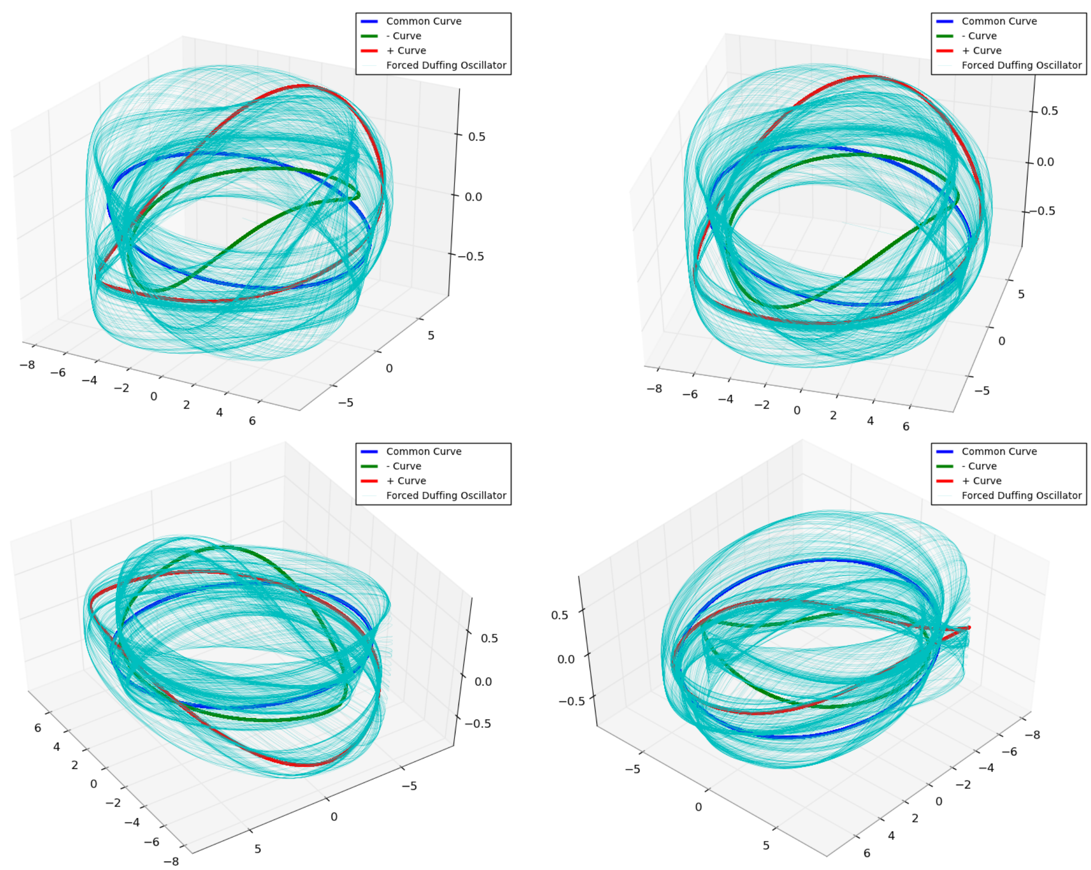

Figure 4.6: Vortex curves found for Duffing nonautonomous system (Equation 4.16) using energy minimization technique, plotted with attractor. Four different angles are shown of the same attractor and curves to show how these curves successfully highlight some of the major features of the attractor. Electronic version shows color. The common curve is a curve which both the $+$ and the $-$ cases found as a minima curve.

4.5 Conclusion

Because periodically driven dynamical systems introduce a transcendental function in the form of a sine or a cosine, the connecting curve algorithms we use for autonomous systems fails to provide useful information about the system. We have shown that a class of methods for detecting vortex curves fails to provide interesting results for such systems, and a new method must be found. We have introduced such a new method, using a variational approach, and find that we can calculate a set of curves for nonautonomous systems which exhibit some of the usefulness of the connecting curves in outlining the structure of the strange attractor. This method is numerical and numerically intensive. Due to the nature of nonautonomous strange attractors, these vortex curves lack some of the more interesting features seen in the connecting curves for autonomous systems. Despite these reservations, this research represents the first known algorithm for finding approximate vortex curves for nonautonomous systems.

Chapter 5: Bimodal Maps of the Interval and Codimensional-2 Parameter Space

We now turn our focus back towards the dynamics of mappings introduced in Chapter One. While this may seem like a sudden break from our previous discussion of strange attractors, we will see in the next chapter that the concept of mappings becomes very important in understanding some very important global features of strange attractors. Whereas in the last few chapters we focused on the shape of strange attractors as a new source of information about their global structure, we treated the parameters of these systems as fixed numbers. Many interesting questions arise when we we consider the global behavior of strange attractors in the context of parameter space.

A fortunate accident of nature is that the most common type of three-dimensional strange attractors found in nature are Smale-like highly dissipative systems. As a result of this, these systems can be studied with help from the tools of the dynamics of mappings. For our purposes, we can restrict ourselves to the dynamics of unimodal and bimodal mappings, and a brief introduction to the latter follows.

5.1 An Example of a Bimodal Map

We first consider as example the mapping $T_\lambda(x_{n+1}) = x_n^3 - \lambda x_n$. As we can see in Figure 5.1, this map is characterized by having three distinct sections. When $\lambda > 0$, these sections are partitioned by two critical points ($dT_\lambda/dx = 0$). As we shall see, this map allows for more complicated dynamics than does the unimodal map. We first take a brief tour of some of the dynamical features of a simple bimodal map.

When $-1 < \lambda \leq 1$ we have fixed points ($T_\lambda(x_{n+1}) = x_n$) at $0, \pm\sqrt{1+\lambda}$. It becomes immediately obvious that this fixed point regime breaks down when $\lambda < -1$, i.e. it takes upon imaginary values.

We also explore the behavior of the derivative of $T_\lambda(x) = x^3 - \lambda x$, i.e. $T'_\lambda(x) = 3x^2 - \lambda$. We now examine the three fixed points for values of λ in the interval $J = (-1, 1]$.

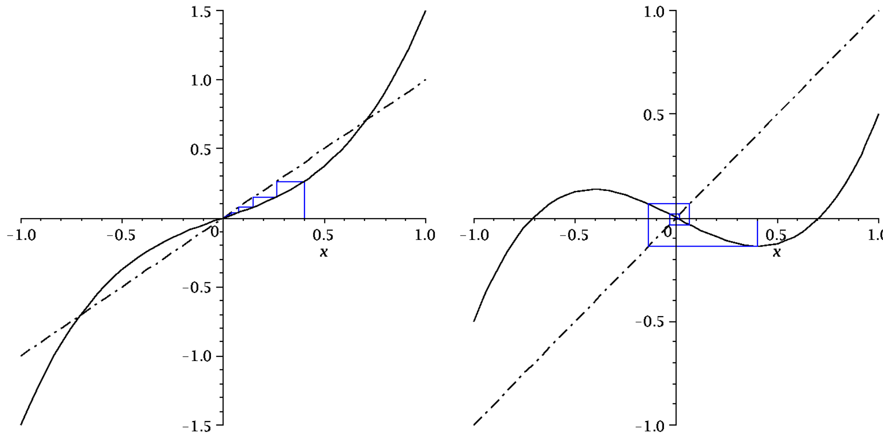

Figure 5.1: $T_\lambda = x^3 - \lambda x$ with $\lambda = -0.5$ (left) and 0.5 (right). In both cases, the map has three fixed points (not shown fully on right).

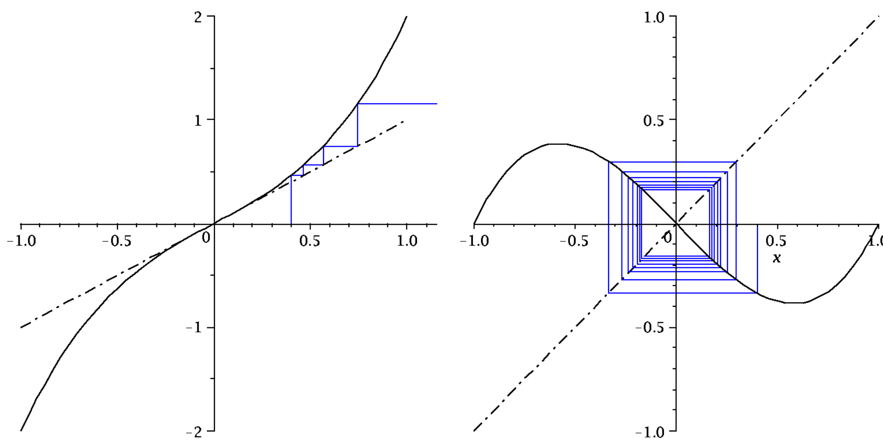

Figure 5.2: $T_\lambda = x^3 - \lambda x$, with $\lambda = -1$ (left) and and $\lambda = 1$ (right).

1. The fixed point $x = 0$ yields $\|T'_\lambda(x)\| = \|\lambda\| < 1$ on J. It is hyperbolic and contracting in the interval J. It is repulsive on $\mathbb{R}/J$.

2. The fixed points $\pm\sqrt{1+\lambda}$ give $\|T'_\lambda(x)\| = \|3(1+\lambda) - \lambda\| = \|2\lambda + 3\|$. At $\lambda = -1$, the fixed point is triply-degenerate.

We also note, as in the figures above, that T_λ crosses the $y = -x$ line for $\lambda > 1$; this clearly would not happen for $\lambda < 1$, and it becomes even more obvious that the cases $\lambda \leq 1$ and $\lambda > 1$ are dynamically dissimilar. The result of the crossing of the $y = -x$ line is that we get a period 2 orbit (since $T_\lambda(x) = -x$ and $T_\lambda(-x) = -T_\lambda(x)$).

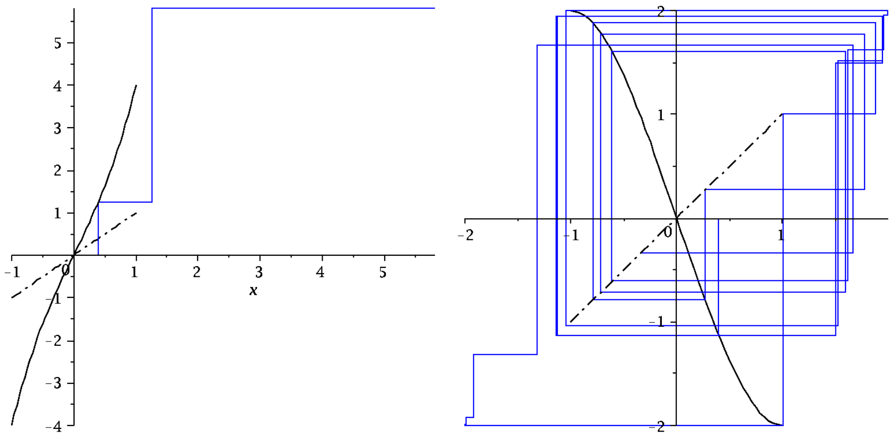

Figure 5.3: $T_\lambda = x^3 - \lambda x$ with $\lambda = -3$ (left) and $\lambda = 3$ (right). When $\lambda > 1$ we enter a regime of chaotic behavior.

Symbolic Dynamics

The symbolic dynamics of bimodal maps involves the use of three symbols. For the remainder of this thesis we will be using the convention shown in Figure 5.4. In this case, we have two critical points, which we label C for the rightmost critical point, and D for the leftmost critical point. The "laps" of the map are labeled as 0 for the segment right of C, 1 for the segment between C and D, and 2 for the segment left of D.

Normal Forms of Bimodal maps

A normal form is an equation that describes a particular class of objects, in our case it will be bimodal maps, such that all maps in this class are conjugate to the normal form, and the normal form typically represents the simplest way of expressing the dynamical equations for the system. In 1988, Branner and Hubbard [188] showed that all bimodal maps are conjugate to the form[1]

$$x \mapsto \sigma x^3 + 3ax - b \tag{5.1}$$

where $\sigma = \pm 1$. Figure 5.6 shows the periodicity bifurcation diagram for the case for $\sigma = -1$.

[1] Their result was more generic and applied to the complex plane, here we use only the real-valued variation [189].

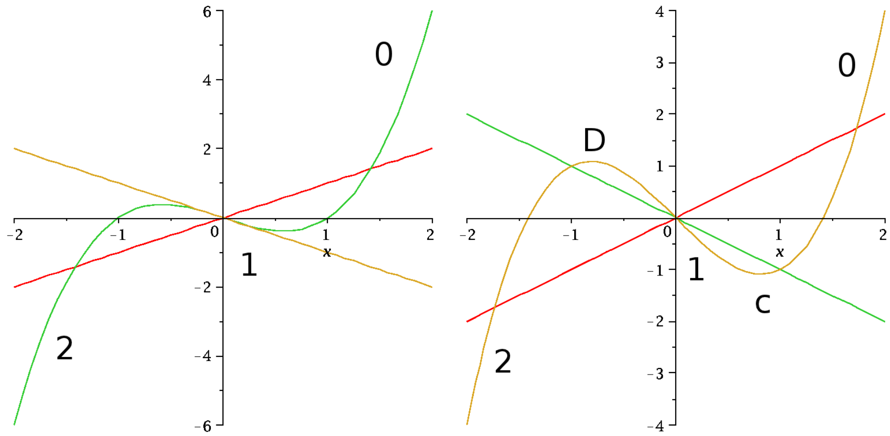

Figure 5.4: $T_\lambda = x^3 - \lambda x$ with $\lambda = 1$ (left) and $\lambda = 2$ (right) with $y = x$ and $y = -x$ superimposed. We have labeled these maps with the symbols we will be using to describe bimodal systems, where the rightmost critical point is labeled as C and the leftmost critical point is labeled D. Positions to the right of C are labeled 0, positions between D and C are labeled 1 and positions left of D are labeled 2.

5.1.1 Shrimp Shapes and Orientations

The shrimp features are a signature of bimodal mappings. With the use of Kneading Theory [31], it has been shown that the locus of superstable parameters–parameters which correspond to orbits which include at least one critical point–in codimensional-2 space (the space of the control parameters a, b) is a continuous curve with a parabolic shape [190, 191]. At the head of this parabolic shape, the symbolic sequence of a superstable orbit undergoes a transition as one point on the return map passes through a critical point (but not the critical point which the orbit shares in common at all points along the curve, see Figure 5.5). On one side of the parabola, this point is on the left side of this critical point, and on the other side, it is on the right side. At this point of the parabolic curve, where both sides meet, the orbit is an iteration of two critical points.

On each parabola, one point on the orbit will always be fixed on one of the critical points, say the rightmost one, and at the head of the shrimp, one point inhabits the leftmost critical point as well. What happens then if we hold the point inhabiting the leftmost critical point fixed and allow the point on the orbit inhabiting the rightmost critical point to vary to the left and right side of the critical point? We will thus have a new parabolic curve which turns out to have a differing orientation. The intersection of these parabolas of superstability are what give the shrimp their

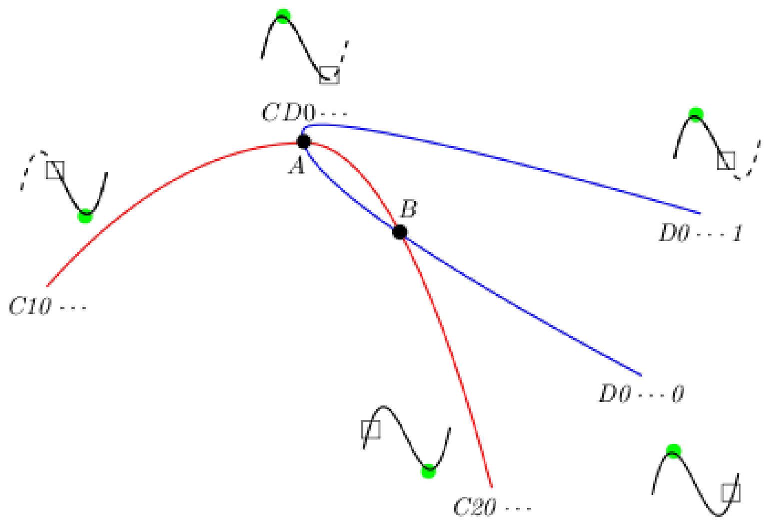

Figure 5.5: Generic model for a shrimp in bimodal parameter space. Each of the intersecting parabolas corresponds to one of the critical points being held fixed. At the intersecting heads of these parabolas, A, we have a doubly-superstable orbit which includes both critical points. The intersection B is not due to doubly-superstable orbits, but rather two coexisting stable orbits, one for each critical point. These orbits have different basins of attraction, which means that an integration of the system will only manifest one or the other orbit, depending on the initial conditions selected

characteristic shape.

Let us consider what happens when we have control parameters which lie at the head of the shrimp (position A in Figure 5.5). It is not generally the case that one control parameter will correspond to varying a stable periodic orbit around one critical point, and another control parameter will vary the stable periodic orbit around the other fixed point. In general, both control parameters will affect either point. However, each system has a specific orientation to which the shrimp line up. For example, in Figure 5.7 we see that the shrimp on the left branch of the chaotic region for the normal form have an approximately $\pi/4$ radian orientation with respect to the parameter axes. To find ourselves on the rightmost parabola for this shrimp, we need vary our parameters in the positive a, positive b direction; the other parabola would require a positive a, negative b direction. To follow each leg of one of the parabolas, we will require a different angle in the same general direction.

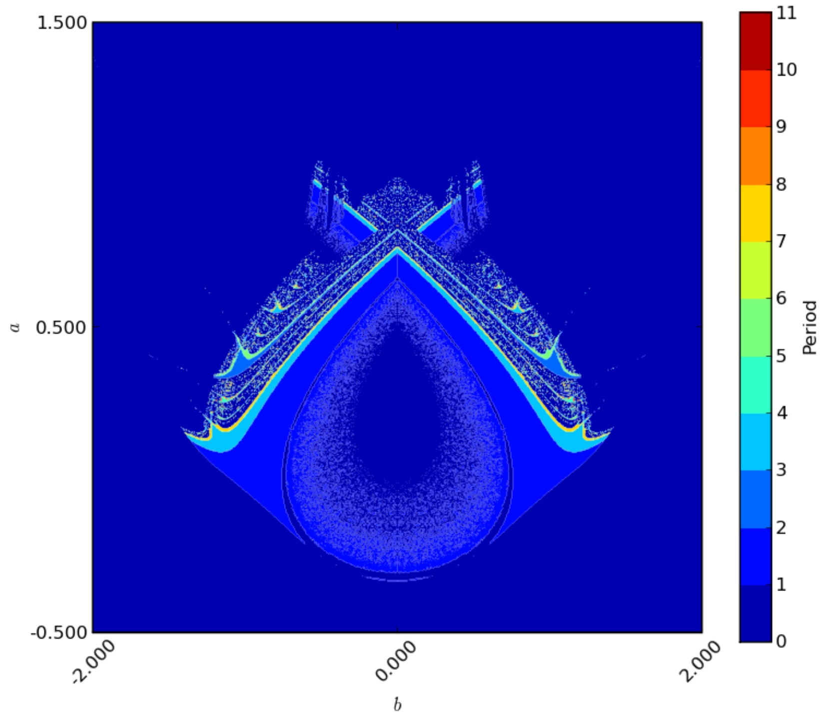

Figure 5.6: Periodicity diagram for the codimensional control-parameter space of Equation 5.1 with $\sigma = -1$.

Location of Shrimp Heads for the Bimodal Normal Form

One of the functions of normal forms (also called canonical forms) is to capture the essence of a dynamical system with the simplest equations possible, and it turns out that one can locate the center of shrimp for Equation 5.1 fairly easily [190, 192]. The derivative of a point on an orbit indicates its stability (which is why critical points, whose derivative is zero, are superstable). The multiplier of a period p orbit is defined as the multiplication of the derivatives of all the points of the orbit. Let $f(x) = -x^3 + 3ax - b$, then an orbit with a sequence $\{x_1, x_2, x_3, \cdots, x_p\}$ will have a multiplier,

$$m_p = \prod_{i=1}^{p} f'(x_i) \tag{5.2}$$

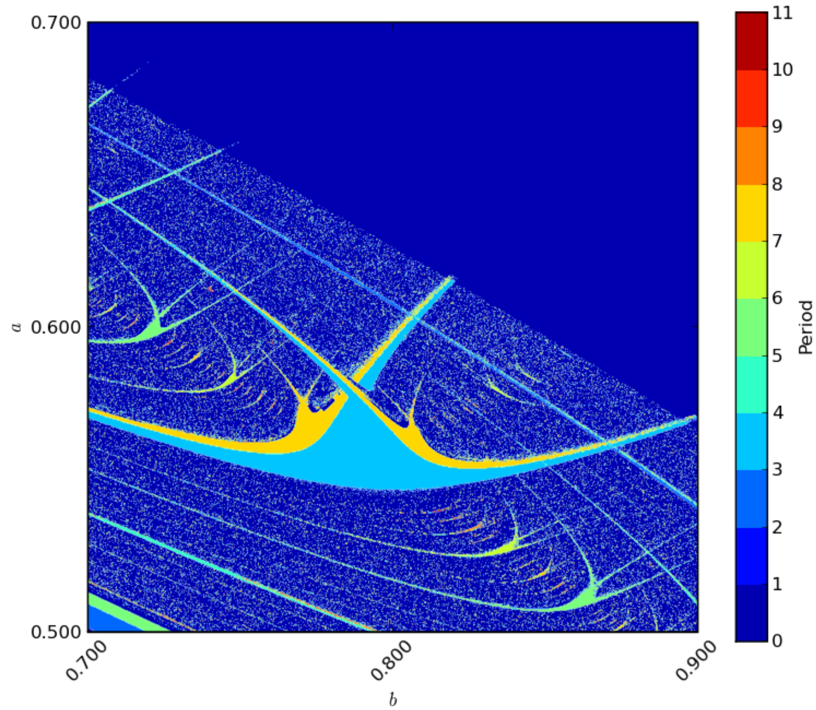

Figure 5.7: Periodicity diagram for the codimensional control-parameter space of Equation 5.1 with $\sigma = -1$, focusing in on a period-4 shrimp.

where $f'(x_i) = -3x_i^2 + 3a$. In terms of this multiplier, we can define superstable orbits by the condition that for some i, $x_i^2 = a$, which has a solution $x_i = \pm\sqrt{a}$. Where we have a multiplier in which two terms are zero (of course, for bimodal maps, no more than two terms can be zero), we will have located the center of a shrimp. The sequence of points for such an orbit will have the form $\{\pm\sqrt{a}, \mp\sqrt{a}, x_3, x_4, x_5, \cdots, x_p\}$. This sets up a series of constraint equations, which constrain

b based on the requirement that,

$$\begin{aligned} f(\sqrt{a})) &= -\sqrt{a} \\ f(f(\sqrt{a})) &= x_3 \\ f^3(\sqrt{a})) &= x_4 \\ &\vdots \\ f^{p+1}(\sqrt{a})) &= \sqrt{a} \end{aligned} \tag{5.3}$$

For example, it can be shown [190] that for period-3, these conditions give the equation $32a^4 + 24a^3 - 2a - 1 = 0$. This being a fourth-order polynomial root, an exact solution can be found [193]. For periods higher than period-3, we will require numerical means to locate the corresponding shrimp heads. Taking the real solutions, one period-3 shrimp head for the bimodal normal form can be located at $(a, b) \approx (0.36453, 1.04422)$. By reversing the order of the sequence, one obtains the location of a second shrimp head at $(a, b) \approx (0.36453, -1.04422)$.

In this way, we can identify the number and location of shrimp in the codimensional-2 parameter space of the bimodal normal form. This method will grow increasingly problematic for higher period due to the increasing complexity of solutions.

5.2 Conclusion

We have briefly discussed the remarkable features found in bimodal maps, the so-called shrimp structures seen in biparameter phase space. These features are fascinating unto themselves, but what is even more fascinating is that they tend to show up in surprising places. When one plots the global Lyapunov exponents (Chapter One) of the Rössler system's biparameter space, one finds that this space is swarming with shrimp. Why is this the case, and can we find a systematic way to describe the organization of these swarms of shrimp?

Chapter 6: Periodicity spiral hubs in the biparameter Lyapunov space of the Rössler attractor

> *We observed hubs and spirals in a broad spectrum of oscillators such as the Rössler equations, in variations of Chua's circuit, in certain chemical and biological oscillators and, therefore, expect them to be of importance in several fields, beyond the electronic circuit used as an illustrative example here. A key open question now is to investigate what sort of dynamical phenomena lead to hubs and spirals, the eventual role of homoclinic orbits in their genesis, and the mechanisms inducing periodicity transitions along and among spirals.* –Bonatto & Gallas [194]

Recently, an increased attention has been focused on the appearance of nested spirals, called hubs, and so called "shrimp" or "swallows" within the biparameter space of a number of dissipative systems [93, 194–200] (Figure 6.1). While these swallows have been known to exist in systems such as the Hénon map [201], the Rössler system [192], and the normal form of the cubic map [189], their placement relative to a spiral hub, and the form of the spiral hubs themselves, has not been explained in any depth thus far.

Furthermore, while in some systems, these hubs have been shown to coincide with homoclinic bifurcations under Shilnikov conditions[1] [198–200], other examples have been claimed to exist in which these hubs occur under non-Shilnikov conditions or do not occur under Shilnikov conditions [194, 197]. This remains an open question, as the latter claims are not fully convincing and require further investigation. Ultimately for our purposes, we only require that the center of these hubs have homoclinic-like behavior and so we do not address the Shilnikov conditions question further.

In this chapter, we elucidate the dynamical mechanism responsible for the creation of these spiral hubs, showing that they have a topological signature that can be found in dissipative systems whose low-parameter return map has a unimodal nature which transitions to a cubic nature. We show

[1] Shilnikov conditions on a saddle-focus fixed point undergoing a homoclinic bifurcation entail the existence of countably many saddle periodic orbits near that fixed point. Since the appearance of hubs only seems to require a homoclinic point, whether or not it has Shilnikov conditions, we do not consider this condition further.

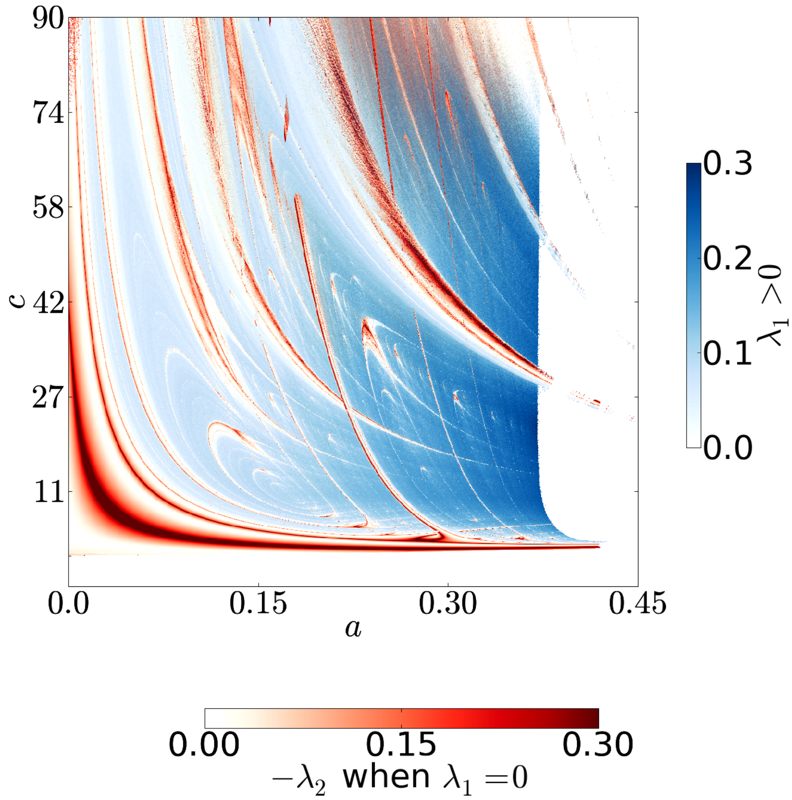

Figure 6.1: Lyapunov phase diagrams for the Rössler system. (Color online). Blue coloration reflects the intensity of the first Lyapunov exponent, red coloring reflects that of the negative of the second exponent when $\lambda_1 = 0$. Blue regions correspond to chaotic behaviors, red regions correspond to regions of superstability. White regions correspond to transitional regions or regions where the attractor has undergone a boundary crises. Lyapunov exponents were calculated in a 1000x1000 grid using the LESNLS software package [107].

- The partial topological conjugacy[2] of the Rössler system for with the Logistic Map, whenever its return map is unimodal, constrains its dynamical behavior in the codimension-2 parameter plane which leads to the round hub shape seen on the branch-2 side of the parameter plane (Figure 6.2).

- Exactly how the periodicity shifts along the spiral trail, pointing out, for the first time, the region of transition of the period as we follow the spiral inwards. We show the mechanism for

[2] As a referee has pointed out, "the Rössler system is not [fully] conjugate to a logistic map because there are infinitely many bifurcations whose order of occurrence is reversed as soon as the Poincaré section is 2D vs. 1D (admittedly for orbits of high period), see [202]". As will be made clear shortly, we are nowhere claiming complete conjugacy of all periodic orbits. In fact, we limit ourselves to orbits up to period seven for which we have numerically demonstrated conjugacy both in the return map and in the order of periods. We need not consider the extremely high periods at which this conjugacy breaks down to understand the primary features of the spiral hubs.

this transition and, using symbolic dynamics, we accurately predict the exact symbol sequence of the period shift.

- Continuity of super-stable orbits at the intersection of the topological division in the codimension-2 parameter plane, where on one side the Rössler system is described by a two-branch manifold, and on the other side it is described by a three-branch manifold, results in a shrimp pattern along this boundary in which the ordering of the periodicity of the shrimp is the same as that of the superstable periodic orbits of the Logistic Map.

- There exist striation patterns in the codimension-2 plane which are faint but appear as a new open question. These striations have appeared in figures published in the literature previously, but apparently haven't yet been pointed out.

6.1 A Hub in the Rössler System

The occurrence of these spiral hubs is easily seen in Lyapunov phase diagrams for the Rössler system (Figure 6.1). In keeping with recent work, we focus on a hub found in the Rössler system. The hubs for this system have been studied for a number of different parameter values [93]. Here, we concentrate on the $b = 0.2$ regime, although our findings are valid for all regimes in which chaos will be found.

The equations for the Rössler system [42] are,

$$\overrightarrow{V}\begin{pmatrix} \dot{x} \\ \dot{y} \\ \dot{z} \end{pmatrix} = \overrightarrow{\Im}\begin{pmatrix} f_1(x,y,z) \\ f_2(x,y,z) \\ f_3(x,y,z) \end{pmatrix} = \begin{matrix} -y-z \\ x+ay \\ b+z(x-c) \end{matrix} \tag{6.1}$$

For this study, we hold the parameter value b constant at 0.2 such that our bi-parameter space is in the a, c parameter plane. We color the magnitude of the first two nonzero Lyapunov exponents (the third is always negative, and at any time, one of the three is always zero), where, for example, in Figure 6.1, red implies a higher magnitude for the second Lyapunov exponent when the first is zero, where the darkest red indicates the presence of a superstable orbit, and blue indicates the intensity of the first Lyupunov exponent when the second is zero, which effectively measures how chaotic the system is.

We see a number of interesting features in a Lyapunov phase diagram of this plane (Figure 6.1), including areas of seeming discontinuity (coexisting basins of attraction in which our initial conditions have moved from one basin to another, see Gallas 1995 for a mathematically oriented discussion on such points [203]), spiral hubs (the clearest, seen in Figure 6.2, being centered at $(a, c) = (0.1798, 10.3084)$ which we will identify as the "primary hub"), and the so-called shrimp structures. In the region where the Rössler attractor is in its topologically simplest state ("spiral"), which is the region in which a return map will yield two branches, the hub structure is clearly organized in a spiral pattern.

Figure 6.2 shows this region in detail, and shows an approximate best-fit curve linking the centers of the shrimp structures along a line which corresponds to a transition from "spiral" (the return-map of the Rössler flow has two branches) to "screw-like" structure in the Rössler attractor, which corresponds to the branched-manifold describing the Rössler attractor obtaining a third branch and the return-map appearing bimodal, with two critical points (see Figure 6.3). This line was previously noted and estimated [198], and our best fit curve is approximated as

$$c \approx 1881a^2 - 856a + 103 \tag{6.2}$$

in agreement with previous estimates. Also in agreement with previous estimates[198], we find the center of the primary spiral hub to be numerically located at approximately $(a, c) = (0.1798, 10.3084)$. We label this curve the Topological Transition Line (from requiring two symbols to requiring three symbols) and denote it henceforth as TTL_3^2.

6.1.1 Second method for detecting spiral hubs

The algorithms which detect global Lyapunov exponents can be replaced with a quicker, simpler algorithm that successfully detects the spiral hubs. With this method, we construct a return map of the Rössler attractor and partition the map into five hundred equal divisions. We do this for

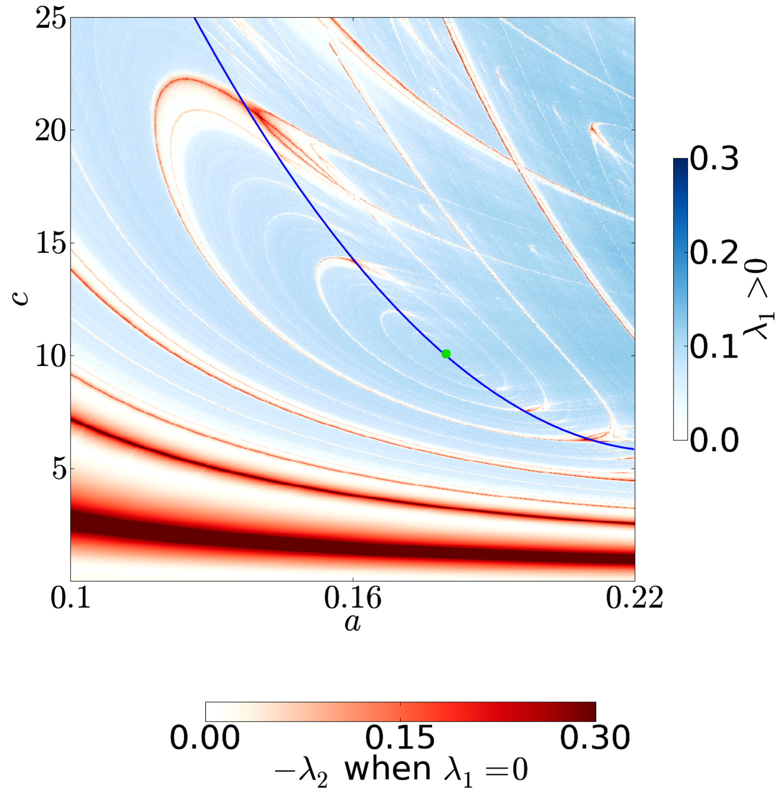

Figure 6.2: Lyapunov phase diagrams for the Rössler system, close up of primary spiral hub. Green center dot (color online) indicates the center of the spiral hub. Dark blue line indicates a best-fit curve for the partition of the primary hub by the appearance of "shrimp", a curve found previously [], which we call TTL_3^2 for Topological Transition Line (from unimodal, with two symbols, to bimodal, with three symbols). Blue coloration reflects the intensity of the first Lyapunov exponent, red coloring reflects that of the negative of the second exponent when $\lambda_1 = 0$. Blue regions correspond to chaotic behaviors, red regions correspond to regions of stability. White regions correspond to transitional regions or regions where the attractor has undergone a boundary crises. Lyapunov exponents were calculated on a 1000x1000 grid using the LESNLS software package [107].

5000x5000 data points on the $a-c$ parameter plane of the Rössler attractor, for a total of 25,000,000 integrations. We then plot the percentage of partitions of the map which are occupied by at least one point in an orbit. While super-stable periodic orbits, that is, orbits which are iterations of a critical point of the return-map, will only occupy a small number of divisions, typically the number equal to their period, chaotic orbits will spread out and occupy many divisions. Thus this method indicates, to great accuracy, which regions in codimension-2 parameter phase space are chaotic. This method does give false positives in the very small regions in which an orbit is undergoing a period-doubling

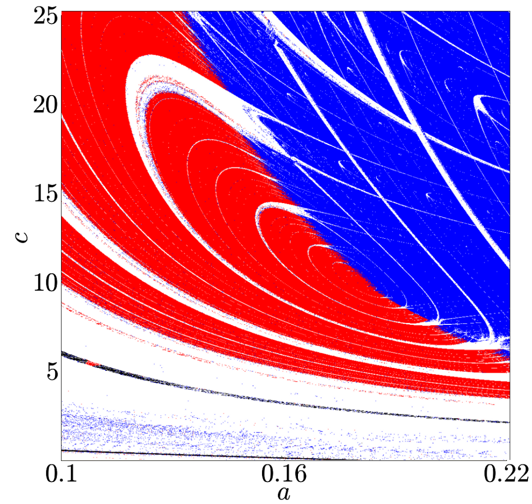

Figure 6.3: A numerical analysis of the region from Figure 6.2 shows regions in which the topology of the Rössler attractor is described by a two-branched branched manifold (lower red region) and that described by a three-branched branched manifold (upper blue region). The white region represents areas in which our numerical algorithm could not make a determination or where there exist regions of superstable periodic orbits. The scatter of colors in the lower stable regions is numerical artifact. The divide between the branch-two and branch-three regions is defined by the same partition of the primary hub as that found in Figure 6.2.

bifurcation, as critical slowing down retards decay of transients [204].

6.1.2 Spiral hubs are Robust With Variation in b

The spiral hub patterns we see in the Rössler dynamical system are not anomalous for the parameter range we selected in Figures 6.1 and 6.2. As the parameter b is changed, the center of the hub moves along the topological transition line (which separates the 2-branch region from the 3-branch region), and the shape of the hub changes very slightly, but the overall structure of the hub is consistent for all parameter ranges of b. We demonstrate how it evolves with b in Figure 6.4. The shift of the hub is due to the shift of the curve of the Andronov-Hopf bifurcation of the Rössler system rightward as b increases. We will return to a discussion of this bifurcation later in this chapter.

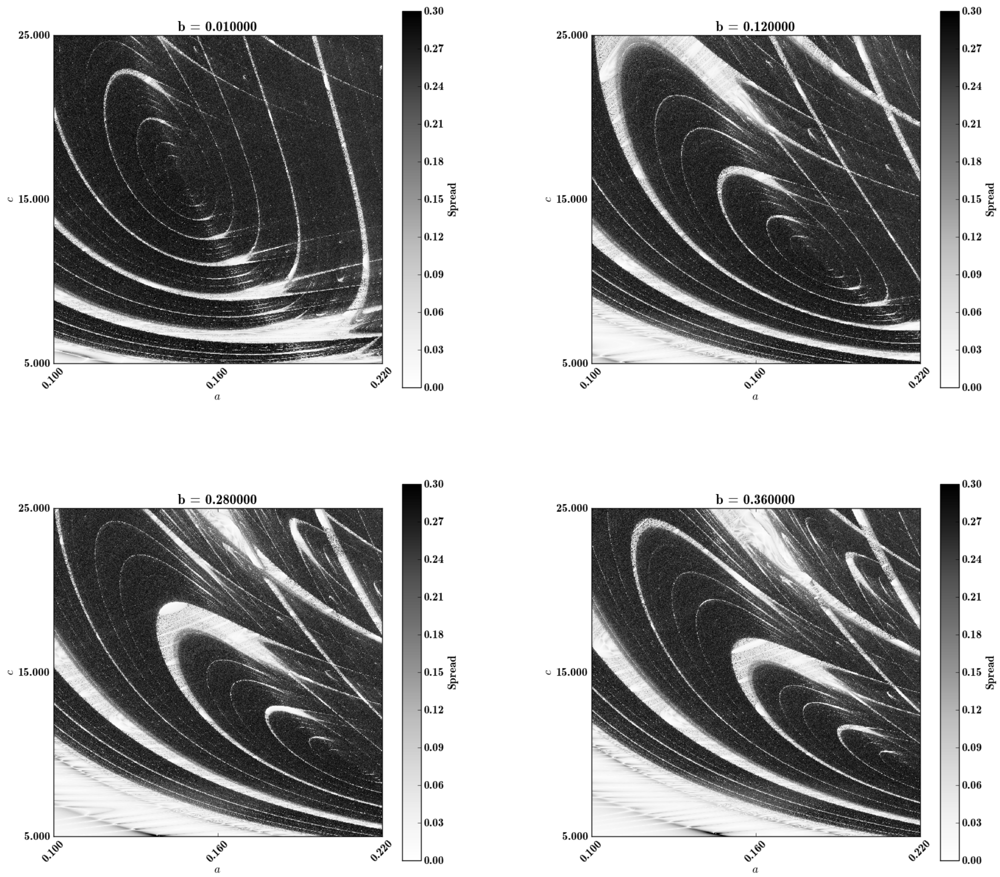

Figure 6.4: The spiral hub in the Rössler codimension-2 parameter plane are robust under a change in b. Grey scale coding of percentage of partitions of return-map which are occupied by a point in a trajectory, darker colors corresponding to more chaotic behavior. Top Left: $b = 0.01$, Top Right: $b = 0.12$. Bottom Left: $b = 0.28$, Bottom Right: $b = 0.36$.

6.2 Caustics in the Bifurcation Diagrams

It has been noted in the literature [194, 197] (both studies did not consider the Rössler system) that a bifurcation diagram[3] taken along the best-fit curve linking the centers of the shrimp structures in the primary hubs has a symmetry that hasn't been accounted for. We find a similar symmetry in in the bifurcation diagram taken along the shrimp-laden curve that bisects the primary hub (see Figure 6.5). The symmetry can be seen in the orbit ordering from the point at which the attractor

[3]There are multiple types of bifurcation diagrams, just as there are multiple types of bifurcations. Unless otherwise specified, when we refer to bifurcation diagram, we mean a graph for which the x axis represents a parameter, the y axis represents positions of points on a Poincaré section, and data points represent the position at which an orbit intersects the Poincaré section for the given parameter. This diagram has been called an "attractor diagram" [205], but the most common name in the literature remains the vague "bifurcation diagram".

makes contact with its fixed point (the homoclinic bifurcation), and with the caustic patterns.

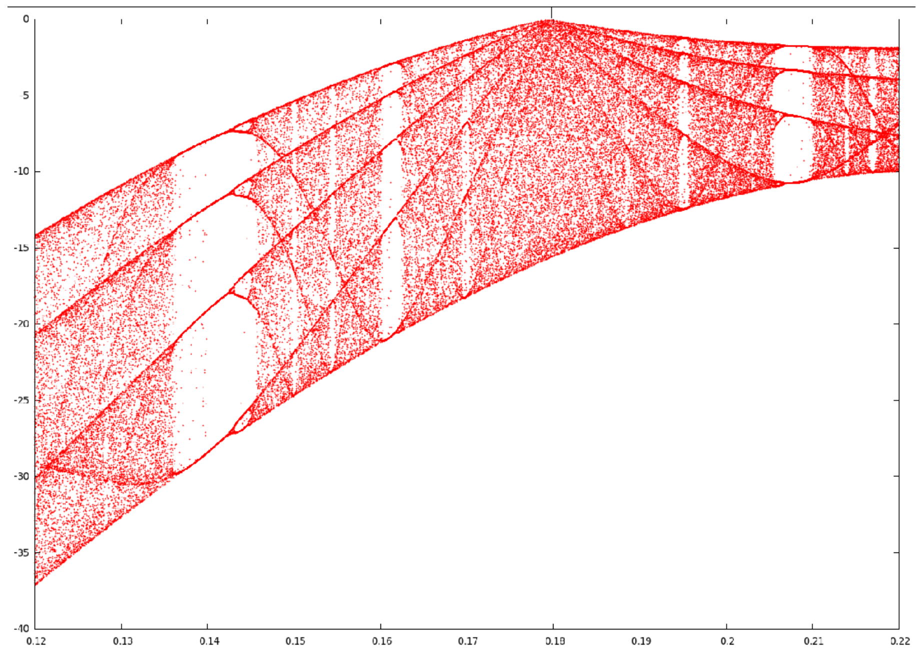

Figure 6.5: Bifurcation diagram along best-fit curve of Equation 6.2, TTL_3^2. The center is focal point (0.1798, 0.2, 10.3084). We take Poincaré sections on the Rössler attractor as defined at the line $(y = 0, x < (c - \sqrt{c^2 - 4ab})/2)$. Compare with Fig 2.c and 4 in [194] and [197] respectively.

Unfortunately, these researchers mentioned this symmetry only in passing. It turns out that the root of this symmetry is at the heart of the dynamical mechanism that creates the primary spiral hub pattern.

6.2.1 Iterates of the Critical Point of Unimodal Map

To paraphrase one of the pioneers of chaos theory (as quoted in [18]), it is a happy coincidence that the bifurcation diagram of the Rössler system for low parameter values corresponds to a nearly bijective mapping with the bifurcation diagram of the Logistic Map system [80] when one passes through a certain parameter regime, as this mapping is one of the most well studied in nonlinear dynamics and yields a rich set of tools that can be transposed into an investigation of the Rössler dynamical system in the low parameter regime where it is highly dissipative and has only two branches.

What stands out very clearly in this map are the “caustics” or scars in the bifurcation diagram.

These caustics are not as widely understood as they could be, as most textbooks on nonlinear dynamics don't mention them (exceptions include [40, 206]). These caustics turn out to hold the key to understanding the stable periodic windows in the Logistic map, and by extension, the mechanisms inducing periodicity transitions along and among spirals.

It was once considered a "hopeless problem" [57] to decide on the occurrence or absence of stable periodic orbits of unimodal maps based on the analytical form of a one-dimensional map. While one can analytically solve this problem for the lower periods, the analytical method becomes increasingly difficult as we consider higher periods. For example, the classic Logistic map,

$$L(x_n, r) = x_{n+1} \equiv r x_n (1 - x_n) \tag{6.3}$$

will have a period two orbit whenever

$$L_2 \equiv L(L(x, r)) = x_{n+2} = x_n \tag{6.4}$$

and so on. One method of finding stable periodic orbits of period p in the Logistic map is to solve the equation,

$$L_p(x, r) = x \tag{6.5}$$

However, such an equation becomes exceedingly difficult to solve, especially for large p.

Fortunately, this problem is not so "hopeless" after all. A method of analytically detecting periodic windows in the general class of Logistic type maps was introduced by the seminal work of Metropolis et al. in 1973 [30], and rediscovered by Jensen and Myers in 1985 [205, 207] (the authors do not appear to have noticed the work of Metropolis et al. on this point, and in any case, they go into greater detail regarding the Logistic Map). Froyland (1992) [40] appears to be the first to have discussed these caustics in a text book, and Stefanski (1999) [208] put these findings into a more mathematical context.

Rather than posing the problem of solving an exceedingly complex iterative equation for the

Logistic Map class of systems, we instead only need to study the iterations of the critical point. Instead of solving an increasingly complex polynomial, we need only repeatedly apply the Logistic Map equation to the critical point. Whenever one of these iterations of the critical point intersects the critical point, we are assured of the existence of a super-stable periodic orbit which corresponds to one of the windows of stability in the Logistic Map's bifurcation diagram. This superstability is due to the fact that the slope at the critical point is zero, and so the stability of the periodic orbit is thus maximal since it is proportional to the slope (derivative). These iterations of the critical point "scar" the bifurcation diagram and stand out due to a higher concentration of "hits" around these points.

The critical point of the Logistic Map will be found at,

$$\frac{dL(x,r)}{dx} = r\,(1-2x) = 0 \tag{6.6}$$

with critical point $\bar{x} = 1/2 = g_0(r)$, where we use the g_p notation for the p^{th} iteration of the critical point after that introduced in [208]. The next three iterations are given as

$$\begin{aligned} g_1(r) &= \frac{r}{4} && (6.7) \\ g_2(r) &= \frac{r^2}{4}\left(1-\frac{r}{4}\right) && (6.8) \\ g_3(r) &= \frac{r^3}{4}\left(1-\frac{r}{4}\right)\left(1-\frac{r^2}{4}\left(1-\frac{r}{4}\right)\right) && (6.9) \end{aligned}$$

So, for example, to locate the value r_3 at which the period-three window in the Logistic Map occurs, we need to solve, numerically or analytically, the equation

$$\frac{r^3}{4}\left(1-\frac{r}{4}\right)\left(1-\frac{r^2}{4}\left(1-\frac{r}{4}\right)\right) = \frac{1}{2} \tag{6.10}$$

The x value for r_3 of the points on the orbit will then be given by (g_0, g_1, g_2). Evaluated at $r = r_3$, Equation 6.10 has only one unknown, whereas the means of finding this period by solving the third iteration of the logistic map, i.e. finding the point where,

$$-r^3x\,(x-1)\left(1-rx+rx^2\right)\left(1-r^2x+r^3x^2-2r^3x^3+r^2x^2+r^3x^4\right)=x \tag{6.11}$$

involves two unknowns and drastically more complicated algebra that quickly becomes unmanageable.

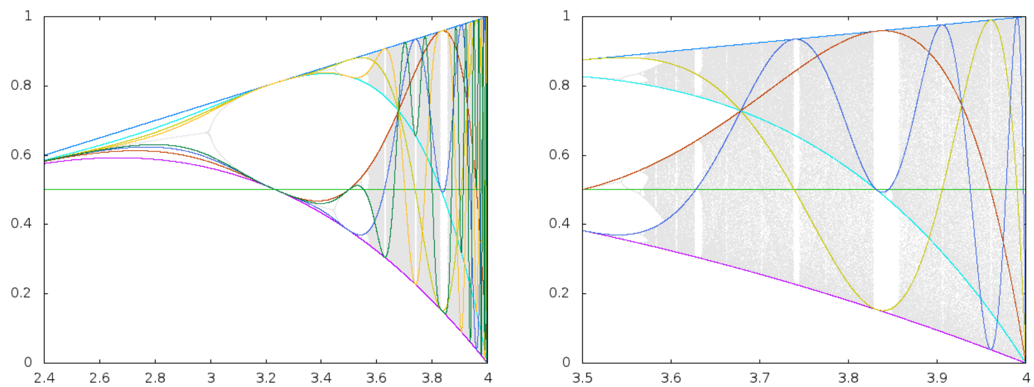

Figure 6.6: Periodicity Bifurcation diagram of Logistic Map with first eight caustics shown (left) and a closer view with the first six caustics shown (right). The central green line is the critical point for the Logistic Map given by Equation 6.3. Whenever a caustic crosses the line corresponding to a critical point, we have a window of stability. The sudden explosion of chaos after the stability windows, seen clearly in the period-3 window, are called "interior crises" [209] and are due to the attractor encountering an unstable periodic orbit in the basin of attraction (in this case, an unstable period-3 orbit [207]. This is in contrast to the boundary crises that happens at $r = 4$, in which the attractor encounters the edge of its basin of attraction and diverges to infinity.

A further advantage of the caustic method is that this method also encodes the order of orbits of the super-stable orbits [30]. Ott [206] gives an example for a period four super-stable orbit. Recall that when defining orbits by their symbols, we partition the Logistic Map at its critical point. All points to the right of the critical point are labeled R or 1, and all orbits to the left are labeled L or 0. Metropolis et al. [30] showed that if two separate orbits are found at points r_m, r_p where $r_p > r_m$, then all orbits between them in the Sarkovskii [210] order of orbits must have occurred in the range $r \in (r_m, r_p)$. Using Ott's example, if a period nine super-stable orbit occurs at r_m with symbols RL^2RLR^2L, and a period four orbit with symbol sequence RL^2 appears at $r_p > r_m$, then a period five can be found somewhere in $r \in (r_m, r_p)$ with orbit RL^2R. Also, the caustic method offers a quick shorthand for obtaining the kneading invariant of a super-stable periodic orbit, as the order of the symbols will follow the order of the iterations of the critical point, something which can be obtained numerically or graphically. For example, in Figure 6.6, the period three window occurs when the caustic corresponding to the third iterate of the critical point (light blue line) intersects the critical point (green line), and we can read off the order of the symbol sequence by the order of the caustics corresponding to the iterates. The second iterate is the next iterate, and it is on the rightmost branch of the Logistic Map, which we can label 1. The third iterate is the leftmost branch (purple line) which we can label 0. Thus if we label the critical point C, we have the orbit $C10$. The largest window before the period three window in Figure 6.6 is a period five window, and with a little more work we can read off the sequence as $C1011$.

6.2.2 Caustics in the Rössler Bifurcation Diagram

Using a common Poincaré cross section for the Rössler attractor ($y = 0, x < (c - \sqrt{c^2 - 4ab})/2$)[36], we construct a return map for points along TTL_3^2 (Figure 6.5). This bifurcation diagram displays evident symmetry at the focal point of the hub. The symmetry in this bifurcation diagram at the focal point of the spiral hub suggests that we should consider other bifurcation diagrams along lines parametrized such that they terminate at the focal point. In fact, the focal point is the terminus of a homoclinic bifurcation in the Rössler attractor [79, 86, 93, 200], that is, the point where the attractor has expanded into its inner-region and made contact with the inner fixed point in the form of a homoclinic orbit.

Since the hub is stretched in its upper half, we take a horizontal cut and a vertical cut in parameter space connecting points along the Andronov-Hopf bifurcation with the point on the homoclinic bifurcation curve which intersects the line of topological transition from branch-2 to branch-3. These lines are $L1 : b = 0.2, c = 10.3084, a \in [0.01, 0.1798]$, and $L2 : a = 0.1798, b = 0.2, c \in [4, 10.3084]$ (Figure 6.8). For all slices for which the topology of the attractor is spiral (number of branches in the return map is two), the bifurcation diagram is qualitatively similar to that of the Logistic Map. While we will demonstrate this up to super-stable period seven orbits using the caustics method, we take it assume that:

The return map for the Rössler attractor under the branch-two manifold regime is at

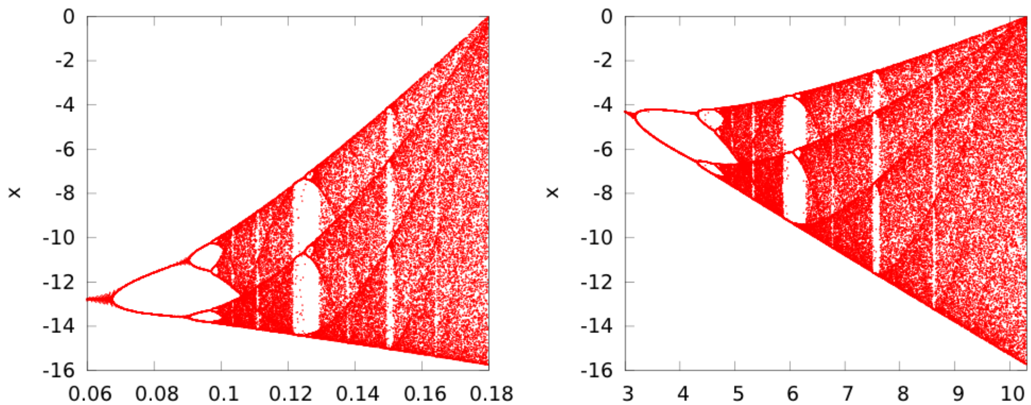

Figure 6.7: Bifurcation diagram taken along the line $L1$: $b = 0.2, c = 10.3084, a \in [0.01, 0.1798]$ (left) and $L2$: $a = 0.1798, b = 0.2, c \in [4, 10.3084]$ (right). The bifurcation diagram terminates at the point where the return map acquires a third branch. The map qualitatively corresponds to that of the Logistic Map, although there are obvious scaling differences. These scaling differences are due to the morphology of the attractor for differing parameter ranges.

topologically conjugate to the Logistic Map up to and including period seven.

In any case, we find that the return map for the Rössler system behaves *as if* it were topologically conjugate to the Logistic Map for the periodic orbits we will be considering. The reader is referred to Gilmore and LeFranc (2002) for further discussion on this point [36].

6.3 Origin of Hub-Shape in Rössler's Codimensional-2 plane

Next we examine the bifurcations of the Rössler attractor for the parameter region near the spiral hub structure that is at the center of Figure 6.2. Using numerical continuation software [211, 212], we locate the Andronov-Hopf bifurcation curves and note that lines $L1$ and $L2$ originate from these curves. Behavior left of the Andronov-Hopf bifurcation curve is dynamically uninteresting, as it corresponds to fixed points. Points right of the Andronov-Hopf curve are dynamically interesting because the curve denotes the formation of a period-one limit cycle. As we travel rightward, away from the the Andronov-Hopf bifurcation curve, we find that the Rössler dynamical system undergoes period doubling and saddle-node bifurcations. We note the following important points.

From any line connecting the Andronov-Hopf bifurcation curve to the homoclinic point at the center of the spiral hub on the TTL_3^2, the Rössler's return map is unimodal. After

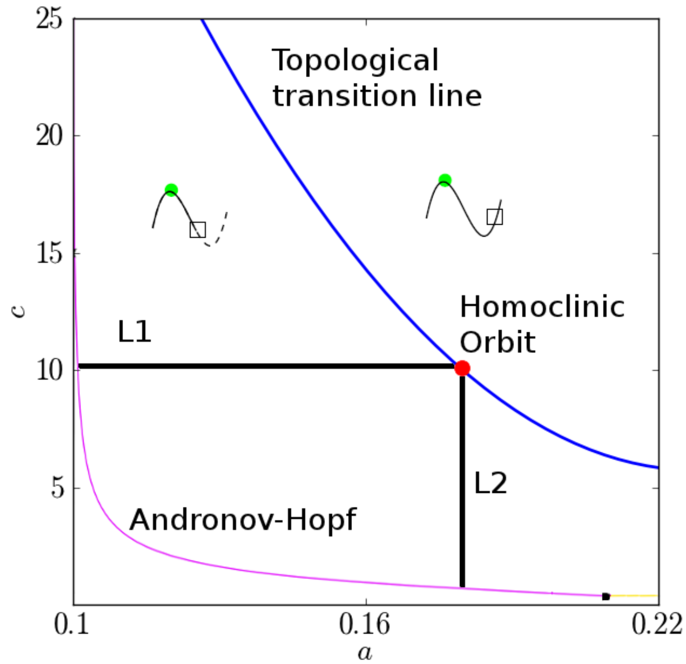

Figure 6.8: Bifurcation diagram using PyCONT/AUTO [211, 212]. The bifurcation diagrams L1 and L2 (Figure 6.7) originate from the Hopf bifurcation of the Rössler attractor and terminate at a Homoclinic bifurcation point on the curve demarking the topological transition from two to three branches in the branched manifold. We exclude the continuation of the homoclinic bifurcation curve into the three-branch region for simplicity. $p1 = a$ and $p2 = c$, the Rössler system parameters.

that point, it becomes bimodal.

We have shown this point numerically. We will return to a discussion of the bimodal portions of the codimension-2 space in later sections, as this region contains the second half of the spiral hub. For now we will only focus on the region in which the Rössler's return-map is unimodal.

> *Assuming that the dynamics of the Rössler system is topologically conjugate with that of the Logistic Map for lower periods wherever its return-map is unimodal, we require a one-to-one correspondence between the dynamical behavior of the Rössler and the Logistic Map.*

This follows from the definition of topological conjugacy. While the Rössler system return map is not perfectly topologically conjugate to the Logistic Map for reasons stated previously (i.e. the conjugacy breaks down a higher periods than we consider), we will demonstrate numerically in later sections that its behaves *as if* it were at least topologically conjugate for lower periods. We do not consider periods high enough to encounter this break of conjugacy, and so we make the following assumption:

> *In the codimension-2 plane (a,b), if we follow the evolution of the Rössler system from a point on the Andronov-Hopf bifurcation curve to the homoclinic point, where the Rössler strange attractor touches its central fixed point, then we expect to find that this corresponds to the evolution of the Logistic Map (for periods up to period seven) from its initial period one orbit to* $r = 4$*, where the critical point of the Logistic Map is mapped to an (unstable) fixed point (*$x = 1/2 \to 1 \to 0$*).*

This point is a delicate one. In the Logistic Map, the first iteration of the critical point marks the furthest position of all possible orbits. At the parameter value $r = 4$, the critical point is mapped in two steps, finally, to a fixed point of the system. Similarly, with the Rössler return map, the mapping of the effective critical point will correspond to the furthest boundary of the attractor itself in $\mathbf{R}^3$ along the Poincaré slice. Thus, when the Rössler attractor intersects with the central fixed point of the spiral hub, we are assured that this corresponds to the mapping of the critical point of the return-map to the fixed point.

It must be noted that the Rössler's return map is not a two-dimensional curve, but rather a fractal curve. Due to the highly dissipative nature of the Rössler flow, the Rössler return map is very thin (fractal dimension $1 + \epsilon$, $\epsilon << 1$. Thus the return map does not deviate from unimodal behavior in any substantial way. The deviation from a smooth curve acts as a slight perturbation for very higher periodic orbits, a regime which we do not consider.

The next point is key in explaining the shape of the spiral-hub, and we call upon the requirements that the evolution of periodic orbits be continuous with parameter change [36] except at points of creation/annihilation.

> *Since the Andronov-Hopf bifurcation curve is continuous, and due to the effective conjugacy between the Rössler and the Logistic Map along lines connecting the Andronov-Hopf*

bifurcation curve with the homoclinic point, and because we require continuity of periodic orbits with the variation of parameters a and b, the super-stable periodic orbit pattern seen in the Logistic Map will correspond to bands of super-stability in the Rössler codimension-2 plane along these lines, resulting in a smooth hub-shaped pattern.

We will demonstrate that this is the case in the next sections.

6.4 Surrogate Analytical Method

Since the periodicity windows of the logistic map are explainable in a concise analytical way, we should like to find a similar analytical method for the Rössler system. Unfortunately there is no known method of achieving this, and it may not be possible, so we instead use a semi-analytical method in which the return map for the Rössler system is approximated with best-fit curves, giving us a numerically approximated surrogate set of analytical equations from which we can derive an analysis of the caustics.

6.4.1 Caustics in a Rössler Hub

In order to form a surrogate model for the Rössler return map, we scan the return map for the Rössler system along a line that originates in the period-one region to the right of the Andronov-Hopf bifurcation curve and terminates at the focal point of the hub (the terminus of the homoclinic bifurcation curve that sits on TTL_3^2).

Along this line, we construct thousands of return maps to which we fit a polynomial best-fit value of order 12 using the Matlab polyfit routine. We exclude locations of super-stable periodic orbits by only considering regions in which the positive Lyapunov exponent is above a certain threshold, given as $\gamma_1 > 0.03 + 0.03 * (a - 0.1)$. This is a heuristic fit (along the lines of [213] Figure 1) designed to match the fact that the trend of both the maxima and minima of the Lyapunov exponent slopes upwards with increasing a as seen in Figure 6.9. This upwards slope was found by Huberman and Rudnick in 1980 to behave as $\bar{\lambda} = \bar{\lambda_0}\,(a - a_c)^t$ [214] where a_c marks the onset of chaotic behavior, $\bar{\lambda}$ is the largest Lyapunov exponent, and $\bar{\lambda}_0$ is fit close to unity.

The coefficients of the best-fits for the return maps shows a regular pattern that suggests the

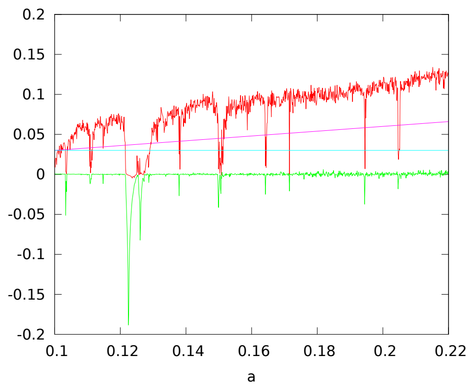

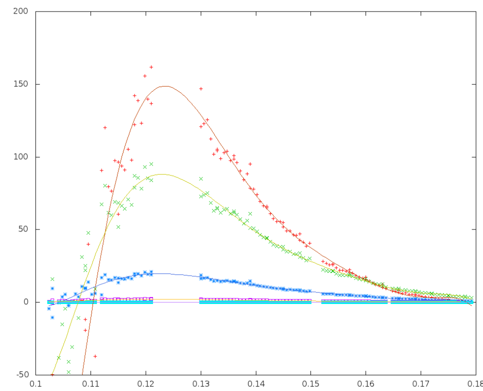

Figure 6.9: Left: Heuristic cut-off for positive Lyapunov coefficient of the Rössler attractor. The magnitude of the positive Lyapunov exponent λ_1 is colored in red, λ_2 is colored in green. The cutoff $\lambda_1 = 0.3$ is colored blue and is effective, but the cuttoff $\lambda_1 = 0.3(x - 0.1)$ is colored in violet and excludes more regions of stability (which can't be seen due to resolution of the λ_1 magnitude). Right: Plot of the coefficients found with our Matlab optimization program and their best-fit lines.

possibility of paramaterizing a more global model of the return map (Figure 6.9) by fitting the coefficients of the individual best fits to a global best-fit model. However, experience has shown us that although such a model gives a good qualitative representation of the caustics in the Rössler return map, it fails to yield excellent quantitative results.

We instead use what we call a surrogate analytical method in which, over a range of thousands of points in a slice of codimension-two parameter space, we construct best-fit models for the actual return map for that point, and identify the iterations of the critical point of the best-fit of the original return-map, with that return map as a set of points to be fitted for a caustic map over the entire range (see Figure 6.10)[4].

This method yields results which reconstruct the caustics of the Rössler return map. As we go to higher and higher iterations of the critical points, the accuracy declines. This can be overcome by introducing the restriction to the best fit curves for the return maps of the position of the critical point as fitted by the global model, such that each individual surrogate model must pass through the predicted position of the critical point. Further accuracy of the model can be obtained by also forcing the best-fit return map to pass through the predicted value of the first caustic, ad infinitum.

[4]An alternative method for identifying the shape of the return map for regions of stable periodicity is called the sprinkling method [215]

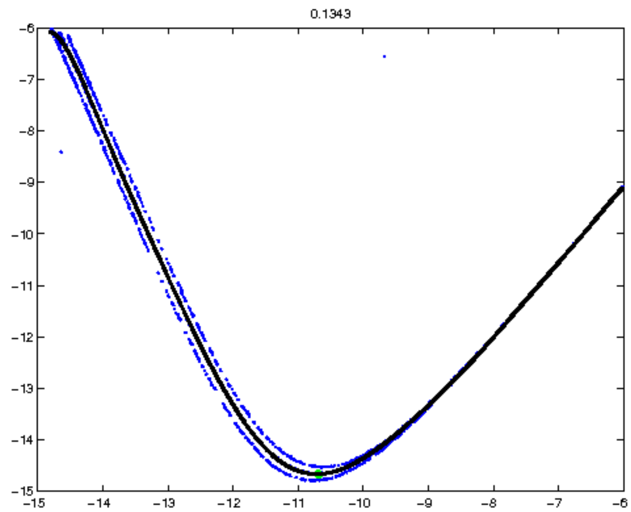

Figure 6.10: A best-fit polynomial fit of a return map (black) constructed for a super-stable point on the bifurcation diagram by constraining the fit to the predicted position of the critical point based on previous fits as well as using return-map perturbation analysis to predict the probable position of the return map.

A final method to improve accuracy is a return-map perturbation analysis (Figure 6.10) based on the topological stability of the Logistic Map (and by extension the Rössler return map when two-branched). In order to increase the accuracy of the surrogate caustics model, we need to compensate for the lack of enough data points in super-stable regions in order to obtain a surrogate for the return map at that instance. We know that the regions of super-stability are found as one-dimensional curves in the biparameter Lyapunov space, and so for each point (a, c), we also obtain the return map for the points $(a+\epsilon, c-\epsilon)$ and $(a-\epsilon, c+\epsilon)$ where ϵ is much smaller than the scale on which we are constructing our surrogate caustics model ensuring that these additional two points represent only very small perturbations to the shape of the original return-map, one which is slightly above the original return map, and one which is slightly below it.

Thus along the lines $L1$ and $L2$ (see Figures 6.9), we partition the line into thousands of points and model the return map of the Rössler system, using nearest neighbors to improve the approximation, for each point. We then calculate the critical point for each model, and seven iterations of the critical point assuming unimodal behavior. The first five iterations are plotted for each of the points on the

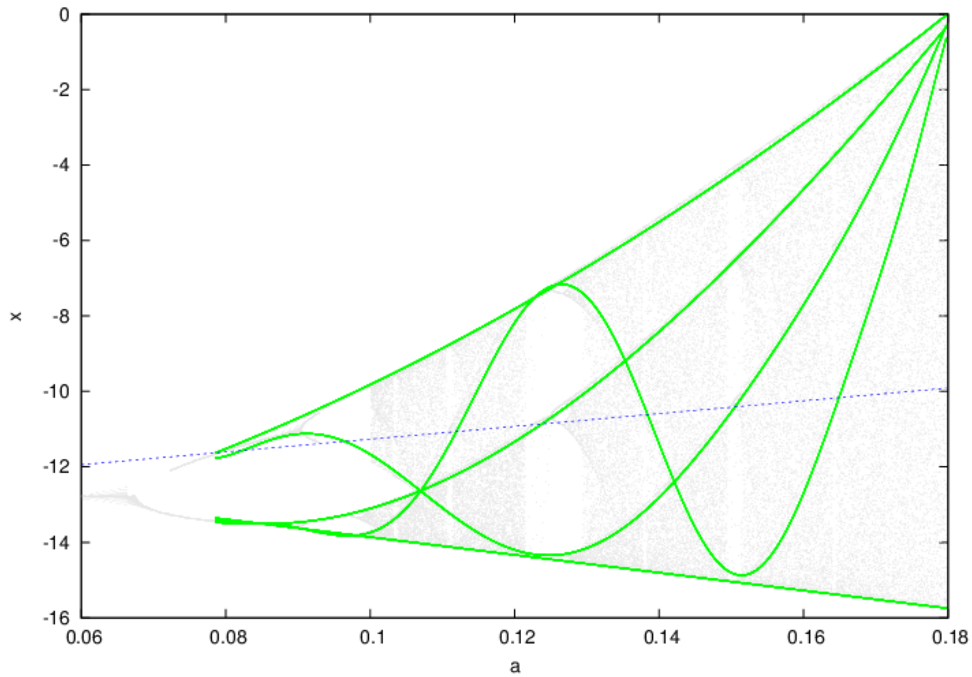

Figure 6.11: Surrogate caustic values and numerical bifurcation data for the Rössler bifurcation diagram in the bi-parametric slice $b = 0.2, c = 10.3084, a \in [0.01, 0.1798]$. The first five iterations of the best-fit surrogate critical points shows strong correlation with the bifurcation diagram. Remaining caustics up to period five are excluded for clarity.

line, and the collected plot yields an accurate representation of the caustic pattern of the Rössler bifurcation diagram (Figure 6.11).

We have thus shown, for the lines $L1$ and $L2$, that the Rössler return map, for the superstable orbits up to period seven at least, is conjugate to the unimodal map represented by the Logistic Map. Our next task is to demonstrate that this is the case for all lines originating from the Andronov-Hopf bifurcation curve to the homoclinic focal point.

6.4.2 Continuity of Superstable Orbits in the Rössler Codimension-2 Plane: The Unimodal Side

In order to confirm our conjecture about the origin of the hubs, it is necessary to produce a high-resolution codimension-2 periodicity graph. While integration of nonlinear equations is, for the most part, an inherently serial calculation, mapping a codimension-2 phase plane represents a large number of independent serial calculations, and in such a situation, the use of parallel computation implementation becomes practically necessary. We use the Message Passing Interface [216] and set our resolution to a $5000 \times 5000 = 25 \times 10^6$ partition of the phase plane.[5]

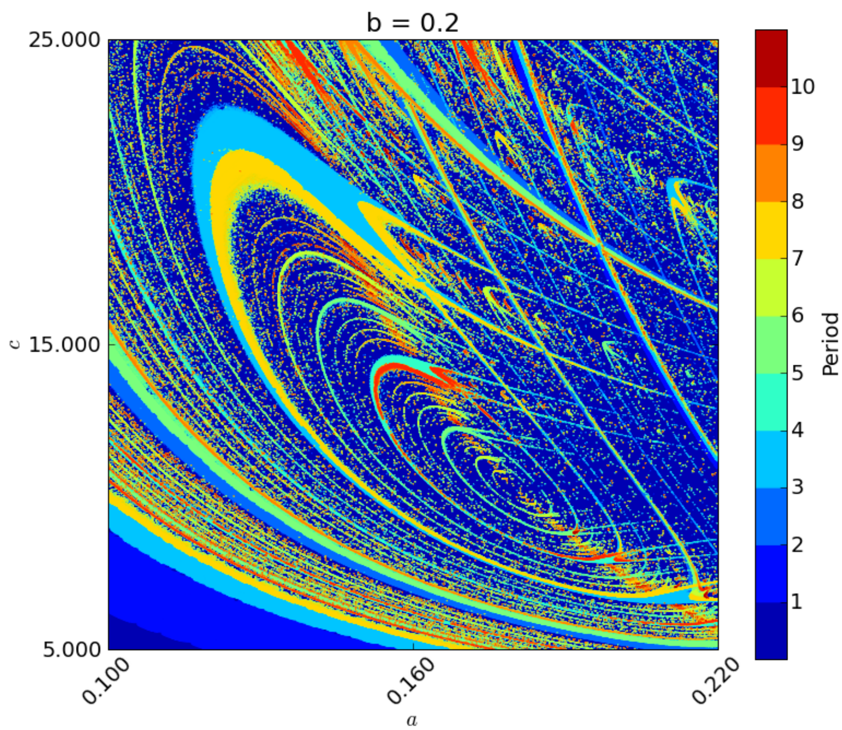

Figure 6.12: Periodicity calculations for the codimension-2 parameter space of the Rössler attractor, for $b = 0.2$, $a \in (0.1, 0.22)$, $c \in (5.0, 25.0)$. The parameter space is divided into a 5000×5000 grid for 25×10^6 independent calculations. Periodicity detection was programmed to be triple checked to ensure accuracy. Darkest blue corresponds to divergent or chaotic behavior.

In Figure 6.12, we find that for the side of the hub in which the Rössler attractor is described by a two-branched branched manifold, there is a uniformly smooth (though warped) regularity to the organziation of the super-stable regions that partition the chaotic regions. We can also see the regular cascades of period-doubling bifurcations that occur wherever a region of super-stability appears (moving inward towards the focal point). We also note that in Figure 6.12, the curve through which the topology of the Rössler system changes (TTL_3^2) is very clearly marked by the sudden appearance of "shrimp" shapes, which we will discuss in the next section. It turns out that

[5] We thank Drs. Yuan and Vallieres for generous use of their computational clusters for these calculations, and Wolfgang Nadler and Maryann Fitzpatrick for help building a beta-testing cluster.

these shrimp present a pattern atypical of bimodal maps.

> *An open problem remains the question of whether or not the curve marking topological transition can be described with an analytical expression. While we would naturally expect such a transition line to be smooth given continuity conditions, this does not necessarily imply that this line can be calculated explicitly.*

6.5 Continuity of Super-stable Periods in the Rössler Codimension Plane: The Bimodal Side

As discussed in the previous chapter, the so-called “shrimp” structures in codimension mappings are never found in unimodal maps due to the fact that they represent the coexistence of regions of super-stability (unimodal maps can only have one superstable periodic orbit at a time). At the very center of these shrimps, one finds a degenerate super-stable state which corresponds to the fact that at these points, two intersecting regions of super-stable periodicity contain both fixed points simultaneously [190]. Careful consideration of the conditions at the intersection of the topological regions will help us understand why the shrimp line up along the transition curve.

First, we recall the fact that these super-stable regions represent iterations of at least one critical point of the return-map. The critical point maps to the borders of the range of possible iterations, first to the maximal value, and then to the minimal value. As the Rössler's return map passes through the topological transition, one of those extremes becomes, first, a critical point, and this grows into a third branch (Figure 6.14).

> *Where iterations of the critical-point are super-stable at the border of topological transition where the Rössler's return map becomes bimodal, the original critical-point will be mapped to the secondary critical point, a conditions which places it at the degenerate center of a “shrimp”. See, for example, Figure 6.14.*

We thus see that the shrimp are constrained to line up along this curve by the nature of the transition from unimodal to bimodal mappings. Of course, we should note that there are plenty of “shrimp” beyond this transitional curve, an example is shown in Figure 6.15.

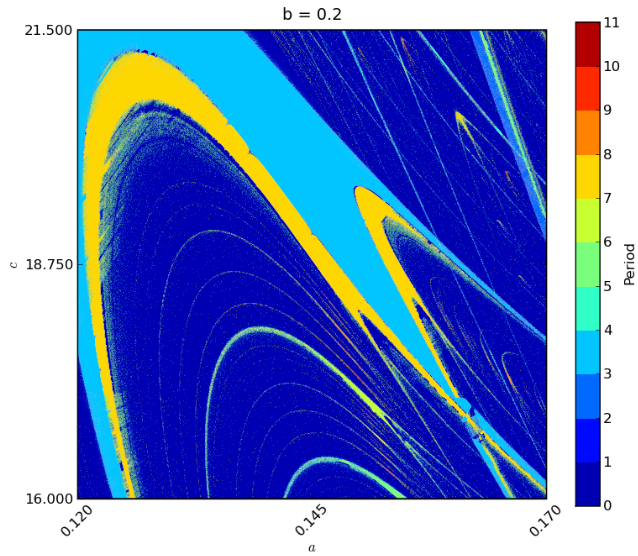

Figure 6.13: Periodicity calculations for the codimension-2 parameter space of the Rössler attractor, for $b = 0.2$, $a \in (0.12, 0.17)$, $c \in (16.0, 21.50)$. The parameter space is divided into a 5000×5000 grid for 25×10^6 independent calculations. Periodicity detection was programmed to be triple checked to ensure accuracy. Darkest blue corresponds to divergent or chaotic behavior. Where the graph looks disjointed (near (17.0, 0.165) for example), our initial condition "hopped" from one basin of attraction to another. This is a phenomenon which can only happen in multimodal regions where coexisting superstable orbits exist, and is due to the fractal nature of the strange attractor's basin of attraction.

> *Where iterations of the critical-point are super-stable at the border of topological transition where the Rössler's return map becomes bimodal, the original critical-point will be mapped to the secondary critical point, a conditions which places it at the degenerate center of a "shrimp". See, for example, Figure 6.14.*

We thus see that the shrimp are constrained to line up along this curve by the nature of the transition from unimodal to bimodal mappings. Of course, we should note that there are plenty of "shrimp" beyond this transitional curve, an example is shown in Figure 6.15.

Comparison with the Rössler system

If we compare Figure 5.7, which is a section of codimension-2 parameter space for one of the two normal forms of bimodal maps, with Figure 6.16, we find that the order in which the superstable

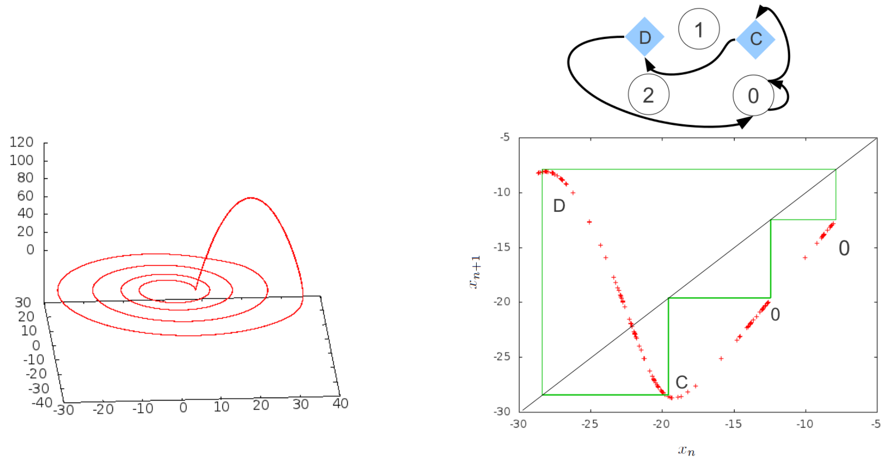

Figure 6.14: We use the return map for $a = 0.147$, $b = 0.21$, $c = 20.3$ to approximate the outline of the functional return map curve for $a = 0.145$, $b = 0.2$, $c = 20.125$, a period four orbit with symbolics C100=CD00 (we represent the rightmost critical point as C and the leftmost critical point as D, and at the topological transition line, the furthest point on the branch labeled 1 becomes a critical point). This orbit is at the degenerate core of a shrimp and the iterations of the first critical point includes the newly formed second critical point. Shown above the return map is a modified transition graph for this orbit.

shrimp appear are quite similar. The distinct differences come from the symmetry that the Rössler parameter space possesses around the focal point (where the homoclinic bifurcation curve intersects the topological transition curve). This ordering is mirrored on the other side of the focal point in the Rössler parameter plane. Closer inspection reveals a decidedly unexpected asymmetry which we will address in the next section.

6.5.1 Asymmetry in the Spiral Hub and Mutant Shrimp

In the wider view of the spiral hub (Figure 6.12), we see that the shrimp along the topological transition line, for points above the focal point, behave as we would expect in the bimodal regime. One of the "tails" of each of the shrimp point downward back towards the hub. This "tail" joins a shrimp below the focal point. A closer inspection of the shrimp below the focal point (Figure 6.18) shows that the tail joins a "shrimp" of a distinctly different period. We affectionately call these lower "shrimp" "mutant shrimp", as they posses a tail which has a period which is not the same as the other three tails. For example, in Figure 6.18, the tail of the upper period three shrimp merges with the lower period four shrimp. (We might just as well say that the mutant tail of the lower

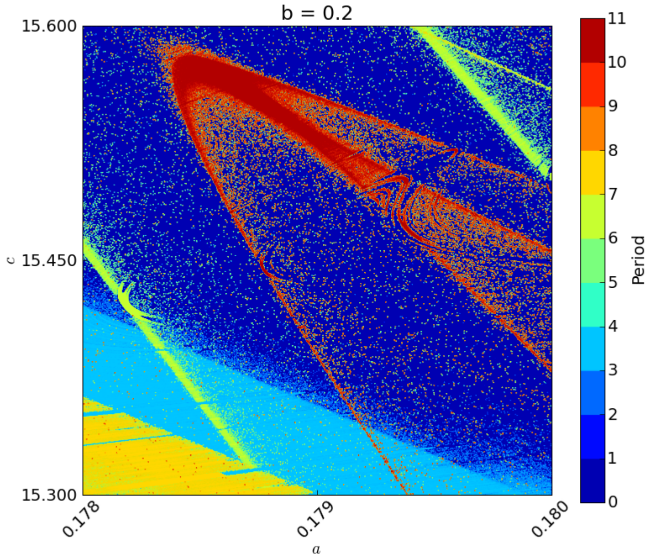

Figure 6.15: Periodicity calculations for the codimension-2 parameter space of the Rössler attractor, for $b = 0.2$, $a \in (0.178, 0.180)$, $c \in (15.3, 15.6)$ which is well within the bimodal region of the codimension-2 parameter plane. The parameter space is divided into a 5000×5000 grid for 25×10^6 independent calculations. Periodicity detection was programmed to be triple checked to ensure accuracy. Darkest blue corresponds to divergent or chaotic behavior. Where the graph looks disjointed (near (17.0, 0.165) for example), our initial condition "hopped" from one basin of attraction to another. This is a phenomenon which can only happen in multimodal regions where coexisting superstable orbits exist, and is due to the fractal nature of the strange attractor's basin of attraction. This "shrimp" is found well-within the bimodal region of the codimension parameter space of the Rössler attractor and represents a more classic case of the "shrimp" or "swallow-tail" shape. The striations in this graph remain an open question and are discussed further at the close of this chapter.

period four shrimp merges with the period three shrimp, but the latter merger is more natural in that the tail is joining up with a body of the same period). It is this "mutation" which results in the inward spiral of the super-stable regions, and finding the causation for this will bring us to a more complete description of the spiral hub feature. To date, no mechanism has been produced to explain this phenomenon. We introduce such a mechanism below.

First, we pause to make it clear that our assumption of conjugacy proposes only that the Rössler return map is topologically (semi)conjugate to the Logistic Map in the branch-2 region of codimension-2 phase space. It turns out that there is a discontinuity to this conjugacy along TTL_3^2 below the homoclinic point at the center of the spiral hub. One result of this fact is that the

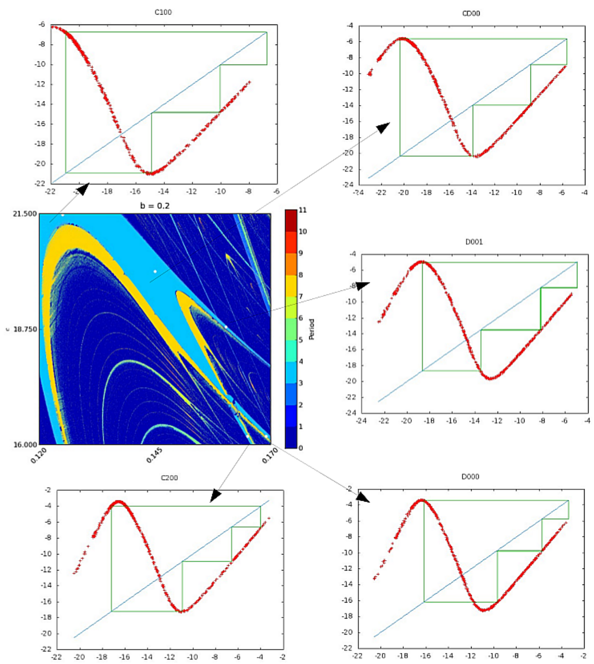

Figure 6.16: Periodicity calculations for the codimension-2 parameter space of the Rössler attractor, for $b = 0.2$, $a \in (0.178, 0.180)$, $c \in (15.3, 15.6)$ with return-map and symbolic calculations. The parameter space is divided into a 5000×5000 grid for 25×10^6 independent calculations. The "shrimp" represent the intersection of two parabolas of superstability which have differing orientation. The parabola pointing towards the branch-3 region have symbolics that always include the leftmost critical point. The parabola which is half-oriented in the branch-2 region have symbolics that always include the rightmost critical point, which is the one associated with the unimodal map.

Poincaré section we have been using is no longer a valid Poincaré section at this discontinuity.

This is due to the fact that the tail of the Rössler attractor "lands" on the plane of the main attractor at different angles relative to the central fixed point. This angle is dependent upon the parameters a and c of the attractor. Figure 6.21 shows this using the transition from the period-3 to period-4 superstable regions. The landing point, where the furthest outward iteration of the critical point is mapped to the inner region of the attractor, is key to the "squeeze" part of the "stretch and squeeze" mechanism of chaos. It is because the Rössler system is such a strongly dissapative

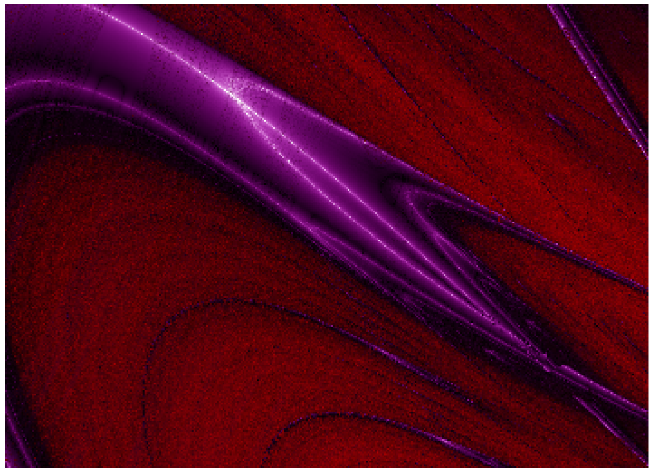

Figure 6.17: Lyapunov exponents map for region shown in Figure 6.16.

system, where the flow is compressed to the main circular plane of the attractor, that we have a relatively smooth return-map. As the flow is mapped away from the central point, it eventually encounters a region in which it pulled upwards above the plane of the main-region of the attractor, before being squeezed back onto the plane towards the inner region near the fixed-point. Without this latter mechanism, the flow would spiral away from the central fixed point until it encountered the boundary of its basin of attraction, at which point it would diverge to infinity. By forcing its flow back towards the fixed point, the system maintains a stable chaotic attractor with regions of superstable-periods.

The writhe of the attractor, as seen in the $x - y$ plane, changes as we follow the periodicity regions around the spiral, and we have one additional negative crossing of the attractor onto itself. Such a crossing is projection dependent, which is to say that when the attractor is viewed at different angles, it may not appear to be a crossing at all, and thus this wouldn't constitute the best possible means of defining the point of transition from one period to the next as we follow the spiral inwards. We do not currently have an invariant definition of where this transition occurs, but we can point to a narrow region where such a precise definition will be constrained to. It is clear that this transition happens near the topological transition line in codimension-2 control parameter space, but only below the center of the spiral hub. Thus the shrimp along this line, below the center of the spiral hub, differ qualitatively from those above this center point.

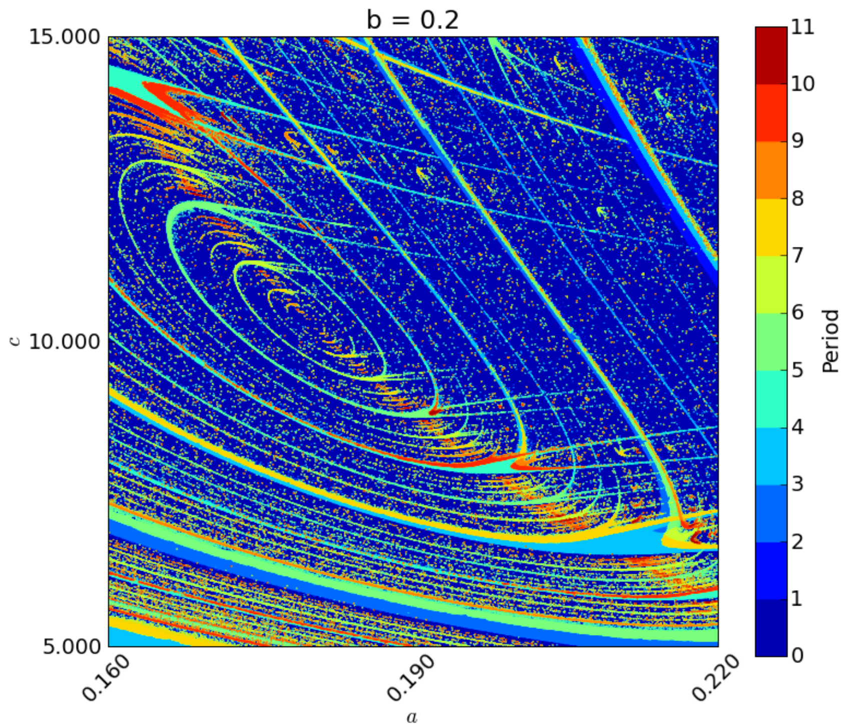

Figure 6.18: Section of codimension-2 parameter space for the Rössler attractor, with periodicity color-coded. The separtrix along which the attractor transitions from branch-2 and branch-3, and along which many shrimp line up, has some resemblance the α line in the codimension-2 parameter space of the bimodal normal form.

As we follow a superstable periodic orbit region around the central spiral hub from lower periodicity to higher periodicity (c.f. Figure 6.22), the angle of deposit rotates counter-clockwise around the fixed point. Like a long chain being deposited in a circular way on a flat surface, the number of turns of the chain on the flat surface increases as we follow the periodicity regions as they spiral in towards the center of the spiral hub. This is why each shrimp with period p along the transition line and above the center of the spiral hub is attached to the shrimp below the center of the hub which corresponds to a period of $p + 1$.

Now we must note that in the Logistic Map, there are, for example, three period-5 superstable orbits and two superstable period-4 orbits. It is not yet clear how these spiral transitions of $p \to p+1$ account for the fact that the number of orbits of period p generally differs from the number of orbits

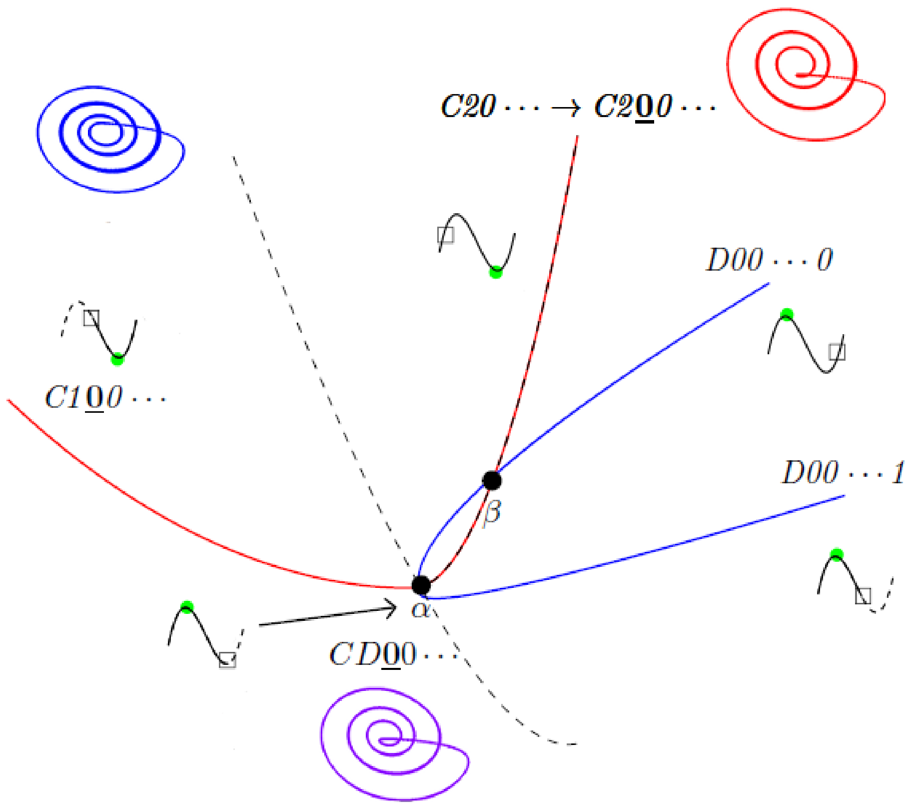

Figure 6.19: Anatomy of a generic "mutant shrimp" along the largest spiral. The symbolic string describing these orbits will be dominated by zeros. The center of the shrimp structure corresponds to a doubly-superstable orbit which includes both critical points. Each parabola corresponds to a variation of this orbit in which only one of the critical points is on the orbit. Due to the topological mechanism responsible for the periodicity transition, this shrimp has one tail which originates as a lower period and transitions to higher period before crossing TTL_3^2. Here, α is the head of the shrimp where we have a super-stable periodic orbit which includes both critical points of the bimodal map, and β is a region of overlap which is not a doubly-degenerate superstable orbit; two superstable orbits have alternating basins of attraction.

of period $p+1$ [36], but we do notice that the symbolics of these orbits help determine which variation of period p connects to which variation of $p+1$. Specifically, we must have that the same critical point, that associated with the unimodal map form on the branch-2 side of control parameter space, is part of the symbolic sequence along this spiral. This is due to the fact that the spiral region is continuous and crosses over the branch-2 side on the left. Thus if we give this critical point the symbol C, then we know that both connected periods p and $p+1$ will begin with symbol C. Furthermore, due to continuity, none of the points on the return map cross over the critical point, and so we know that the period-four orbit $C100$ must transition into an orbit $C1X00$ (though it

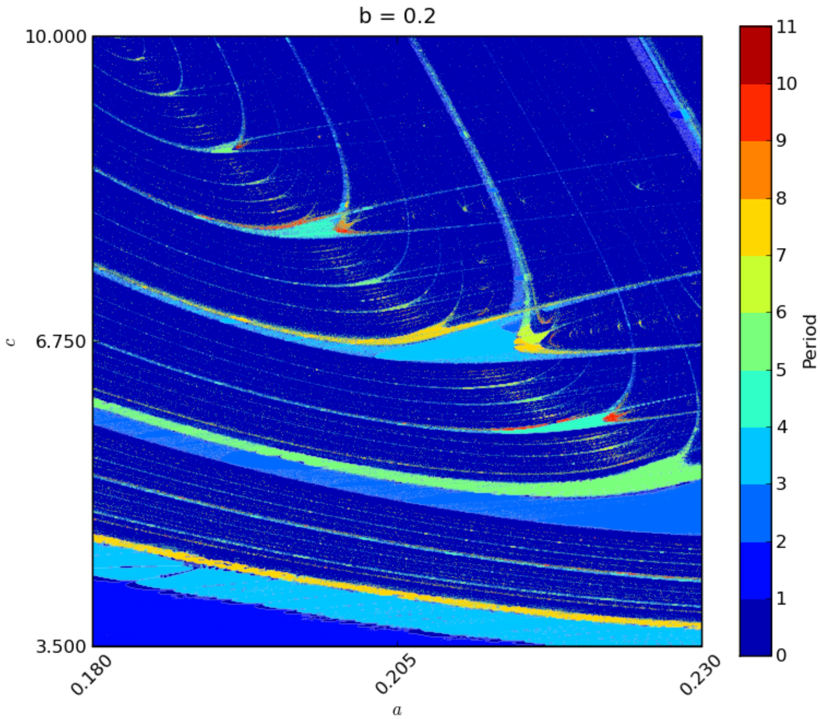

Figure 6.20: Section of codimension parameter space for the Rössler attractor, with periodicity color-coded. These shrimp are the "mutant" type, with one tail which doesn't match the other four.

becomes $C200$ inside the branch-3 region, the first two symbols transition back to $C1$ as they cross back over the second critical point at the lower shrimp), where X is either 0 or 1. However, since we know that the new branch is deposited on the inner region of the main plane of the attractor, this new symbol will be a 0, and so we have the transition from $C100 \rightarrow C1000$. We have traced the spiral for a number of orbits (Figure 6.28) which follow this general algorithm.

6.6 Open Questions

Having addressed a number of open questions, we close by noting that we have found new open questions in the course of our research. One open question, as stated previously, is the fact that though we have shown the mechanism by which one periodic orbit spirals into another, a mechanism

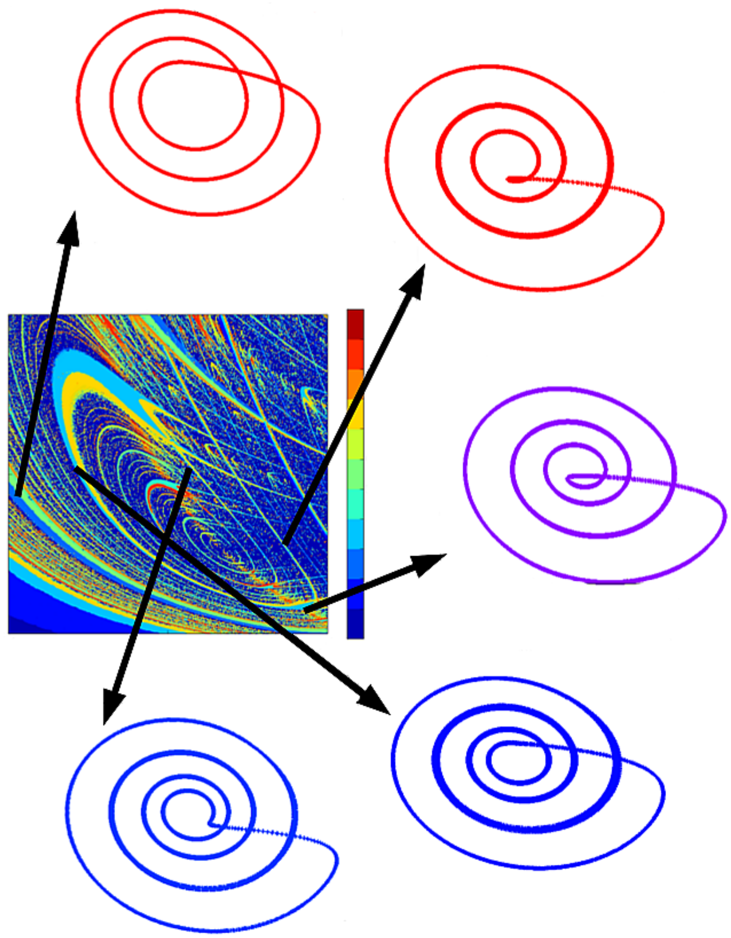

Figure 6.21: The spiral effect is a topological effect, and the "mutant" shrimp are the result of how the "tail" of the Rössler system lands on the attractor for different parameters.

which is continuous in the flow but discontinuous in the mapping, there remains the fact that there is not a one-to-one mapping of the number of periodic orbits of period p to those of period $p+1$ [36]. We suspect that the mapping of shrimp corresponding to each orbit of p to those corresponding to $p+1$ will be injective but not surjective, which is to say, each orbit of period $p > 2$ will transition to a period $p+1$, but there will remain unmatched period $p+1$ orbits. What does it mean for such orbits to be unmatched?

We additionally raise the open question of the striations apparent in the codimension-two parameter diagrams of the Rössler attractor. These striations can be seen in a number of graphs in the literature (see, for example, Barrio et al. [93]) but haven't been pointed out. In using an

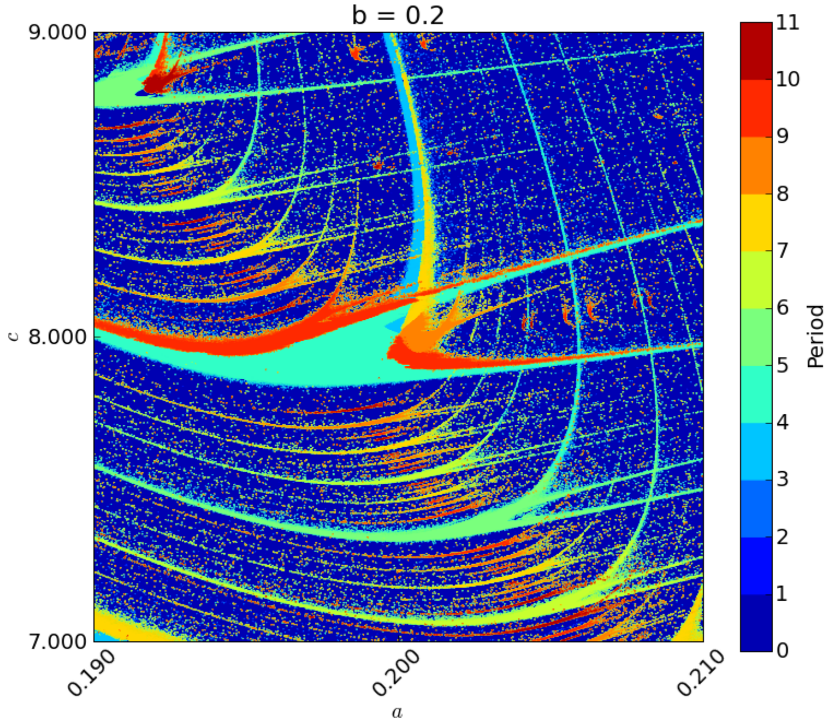

Figure 6.22: The spiral effect is a topological effect, and the "mutant" shrimp are the result of how the "tail" of the Rössler system lands on the attractor for different parameters. The smaller shrimp do not appear mutant on first glance, but that is due to their small size and the fact that nearby periods are identified by the color map as nearby colors. A closer inspection shows that they are indeed also mutant shrimp.

alternative technique to Lyapunov exponents mapping in order to outline chaos in codimension-2 parameter space, we found that these striations appeared with both methods (although slightly different in form for each) and are probably not likely to be numerical artifacts. We have also found that these striations appear consistent as the otherwise fixed parameter b is changed, that is, the striations change with varying b, but in a coordinated way that suggests they represent an unknown dynamical structure.

Figure 6.15 provides a clear example of these striations. The general shape of the striations suggests unanticipated dynamical behavior that seems well worth pursuing in further research.

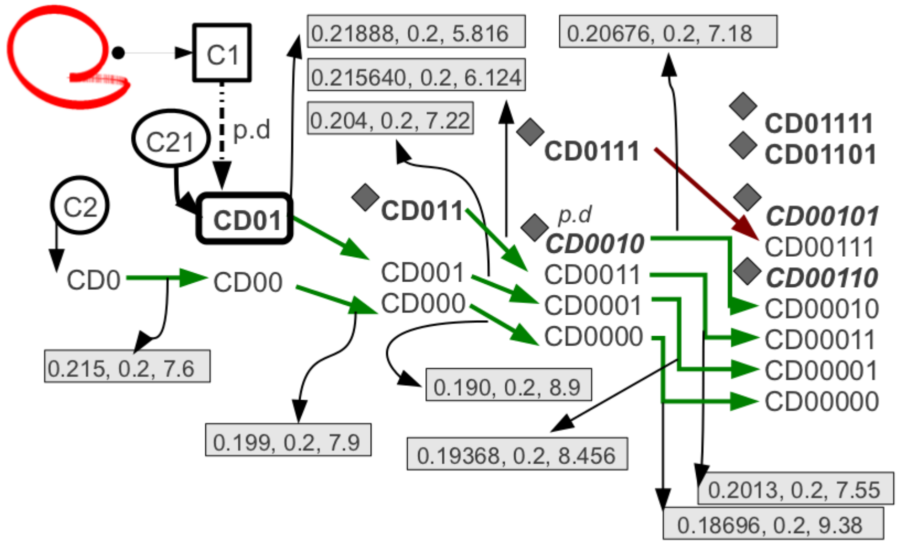

Figure 6.23: Symbol sequences in the nested spiral hub up to period seven. The orbits listed in each column are in the order that they appear in unimodal mappings [92]. Green arrows indicate orderings which have been matched both by looking at the structure in state space, and by matching the symbol sequence of the corresponding transitions in parameter space. The transition $CD0111 \rightarrow CD00111$ has only been confirmed by visually inspecting the attractor. Orbits in bold originate from isolated shrimp off of TTL_3^2 within the branch-3 side. The attached gray boxes indicate the approximate position of the corresponding mutant shrimp in parameter space.

6.7 Analysis of a Second System

Our next task is to demonstrate that this behavior is not unique to the Rössler system. Although the computational requirements for this analysis currently make it impractical to examine a multitude of strange attractors as we did in Chapter Three, we feel that the verification that this mechanism for periodicity transfer holds for another system will go far in providing confidence that this new mechanism helps us understand more than just one strange attractor.

Furthermore, we wish to show that this mechanism can be found in a system with direct experimental relevance. To that end, we chose to examine the model of a semiconductor lasers with optoelectronic feedback by Al-Naimee et al. [217]. This system is a topic of current research, as it has been claimed that this system represents a system with an incomplete homoclinic scenario (and thus non-Shilnikov) [197, 217]. Whether or not this is the case (we are not convinced), this system exhibits a periodicity hub that looks remarkably similar to that of the Rössler attractor.

This periodicity hub was first spotted in 2010 [197] in a Lyapunov phase diagram of the system, but just as with the Rössler system, the dynamical mechanisms responsible for this periodicity transition have not been investigated until now. Not only do we find that this system has the same periodicity transition mechanism, but we also find that this system helps us understand the results for the Rössler attractor since the shape of the hub is not as warped. Additionally, the mutant shrimp for this system are located above the central focus of the hub, rather than below as in the Rössler system, thus providing a very important differential between the two systems that may help us formulate this transition mechanism in more rigorous mathematical terms in the near future.

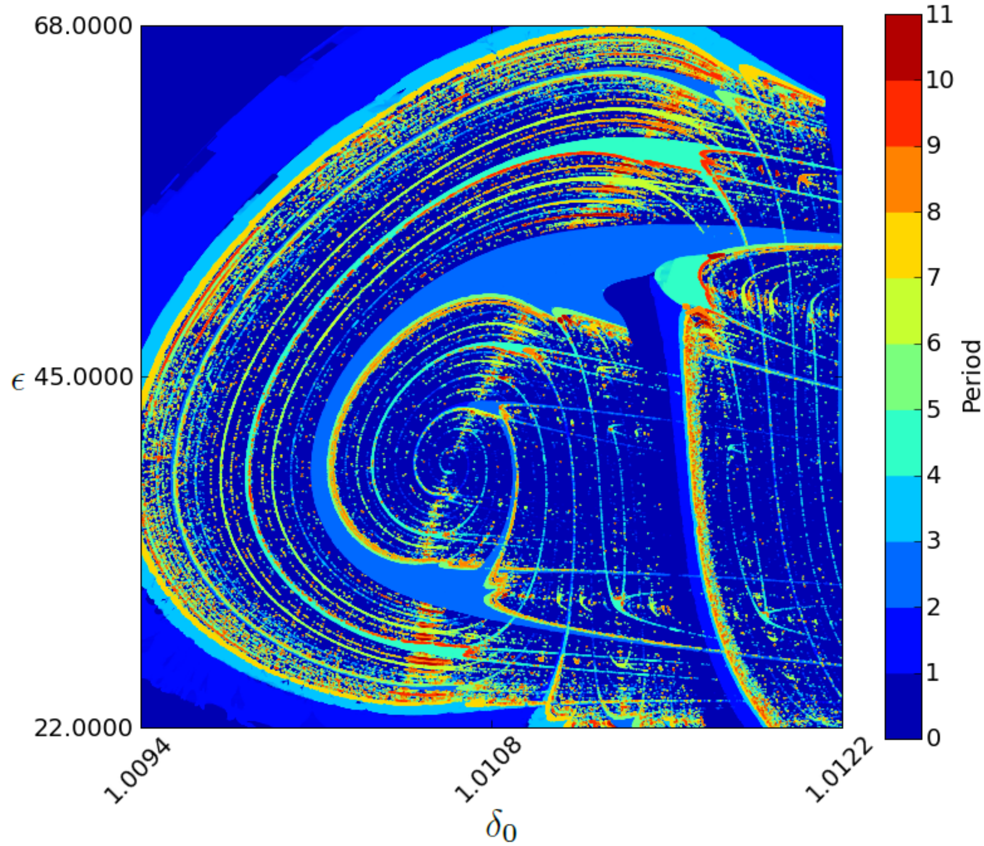

Figure 6.24: Periodicity diagram for a periodicity-transition hub for a semiconductor lasers with optoelectronic feedback. Due to resolution issues, the first period six orbit is aliased as a period three; all periods are confirmed visually by plotting the attractor before being used as data to formulate the periodicity sequence.

The Al-Naimee system is given as,

$$\overrightarrow{V}\begin{pmatrix}\dot{x}\\ \dot{y}\\ \dot{w}\end{pmatrix}=\overrightarrow{\Im}\begin{pmatrix}f_1\left(x,y,w\right)\\ f_2\left(x,y,w\right)\\ f_3\left(x,y,w\right)\end{pmatrix}=\begin{matrix}x(y-1)\\ \gamma\left(\delta_0-y+\alpha\frac{w+x}{1+s(w+x)}-xy\right)\\ -\epsilon\left(\omega+x\right)\end{matrix}\tag{6.12}$$

We select our parameter to mirror those used by Al-Naimee et al. [217]. The coefficient α corresponds to the photodetector responsivity and we set it equal to unity for our analysis, $\gamma = 0.001$ represents the ratio between population relaxation and photon damping rates, and $s = 11$ is the saturation coefficient of the amplifier. The two free parameters with which we will be concerned are ϵ, which is the high-pass frequency of the feedback loop, and δ_0 which is the solitary laser threshold. We plot the periodicity graph for this system in Figure 6.26.

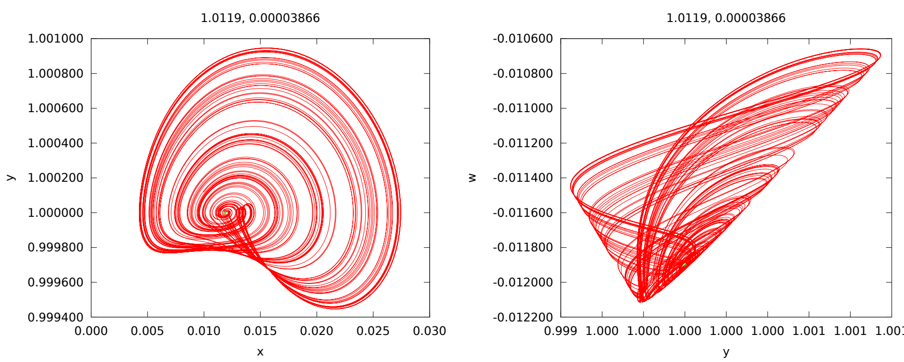

Figure 6.25: The attractor corresponding to the Al-Naimee et al. system (Equations 6.12 shown in xy (left) and yz projections for parameters given in text and $\delta_0 = 1.0119, \epsilon = 0.00003866$. The fixed point, located at $(\bar{x}, \bar{y}, \bar{z}) = (\delta_0 - 1, 1, 1 - \delta_0)$ is marked with a green dot.

The ordering of the periodicity transitions appears to match those of the Rössler system, up to our numerical resolution and established conjugacy (period seven, though three transitions to period seven are unconfirmed due to the fact that the Al-Naimee wraps very tightly around its fixed point and requires higher resolution numerical results). Having established the order of periodicity transfer from the Rössler system (Figure 6.28), we use it as a map to investigate the Al-Naimee system. We begin first with the period-two orbit that transitions into the major spiral (the spiral that begins with the period-three orbit). Regions with this period can be seen in Figure 6.26 as a near vertical line that juts upwards on the right side of the graph before transitioning to period three and wrapping around the center of the hub-like system.

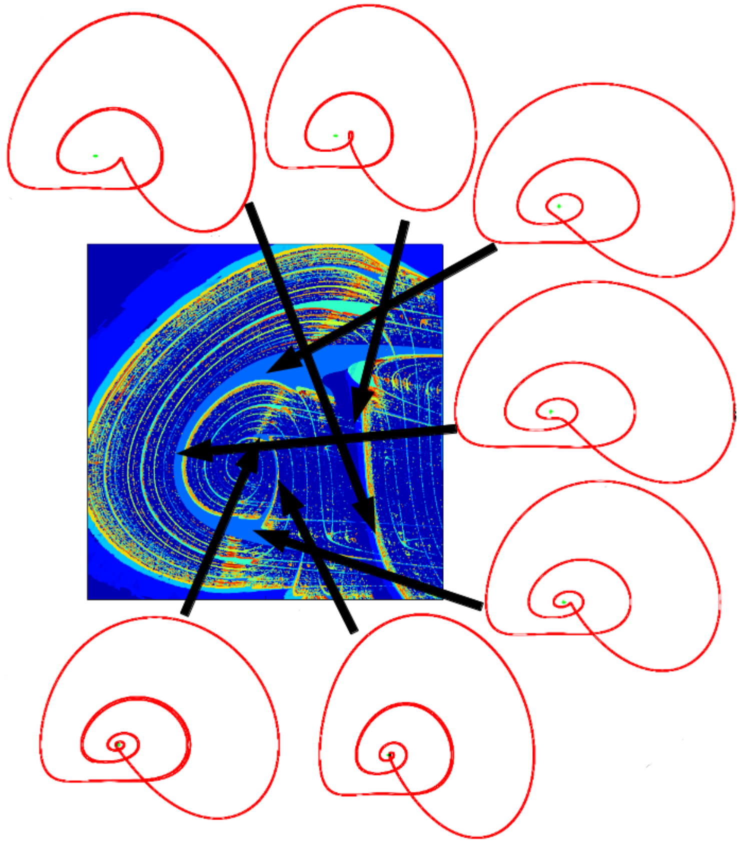

Figure 6.26: We follow the core of the primary periodicity transfer spiral from orbits $C1 \to C10 \to C100$. The area where the new layer is deposited on the main plane of the attractor rotates counter-clockwise as we circle the periodicity spiral counterclockwise. Note that this system has the opposite orientation of the Rössler system. The parameter values for each attractor are given, from top clockwise to bottom, as $1.0117, 0.000026$, $1.01155, 0.000037$, $1.01107, 0.000051$, $1.01011, 0.00004$, $1.01066, 0.000031$, $1.01089, 0.00003685$, and $1.01079, 0.00004301$.

This system has advantages over the Rössler system in regards to studying these special codimension-2 parameter structures. The hub in the Rössler system was highly skewed making it impractical to study the behavior of the hub above the primary period three shrimp. The Al-Naimee system, on the other hand, is remarkably well formed in parameter space, and all regions of interest are accessible. On the other hand, the Al-Naimee system wraps very tightly around its focal point at a much faster rate than the Rössler system does, which leads to occasional false positives. We visually inspect each result by plotting the corresponding attractor to avoid false positives. Another consequence of this tight wrapping is that the higher resolution mutant shrimp (period seven and above) are exceedingly difficult to locate compared with those in the Rössler system.

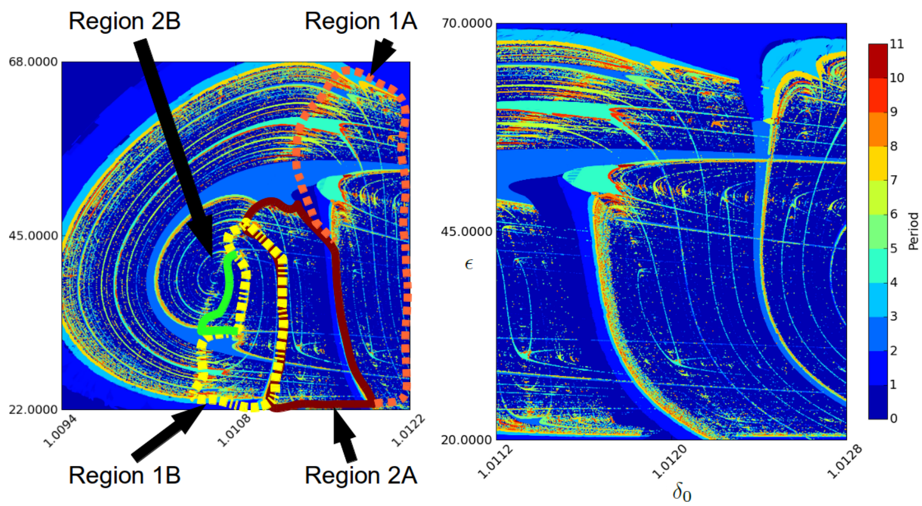

Figure 6.27: The spiral structure of the transitional hub can be partitioned into two primary spiral regions (left). These regions produce cohesive interlocking bands. Orbits in Region 1 correspond to the first periodic orbits in the Logistic Map sequence up until the period three orbit. Region 2 corresponds to the region between the period three orbit and the period four orbit with sequence $CD01$. All orbits that start in these regions do not begin as part of a spiral, but rather are the beginnings of new spirals (Regions 1B and Regions 2B). These orbits originate from more complicated dynamical reasons below $\epsilon < 0.000022$ or from shrimp which are not part of TTL_3^2. On the left, we show the partition area of Region 1A in more detail, where two periodic orbits divide this region; the latter orbit partitions the primary hub from the remainder of parameter space.

In Figure 6.27, we have outlined what are subsets of the two primary regions we have found which supply the spiral hub with periodic orbits. These regions produce cohesive interlocking bands. Orbits in Region 1 correspond to the first periodic orbits in the Logistic Map sequence up until the period three orbit. Region 2 corresponds to the region between the period three orbit and the period four orbit with sequence $CD01$. All orbits that start in these regions to not begin as part of a spiral, but rather are the beginnings of new spirals (Regions 1B and Regions 2B). These orbits originate from more complicated dynamical reasons below $\epsilon < 0.000022$ or from shrimp which are not part of TTL_3^2.

We also find in Figure 6.27 that the primary spiral hub for this system is distinctly partitioned from the remainder of the region of interesting dynamics in codimension-2 space. A periodic orbit that originates away from the primary hub and connects to the period-two orbit that rings the hub is the boundary between these regions.

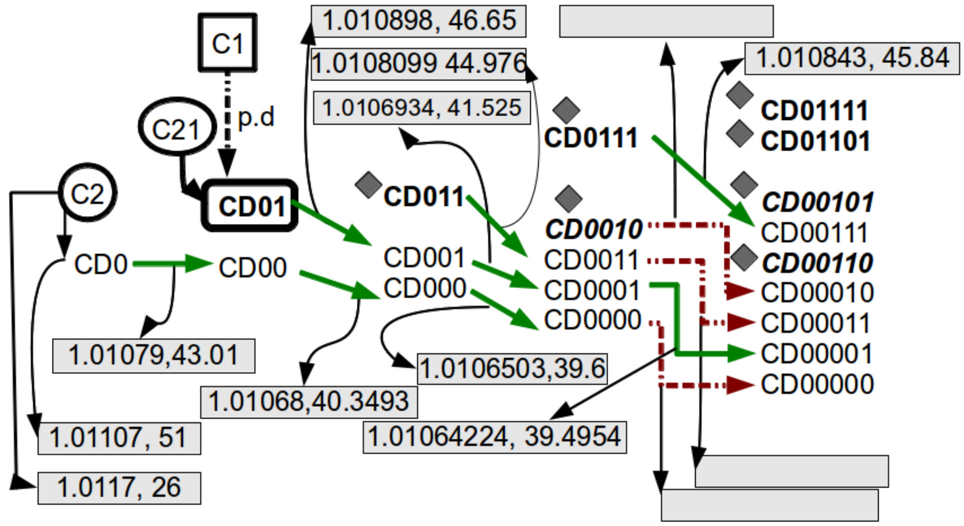

Figure 6.28: Visually matched symbol sequences in the spiral hub and predicted spiral patterns up to period seven for the Al-Naimee system. The orbits listed are those that appear in unimodal mappings, for period up to seven. The orbits are listed in column form in the order of their appearance in the Logistic Map [36]. The arrows indicate one periodic orbit spiraling into another through the mechanism of flow deposit back on to the main plane in the Al-Naimee system. Green (solid arrows) the approximate centers of mutant shrimp corresponding to the transitions have been located, with parameter values δ_0, ϵ given in connected gray boxes (ϵ values are given in units of 10^{-6}). Red (dashed) arrows indicated suspected transitions which need to be confirmed: the Al-Naimee system wraps much more tightly around its fixed points and so resolution issues arise for higher periods.

6.8 Conclusions

We have examined in great detail the spiral hub seen in the Rössler codimension-2 parameter plane. We have shown that the dynamical mechanism responsible for this hub is the dynamics of unimodal and bimodal mappings. For the first time, we have isolated the points at which the “shrimp” tails change periods as they spiral inwards to the focal point of the hub, and we have outlined the dynamical mechanism which causes the transitional line between branch-2 and branch-3 manifolds to be populated by a string of shrimp. For the first time, we have pointed out that the shrimp below the focal point are “mutant”, and we have explained this as being the result of the fact that the Rössler system deposits flow from its tail onto the main plane of the attractor at different angles relative to the fixed point. We have shown that these angles are dependent upon the control parameters of the attractor. The writhe of the attractor, as seen in the $x - y$ plane, changes as we follow the periodicity regions around the spiral, resulting in the addition of a negative crossing of the attractor onto itself as we change control parameters. As we follow a superstable periodic orbit region around the central spiral hub from lower periodicity to higher periodicity, the angle of deposit rotates counter-clockwise around the fixed point. Like a long chain being deposited in a circular way on a flat surface, the number of turns of the chain on the flat surface increases as we follow the periodicity regions as they spiral in towards the center of the spiral hub. There remains uncertainty as to what point in this depositing we transition from period p to period $p + 1$ since this point may vary depending on which Poincaré section is taken, and an open question remains about whether or not there exists a Poincaré section that might work for all parameter values, in which case the precise location of transition from one period to the next can be defined as a sort of "branch-cut" similar to those used in complex analysis [218]. However, it is clear that this transition happens near the topological transition line in codimension-2 control parameter space, but only below the center of the spiral hub. Thus the shrimp along this line, below the center of the spiral hub, differ qualitatively from those above this center point. This phenomenon has no equivalent in mappings.

We followed up these findings by applying this analysis to a second system, a strange attractor which is a direct model for a physical laser. The results from this system matched those for the Rössler attractor.

Chapter 7: Conclusions

The study of nonlinear dynamics is nowhere near conclusion, as each step made towards better understanding nonlinear systems often raises far more questions than it answers. This thesis has approached two main research topics in an attempt to gain a better understanding of the global features of strange attractors.

The first topic regarded the shape of strange attractors, and we have shown that there are dynamical means by which one might ascertain the overall structure of a strange attractor. We believe that this research has brought us a step closer to understanding how the dynamics that define a strange attractor also define its shape.

The second question was a much more ambitious one. We wished to provide a topological and dynamical explanation for some of the features we find in the phase space analysis of the Rössler attractor. In particular, we focused on the primary spiral hub found in the the parameter space of the Rössler system. We have found the mechanism that leads to these spirals, locating it in the state-space behavior of the attractor as we circle around the center of the spiral hub in phase space. We followed this with an analysis of a second system, which describes an experimental laser system. We found that this system also had a primary spiral hub, and that the mechanism for periodicity transition and the organization of shrimp structures, as well as the symbolic ordering of orbits along the periodicity spiral, all matched those of the Rössler system. This suggests that our findings will likely extend to many other systems which are yet to be explored.

While this thesis may seem bimodal, in that the core parts of it represent avenues of research which aren't directly related, we believe that this work has taken a step in the right direction in order to gain a better grasp of the global organization of strange attractors. When one looks upon the multitude of strange attractors, one can't help but ask, why do they have such a diverse set of shapes? We have shown that the shape of the attractor can be outlined via analytical dynamical means. In other words, the shapes of the attractors are baked into the dynamical equations that define them, and we have found a way to extract a sort of skeletal structure from these equations. While researching this topic, we could not help but notice that these attractors can vary dramatically with a change in parameters, transitioning suddenly from chaos to a stable period and then back again. This seems quite random on a superficial level, but one can not help but ask, is there a global organization to these transitional regions between chaos and stability? In recent years, the answer to this question has been found to be a resounding yes. The discovery of the spiral hubs and periodicity transitions was a welcome surprise, but in science, a surprise is only welcome for a short period before it becomes an itch to be scratched. The open question remained as to why the parameter space was organized in such an unexpectedly ordered way. This thesis has taken an important step in answering that question. Of course, we have not come close to closing the book on research of these global patterns, but we have better set the stage by identifying a new key mechanism, and by refining the set of open questions to a more specific subset which may help future researchers as they explore the n-modal regions that lie ahead.

Finally, our work can be seen as a reminder to experimentalist exploring chaotic systems that return-maps should be used with great care. Return-maps are one of the most commonly used tools in the chaos tool-box, but as we have shown here, they do not always provide a true picture of the dynamics of strange attractors. We have shown where, and how, they lose verisimilitude with the dynamics of the system.

Bibliography

[1] Brian R Hunt and James A Yorke. Maxwell on Chaos. Nonlinear Science Today, 3(1), 1993.

[2] B Hao. Chaos. World Scientific, 1984. ISBN 9789971966508.

[3] H. Poincar´e. Sur le problème des trois corps et les équations de la dynamique. Divergence des séries de M. Lindstedt. Acta Mathematica, 13:1–270, 1890.

[4] S H Strogatz. Nonlinear dynamics and chaos: with applications to physics,biology, chemistry, and engineering. Studies in nonlinearity. Westview Press, 1994. ISBN 9780738204536.

[5] Jacques Hadamard. Les surfaces a courbures opposees et leurs lignes geodesique. J. Math. Pures Appl., 4:27–73, 1898.

[6] S Velichov. Nonlinear Dynamics and Chaos with Applications to Hydrodynamics and Hydrological Modelling. Taylor and Francis, 2004. ISBN 9789058096913.

[7] D A Lind and B Marcus. An introduction to symbolic dynamics and coding. Cambridge University Press, 1995. ISBN 9780521559003.

[8] D Ruelle. Chaotic evolution and strange attractors: the statistical analysis of time series for deterministic nonlinear systems. Lezioni lincee. Cambridge University Press, 1989. ISBN 9780521368308.

[9] Susan G Williams. Introduction to Symbolic Dynamics. In Proceedings of Symposia in Applied Mathematics: Symbolic Dynamics and its Applications, volume 60, pages 1–11, 2002.

[10] B Kitchens. Symbolic dynamics: one-sided, two-sided, and countable state Markov shifts. Universitext (1979). Springer, 1998. ISBN 9783540627388.

[11] B van der Pol and J van der Mark. Frequency Demultiplication. Nature, 120:363–364, September 1927. doi: 10.1038/120363a0.

[12] B. van der Pol. The nonlinear theory of electric oscillations. Proc. INst. Radio Eng., 22: 1051–1086, 1934.

[13] S.L. McMurran and J.J. Tattersall. The mathematical collaboration of ML Cartwright and JE Littlewood. The American mathematical monthly, 103(10):833–845, 1996.

[14] Shawnee Mcmurran and James Tattersall. Mary Cartwright (1900–1998). Notices of the AMS, 46(2), 1998.

[15] S Lefschetz and M L Cartwright. Contributions to the theory of nonlinear oscillations. Number v. 2 in Annals of Mathematics Studies. Princeton University Press, 1952. ISBN 9780691095813.

[16] ML Cartwright and J.E. Littlewood. On Non-Linear Differential Equations of the Second Order II. Annals of Mathematics, 48(2), 1947.

[17] E.N. Lorenz. Deterministic Nonperiodic Flow. Atmos J Sci, 20:130–141, 1963.

[18] J Gleick. Chaos: making a new science. A Penguin book. Penguin, 1988. ISBN 9780140092509.

[19] David Ruelle and Floris Takens. On the nature of turbulence. Communications in Mathematical Physics, 20:167–192, September 1971. ISSN 0010-3616. doi: 10.1007/BF01646553.

[20] Floris Takens. detecting strange attractors in turbulence, pages 366–381. Springer-Verlag, New York, NY, 1981.

[21] Nicola Romanazzi, Marc Lefranc, and Robert Gilmore. Embeddings of low-dimensional strange attractors: Topological invariants and degrees of freedom. Physical Review E, 75(6):1–9, June 2007. ISSN 1539-3755. doi: 10.1103/PhysRevE.75.066214.

[22] Daniel J Cross and R Gilmore. Representation theory for strange attractors. Physical review. E, Statistical, nonlinear, and soft matter physics, 80(5 Pt 2):56207, November 2009. ISSN 1550-2376.

[23] William Parry. Intrinsic markov chains. Trans. Amer. Math. Soc, 112(1):55–65, 1964.

[24] William Parry. Symbolic dynamics and transformations of the unit interval. Trans. Amer. Math. Soc, 122(6):368–378, 1966.

[25] A.N. Sharkovsky. On the periodic solutions of a class of finite differences equations. In Proceedings of the Fourth conference on nonlinear oscillations, page 249. Academia, CSAV, 1968.

[26] A.N. Sharkovsky. On cycles and the structure of a continuous mapping. Ukrainian Math. J., 17(3):104–111, 1965.

[27] A.N. Sharkovsky. Coexistence of cycles of continuous mapping of the line into itself. Ukrainian Math. J., 16:61–71, 1964.

[28] A.N. Sharkovsky. The reducibility of a continuous function of a real variable and the structure of the fixed points of the corresponding iteration process. Dokl. Akad. Nauk SSSR, 139(5): 1067–1070, 1961.

[29] T.Y. Li and J.A. Yorke. Period three implies chaos. The American Mathematical Monthly, 82(10):985–992, 1975.

[30] N Metropolis and ML Stein. On finite limit sets for transformations on the unit interval. Journal of Combinatorial Theory,, 15(1):25–44, July 1973. ISSN 00973165. doi: 10.1016/0097-3165(73)90033-2.

[31] John Milnor and William Thurston. On Iterated Maps of the Interval. In Lecture Notes in Mathematics, page 465. 1988.

[32] R.M. May. Simple mathematical models with very complicated dynamics. Nature, 261(5560): 459–467, 1976.

[33] MJ Feigenbaum. Quantitative universality for a class of nonlinear transformations. Journal of statistical physics, (1), 1978.

[34] Stephen Smale. Differentiable dynamical systems. Bulletin of the American Mathematical Society, 73:747–817, July 1967. ISSN 0273-0979.

[35] Robert L. Devaney. An Introduction to Chaotic Dynamical Systems. Westview Press, 2nd edition, 2003.

[36] R Gilmore and M Lefranc. The Topology of Chaos: Alice in Stretch and Squeezeland. John Wiley & Sons, Limited, 2002. ISBN 9783527410675.

[37] S Sternberg. Dynamical Systems. Dover Books on Mathematics. Dover Publications, 2010. ISBN 9780486477053.

[38] Michel Vellekoop and Raoul Berglund. On Intervals, Transitivity = Chaos. The american mathematical monthly, 101(4):353–355, April 1994. ISSN 00029890. doi: 10.2307/2975629.

[39] Carsten Knudsen. Chaos Without Nonperiodicity. The American Mathematical Monthly, 101 (6):563, June 1994. ISSN 00029890. doi: 10.2307/2975324.

[40] J Frø yland. Introduction to chaos and coherence. Institute of Physics Publishing, 1992. ISBN 9780750301954.

[41] T Tél and M Gruiz. Chaotic dynamics: an introduction based on classical mechanics. Cambridge University Press, 2006. ISBN 9780521547833.

[42] O Rössler. An equation for continuous chaos. Physics Letters A, 57(5):397–398, July 1976. ISSN 03759601. doi: 10.1016/0375-9601(76)90101-8.

[43] Thomas Malthus. An Essay on the Principle of Population. St. Paul's Church-Yard, London, May 1798. doi: 10.2307/2064821.

[44] Cèsar Bordehore, Angela Pascual, Maria J. Pujol, Julio Escolano, Inmaculada Manchón, and Pedro Grimalt. Study and modelling of a density dependent population using faltung (closed cycle type) equations. International Journal of Numerical Methods for Heat & Fluid Flow, 13 (4):486–499, 2003. ISSN 0961-5539. doi: 10.1108/09615530310475920.

[45] Pierre-François Verhulst. Notice sur la loi que la population poursuit dans son accroissement. Number v. 10. Impr. d'H. Vandekerckhove, 1838.

[46] M Ausloos and M Dirickx. The logistic map and the route to chaos: from the beginnings to modern applications. Springer complexity. Springer, 2006. ISBN 9783540283669.

[47] Alfred J Lotka. Contribution to the Theory of Periodic Reactions. The Journal of Physical Chemistry, 14(3):271–274, January 1910. doi: 10.1021/j150111a004.

[48] A.J. Lotka. Elements of physical biology. Williams & Wilkins company, 1925.

[49] R. Pearl and L.J. Reed. On the rate of growth of the population of the United States since 1790 and its mathematical representation. Proceedings of the National Academy of Sciences of the United States of America, 6(6):275, 1920.

[50] H.S. Pritchett. A formula for predicting the population of the United States. Publications of the American Statistical Association, 2(14):278–286, 1891.

[51] J. Régnier and S. Lambin. Etude d'un cas d'antagonisme microbien (Bacillus Coli-Staphyloccoccus aureus). Comptes Rendus de l'Académie des Sciences de Paris, 199:1682–1683, 1934.

[52] V. Volterra. Remarques sur la note de M. Regnier et Mlle. Lambin (Etude d'un cas d'antagonism microbien). Compt. Rend. Acad. Sci., 199:1684–1686, 1934.

[53] V A Kostitzin. Biologie math{é}matique. Collection Armand Colin. Librairie Armand Colin, 1937.

[54] R Pearl, O M Pepper, and F J Hagle. Variation and differentiation in Ceratophyllum. Carnegie Institution of Washington publication. Carnegie Institution of Washington, 1907.

[55] H.H. Donaldson. A comparison of the albino rat with man in respect to the growth of the brain and of the spinal cord. Journal of Comparative Neurology and Psychology, 18(4):345–392, October 1908. ISSN 0092-7015. doi: 10.1002/cne.920180402.

[56] The World at Six Billion, 1999. Technical report, United Nations Department of Economic and Social Affairs, Population Division, 1999.

[57] P Collet and J P Eckmann. Iterated Maps on the Interval as Dynamical Systems. Birkh{ä}user, Boston, 1980. ISBN 978-0817630263.

[58] R. Aurich, M Sieber, and F. Steiner. Quantum chaos of the Hadamard-Gutzwiller model. Physical review letters, 61(5):483–487, 1988.

[59] R Aurich and F Steiner. Orbit sum rules for the quantum wave functions of the strongly chaotic Hadamard billiard in arbitrary dimensions. Foundations of Physics, 31(4):569–592, 2001.

[60] M Morse and G Hedlund. Symbolic dynamics. American Journal of Mathematics, 60:815–866, 1938.

[61] M Morse and G Hedlund. Symbolic dynamics II. Sturmian trajectories. American Journal of Mathematics, 62(1):1–42, 1940.

[62] R Bowen and J R Chazottes. Equilibrium states and the ergodic theory of Anosov diffeomorphisms. Lecture notes in mathematics. Springer, 2008. ISBN 9783540776055.

[63] R Bowen and D Ruelle. Ergodic Theory of Axiom-A. Inventiones Mathematicas, 29:181, 1975.

[64] Y Sinai. Gibbsian Measures in Ergodic Theory. Russian Mathematical Surveys, 27:21, 1972.

[65] JP Crutchfield and NH Packard. Symbolic dynamics of one-dimensional maps: Entropies, finite precision, and noise. International Journal of Theoretical Physics, 21(6):433–466, 1982.

[66] R S Shaw. On the predictability of mechanical systems. Thesis, University of California, 1980.

[67] W E Boyce and R C DiPrima. Elementary differential equations and boundary value problems. Wiley, 1969.

[68] D. M. Grobman. Homeomorphisms of systems of differential equations. Doklady Akademii Nauk SSSR, 128:880–881, 1959.

[69] P. Hartman. A lemma in the theory of structural stability of differential equations. Proc. Amer. Math. Soc, 11(4):610–620, 1960.

[70] A.M Lyapunov. The General Problem of the Stability of Motion (In Russian). PhD thesis, 1892.

[71] J E Marsden and M McCracken. The Hopf bifurcation and its applications. Applied mathematical sciences. Springer-Verlag, 1976. ISBN 9780387902005.

[72] A. A. Andronov and A.A. Witt. Sur la théorie mathématiques des autooscillations. C. R. Acad. Sci. Paris, 190:256–258, 1930.

[73] Nicholas D. Kazarinoff. Review: J. E. Marsden and M. McCracken, The Hopf bifurcation and its applications. Bulletin of the American Mathematical Society, 83(5):998–1004, 1977.

[74] E. Hopf. Abzweigung einer periodischen Lösung eines Differentialsystems. Akad. Wiss. Leipzig, 94:1–22, 1942.

[75] An introduction to symbolic dynamics and coding, volume 0000. Cambridge Univ Pr.

[76] H. Poincaré. Les Méthodes nouvelles de la Mécanique Céleste. Gauthier-Villars, Paris, 1892.

[77] Ernest W. Brown. Poincaré's Mécanique Céleste. Bull. New York Math. Soc., I(9):206–214, 1892.

[78] K T Alligood, T Sauer, and J A Yorke. Chaos: an introduction to dynamical systems. Textbooks in mathematical sciences. Springer, 1997. ISBN 9780387946771.

[79] R Genesio, G Innocenti, and F Gualdani. A global qualitative view of bifurcations and dynamics in the Rössler system. Physics Letters A, 372(11):1799–1809, March 2008. ISSN 03759601. doi: 10.1016/j.physleta.2007.10.063.

[80] C. Letellier, P. Dutertre, and B. Maheu. Unstable periodic orbits and templates of the Rossler system: Toward a systematic topological characterization. Chaos (Woodbury, N.Y.), 5(1): 271–282, March 1995. ISSN 1089-7682. doi: 10.1063/1.166076.

[81] S Wiggins. Introduction to applied nonlinear dynamical systems and chaos. Texts in applied mathematics. Springer, 2003. ISBN 9780387001777.

[82] TR Chay. Chaos in a three-variable model of an excitable cell. Physica D: Nonlinear Phenomena, pages 233–242, 1985.

[83] G Medvedev. Reduction of a model of an excitable cell to a one-dimensional map. Physica D: Nonlinear Phenomena, 202(1-2):37–59, March 2005. ISSN 01672789. doi: 10.1016/j.physd.2005.01.021.

[84] E M Izhikevich. Dynamical systems in neuroscience: the geometry of excitability and bursting. Computational neuroscience. MIT Press, 2007. ISBN 9780262090438.

[85] Willy Govaerts, Yuri a. Kuznetsov, and Annick Dhooge. Numerical Continuation of Bifurcations of Limit Cycles in MATLAB. SIAM Journal on Scientific Computing, 27(1):231, 2005. ISSN 10648275. doi: 10.1137/030600746.

[86] P Gaspard and G Nicolis. What can we learn from homoclinic orbits in chaotic dynamics? Journal of Statistical Physics, 31(3):499–518. ISSN 0022-4715. doi: 10.1007/BF01019496.

[87] T.D. Tsankov and R Gilmore. Strange attractors are classified by bounding tori. Physical review letters, 91(13):134104, 2003.

[88] G Byrne, R Gilmore, and C Letellier. Distinguishing between folding and tearing mechanisms in strange attractors. Physical Review E, 70(5):56214, 2004.

[89] C Sparrow. The Lorenz equations: bifurcations, chaos, and strange attractors. Applied mathematical sciences. Springer-Verlag, 1982. ISBN 9780387907758.

[90] B L Hao. Elementary symbolic dynamics and chaos in dissipative systems. World Scientific, 1989. ISBN 9789971506988.

[91] Benjamin Coy. Dimension Reduction for Analysis of Unstable Periodic Orbits Using Locally Linear Embedding. International Journal of Bifurcation and Chaos, 22(1), 2012.

[92] Robert Gilmore. Topological analysis of chaotic dynamical systems. Reviews of Modern Physics, 70(4):1455–1529, October 1998. ISSN 0034-6861. doi: 10.1103/RevModPhys.70.1455.

[93] Roberto Barrio, Fernando Blesa, and Sergio Serrano. Qualitative analysis of the Rössler equations: Bifurcations of limit cycles and chaotic attractors. Physica D: Nonlinear Phenomena, 238(13):1087–1100, June 2009. ISSN 01672789. doi: 10.1016/j.physd.2009.03.010.

[94] Timothy D. Jones. Topological origins of a bi-parameter periodicity hub for the Rössler attractor. TBA, 2012.

[95] G B Mindlin, H G Solari, M A Natiello, R Gilmore, and X J Hou. Topological analysis of chaotic time series data from the Belousov-Zhabotinskii reaction. Journal of Nonlinear Science, 1:147–173, 1991.

[96] NB Tufillaro, R Holzner, L Flepp, E Brun, and M Finardi. Template analysis for a chaotic NMR laser. Physical Review A, 44(8):4786–4788, 1991.

[97] F Papoff, A Fioretti, E Arimondo, and GB Mindlin. Structure of chaos in the laser with saturable absorber. Physical review letters, 68(8), 1992.

[98] M Lefranc and P Glorieux. Topological analysis of chaotic signals from a CO2 laser with modulated losses. Int. J. Bifurcation Chaos Appl. Sci. Eng., 3:643–649, 1993.

[99] Javier Used and Juan Carlos Martin. Multiple topological structures of chaotic attractors ruling the emission of a driven laser. Physical Review E, 82:016218, 2010. doi: 10.1103/PhysRevE.82.016218.

[100] C. Letellier, L Le Sceller, and P. Dutertre. Topological characterization and global vector field reconstruction of an experimental electrochemical system. The Journal of, 99(18):7016–7027, May 1995. ISSN 0022-3654. doi: 10.1021/j100018a039.

[101] NB Tufillaro, Peter Wyckoff, Reggie Brown, and Thomas Schreiber. Topological time-series analysis of a string experiment and its synchronized model. Physical Review E, 51(1):164–174, 1995.

[102] C. Letellier, G. Gouesbet, F. Soufi, J. R. Buchler, and Z. Kollath. Chaos in variable stars: Topological analysis of W Vir model pulsations. Chaos (Woodbury, N.Y.), 6(3):466–476, September 1996. ISSN 1089-7682. doi: 10.1063/1.166189.

[103] H Haken. At least one Lyapunov exponent vanishes if the trajectory of an attractor does not contain a fixed point. Physics Letters A, 94(February):71–72, 1983.

[104] Alan Wolf, J.B. Swift, H.L. Swinney, and J.A. Vastano. Determining Lyapunov exponents from a time series. Physica D: Nonlinear Phenomena, 16(3):285–317, 1985.

[105] MT Rosenstein and JJ Collins. A practical method for calculating largest Lyapunov exponents from small data sets. Physica D: Nonlinear, (617), 1993.

[106] Till Tantau. The TikZ and PGF Packages: Manual for version 2.00.

[107] Luca Dieci, Michael S. Jolly, and Erik S. Van Vleck. Numerical Techniques for Approximating Lyapunov Exponents and Their Implementation. Journal of Computational and Nonlinear Dynamics, 6(1):011003, 2011. ISSN 15551423. doi: 10.1115/1.4002088.

[108] A.L. Hodgkin and A.F. Huxley. A quantitative description of membrane current and its application to conduction and excitation in nerve. The Journal of physiology, 117(4):500, 1952.

[109] Kazuyuki Aihara and Gen Matsumoto. Temporally coherent organization and instabilities in squid giant axons. Journal of Theoretical Biology, 95(4):697–720, 1982. ISSN 0022-5193. doi: 10.1016/0022-5193(82)90349-6.

[110] Control of chaos in networks with delay: A model for synchronization of cortical tissue. Neural Computation, 1154:1141–1154, 1994.

[111] C Grebogi and J A Yorke. The impact of chaos on science and society. United Nations University Press, 1997. ISBN 9789280808827.

[112] Kazuyuki Aihara. Chaos Engineering and Its Application to Parallel Distributed Processing With Chaotic Neural Networks. Proceedings of the IEEE, 90(5):919–930, 2002.

[113] P Dayan and L F Abbott. Theoretical neuroscience: computational and mathematical modeling of neural systems. Computational neuroscience. MIT Press, 2005. ISBN 9780262541855.

[114] V S Anishchenko. Nonlinear dynamics of chaotic and stochastic systems: tutorial and modern developments. Number v. 10 in Springer complexity. Springer, 2007. ISBN 9783540381648.

[115] H G Schuster and W Just. Deterministic chaos: an introduction. Wiley-VCH, 2005. ISBN 9783527404155.

[116] S Sastry. Nonlinear systems: analysis, stability, and control. Interdisciplinary applied mathematics: Systems and control. Springer, 1999. ISBN 9780387985138.

[117] L P Shilnikov. Methods of qualitative theory in nonlinear dynamics. Number pt. 2 in World scientific series on nonlinear science: Monographs and treatises. World Scientific, 2001. ISBN 9789810240721.

[118] L P Shilnikov, Andrey L Shilnikov, and L O Chua. Methods of qualitative theory in nonlinear dynamics. World scientific series on nonlinear science: Monographs and treatises. World Scientific, 1998. ISBN 9789810233822.

[119] S. Smale. Chaos: Finding a Horseshoe on the Beaches of Rio. Mathematical Intelligencer, 20: 39–44, 1998.

[120] H.~J. Lugt. The dilemma of defining a vortex, pages 309–321. 1979.

[121] Eric D. Siggia. Numerical study of small-scale intermittency in three-dimensional turbulence. Journal of Fluid Mechanics, 107:375–406, April 1981. ISSN 0022-1120. doi: 10.1017/S002211208100181X.

[122] R A Kerr. Higher-order derivative correlations and the alignment of small-scale structures in isotropic numerical turbulence. 1983.

[123] H J Lugt. Vortex flow in nature and technology. A Wiley-Interscience publication. Wiley, 1983.

[124] R.~W. Metcalfe, S Menon, and A.~K.~M.~F. Hussain. Coherent structures in a turbulent mixing layer - A comparison between direct numerical simulations and experiments. In 5th Symposium on Turbulent Shear Flows, pages 4.13–4.19, 1985.

[125] A K M Fazle Hussain and M Hayakawa. Eduction of large-scale organized structures in a turbulent plane wake. Journal of Fluid Mechanics, 180:193–229, 1987. doi: 10.1017/S0022112087001782.

[126] J.~C.~R. Hunt, A.~A. Wray, and P Moin. Eddies, streams, and convergence zones in turbulent flows. In Studying Turbulence Using Numerical Simulation Databases, 2, pages 193–208, December 1988.

[127] Y. Levy, D. Degani, and A. Seginer. Graphical visualization of vortical flows by means of helicity. AIAA journal, 28(8):1347–1352, 1990.

[128] Zhen-Su She, Eric Jackson, and Steven A. Orszag. Intermittent vortex structures in homogeneous isotropic turbulence. Nature, 344:226–228, 1990. doi: doi:10.1038/344226a0.

[129] D K Bisset, R A Antonia, and L W B Browne. Spatial organization of large structures in the turbulent far wake of a cylinder. Journal of Fluid Mechanics, 218:439–461, 1990. doi: 10.1017/S0022112090001069.

[130] A. Globus, C. Levit, and T. Lasinski. A tool for visualizing the topology of three-dimensional vector fields. IEEE Visualization Proceedings, pages 33–40, October 1991.

[131] John Villasenor and Alain Vincent. An algorithm for space recognition and time tracking of vorticity tubes in turbulence. CVGIP: Image Underst., 55(1):27–35, January 1992. ISSN 1049-9660. doi: 10.1016/1049-9660(92)90004-M.

[132] J. Jeong and F. Hussain. On the identification of a vortex. Journal of Fluid Mechanics, 285 (1):69–94, 1995.

[133] D.C. Banks and B.A. Singer. A predictor-corrector technique for visualizing unsteady flow. Visualization and Computer Graphics, IEEE Transactions on, 1(2):151–163, 1995.

[134] Robert Sujudi, David and Haimes. Identification of swirling flow in 3D vector fields. AIAA Paper, 95(AIAA Paper 95–1715):1–8, 1995.

[135] M. Roth and R. Peikert. Flow visualization for turbomachinery design. Proceedings of Seventh Annual IEEE Visualization '96, pages 381–384. doi: 10.1109/VISUAL.1996.568137.

[136] R.C. Strawn, J. Ahmad, and D.N. Kenwright. Computer visualization of vortex wake systems. AIAA journal, 37(4):511–512, 1999.

[137] Yves Dubief and Franck Delcayre. On coherent-vortex identification in turbulence. Journal of Turbulence, 1(00):1–22, 2000. ISSN 14685248. doi: 10.1088/1468-5248/1/1/011.

[138] G. Haller. An objective definition of a vortex. Journal of Fluid Mechanics, 525:1–26, February 2005. ISSN 0022-1120. doi: 10.1017/S0022112004002526.

[139] Ming Jiang, R. Machiraju, and D. Thompson. Detection and Visualization of Vortices. In The visualization handbook, pages 295–309. Academic Press, 2005.

[140] Václav Kolář. Vortex identification: New requirements and limitations. International Journal of Heat and Fluid Flow, 28(4):638–652, August 2007. ISSN 0142727X. doi: 10.1016/j.ijheatfluidflow.2007.03.004.

[141] H. F. Hawkins and D. T. Rubsam. Hurricane Hilda, 1964 II. Mon. Wea. Rev., 96:617–636, 1968.

[142] I G Currie. Fundamental mechanics of fluids. Mechanical engineering. Marcel Dekker, 2003. ISBN 9780824708863.

[143] T. Motzkin. Sur quelques propriétés caractéristiques des ensembles bornés non convexes. Atti Accad. Naz. Lincei Rend. Cl. Sci. Fis. Mat. Natur., 21:773–779, 1935.

[144] A Vincent and M Meneguzzi. The satial structure and statistical properties of homogeneous turbulence. Journal of Fluid Mechanics, 225:1–20, 1991. doi: 10.1017/S0022112091001957.

[145] Javier Jiménez, P. Moin, R. Moser, and L. Keefe. Ejection mechanisms in the sublayer of a turbulent channel. Physics of Fluids, 31(6):1311–1313, 1988. doi: 10.1063/1.866721.

[146] Y Yeh and HZ Cummins. LOCALIZED FLUID FLOW MEASUREMENTS WITH AN He Ne LASER SPECTROMETER. Applied Physics Letters, 4(10):176–178, 1964. doi: 10.1063/1.1753925.

[147] J. W. Foreman, E. W. George, and R. D. Lewis. Measurement of Localized Flow Velocities in Gases With a Laser Doppler Flowmeter. Applied Physics Letters, 7(4):77, 1965. ISSN 00036951. doi: 10.1063/1.1754319.

[148] JW Foreman, EW George, and RD Lewis. ERRATA: Measurement of Localized Flow Velocities in Gases with a Laser Doppler Flowmeter. Applied Physics Letters, 7(8):228–228, 1965.

[149] C. Truesdell. Two Measures of Vorticity. J. Rational Mech. Anal., 2:173–217, 1953.

[150] D. J. Tritton. Physical Fluid Dynamics. Oxford, England: Clarendon Press, 2nd edition, 1989.

[151] R Betchov. An inequality concerning the production of vorticity in isotropic turbulence. Journal of Fluid Mechanics, 1(05):497–504, 1956. doi: 10.1017/S0022112056000317.

[152] Wm. T. Ashurst, A. R. Kerstein, R. M. Kerr, and C. H. Gibson. Alignment of vorticity and scalar gradient with strain rate in simulated Navier–Stokes turbulence. Physics of Fluids, 30 (8):2343, 1987. ISSN 00319171. doi: 10.1063/1.866513.

[153] Martin Roth and Ronald Peikert. A Higher-Order Method For Finding Vortex Core Lines 1 Introduction. October, pages 143–150, 1998.

[154] W. P. Graebel. Advanced Fluid Mechanics. Academic Press / Elsevier, 2007.

[155] R Gilmore, Jean-Marc Ginoux, Timothy Jones, C Letellier, and U S Freitas. Connecting curves for dynamical systems. Journal of Physics A: Mathematical and Theoretical, 43(25):255101, June 2010. ISSN 1751-8113. doi: 10.1088/1751-8113/43/25/255101.

[156] E. A. Coddington and N. Levinson. Theory of Ordinary Differential Equations. New York: McGraw-Hill, 1995.

[157] JC Sprott. Some simple chaotic flows. Physical Review E, 50(2):647–650, 1994.

[158] Piotr Zgliczynski. Computer assisted proof of chaos in the Rossler equations and in the Henon map. Nonlinearity, 243(10):242–252, 1997.

[159] Warwick Tucker. A rigorous ODE solver and Smale's 14th problem. Foundations of Computational Mathematics, 2(1):53–117, 2002. doi: 10.1007/s102080010018.

[160] H Broer and F Takens. Dynamical Systems and Chaos. Applied Mathematical Sciences. Springer, 2010. ISBN 9781441968692.

[161] D Mackenzie and American Mathematical Society. A New Twist in Knot Theory. Number v. 7 in What's Happening in the Mathermatical Sciences. American Mathematical Society, 2009. ISBN 9780821844786.

[162] Edward N. Lorenz. Irregularity: a fundamental property of the atmosphere. Tellus A, 36A(2): 98–110, March 1984. ISSN 02806495. doi: 10.1111/j.1600-0870.1984.tb00230.x.

[163] OE Rossler. An equation for hyperchaos. Physics Letters A, 71(2-3):155–157, 1979.

[164] R. Thomas. Deterministic chaos seen in terms of feedback circuits: analysis, synthesis, 'labyrinth chaos'. Int. J. Bifurcation Chaos, 9:1889–1905, 1999.

[165] M Momeni, I Kourakis, M Moslehi-Fard, and P K Shukla. A Van der Pol–Mathieu equation for the dynamics of dust grain charge in dusty plasmas. Journal of Physics A: Mathematical and Theoretical, 40(24):F473–F481, June 2007. ISSN 1751-8113. doi: 10.1088/1751-8113/40/24/F06.

[166] Robert L. Merlino. Experimental Investigations of Dusty Plasmas. AIP Conference Proceedings, 799:3–11, 2005. ISSN 0094243X. doi: 10.1063/1.2134567.

[167] Yan Feng, J. Goree, and Bin Liu. Evolution of Shear-Induced Melting in a Dusty Plasma. Physical Review Letters, 104(16):1–4, April 2010. ISSN 0031-9007. doi: 10.1103/PhysRevLett.104.165003.

[168] Peter Hartmann, Angela Douglass, Jorge Reyes, Lorin Matthews, Truell Hyde, Anikó Kovács, and Zoltán Donkó. Crystallization Dynamics of a Single Layer Complex Plasma. Physical Review Letters, 105(11):1–4, September 2010. ISSN 0031-9007. doi: 10.1103/PhysRevLett.105.115004.

[169] Peter Hartmann, Máté Sándor, Anikó Kovács, and Zoltán Donkó. Static and dynamic shear viscosity of a single-layer complex plasma. Physical Review E, 84(1):1–6, July 2011. ISSN 1539-3755. doi: 10.1103/PhysRevE.84.016404.

[170] I. Langmuir, C. G. Found, and A. F. Detmer. No Tit. Science, 60:392–394, 1924.

[171] L. Spitzer Jr. The Dynamics of the Interstellar Medium. I. Local Equilibrium. The Astrophysical Journal, 93:369, 1941.

[172] Frank Verheest. Dusty plasmas in application to astrophysics. Plasma physics and controlled fusion, 41:A445, 1999.

[173] B A SMITH, L SODERBLOM, R BATSON, P BRIDGES, J INGE, H MASURSKY, E SHOEMAKER, R BEEBE, J BOYCE, G BRIGGS, A BUNKER, S A COLLINS, C J HANSEN, T V JOHNSON, J L MITCHELL, R J TERRILE, A F COOK, J CUZZI, J B POLLACK, G E DANIELSON, A P INGERSOLL, M E DAVIES, G E HUNT, D MORRISON, T OWEN, C SAGAN, J VEVERKA, R STROM, and V E SUOMI. A NEW LOOK AT THE SATURN SYSTEM - THE VOYAGER-2 IMAGES. SCIENCE, 215(4532):504–537, 1982. ISSN 0036-8075. doi: 10.1126/science.215.4532.504.

[174] C.K. Goertz and G. Morfill. A Model for the Formation of Spokes in Saturn's Ring. Icarus, 53(2):219–229, February 1983. ISSN 00191035. doi: 10.1016/0019-1035(83)90143-4.

[175] Mihály Horányi. Carged Dust Dynamics In The Solar System. Annual Review of Astronomy and Astrophysics, 34(1):383–418, September 1996. ISSN 0066-4146. doi: 10.1146/annurev.astro.34.1.383.

[176] J.-E. Wahlund, M. André, a.I.E. Eriksson, M. Lundberg, M.W. Morooka, M. Shafiq, T.F. Averkamp, D.a. Gurnett, G.B. Hospodarsky, and W.S. Kurth. Detection of dusty plasma near the E-ring of Saturn. Planetary and Space Science, 57(14-15):1795–1806, December 2009. ISSN 00320633. doi: 10.1016/j.pss.2009.03.011.

[177] G. S. Selwyn. In situ laser diagnostic studies of plasma-generated particulate contamination. Journal of Vacuum Science & Technology A: Vacuum, Surfaces, and Films, 7(4):2758, July 1989. ISSN 07342101. doi: 10.1116/1.576175.

[178] S.~M. Collins, D.~A. Brown, J.~F. O'Hanlon, and R.~N. Carlile. Postplasma particle dynamics in a Gaseous Electronics Conference RF Reference Cell. Journal of Vacuum Science Technology, 13:2950–2953, November 1995.

[179] K. Narihara, K. Toi, Y. Hamada, K. Yamauchi, K. Adachi, I. Yamada, KN Sato, K. Kawahata, A. Nishizawa, S. Ohdachi, and Others. Observation of dust particles by a laser scattering method in the JIPPT-IIU tokamak. Nuclear fusion, 37:1177, 1997.

[180] J. Winter. Dust: A new challenge in nuclear fusion research? Physics of Plasmas, 7(10):3862, 2000. ISSN 1070664X. doi: 10.1063/1.1288911.

[181] RL Merlino. Dusty plasmas in the laboratory, industry, and space. Physics Today, July:32–38, 2004.

[182] M. Rapp and F.-J. Lübken. Polar mesosphere summer echoes (PMSE): review of observations and current understanding. Atmospheric Chemistry and Physics Discussions, 4(4):4777–4876, August 2004. ISSN 1680-7375. doi: 10.5194/acpd-4-4777-2004.

[183] P M Bellan. Fundamentals of Plasma Physics. Cambridge University Press, 2008. ISBN 9780521528009.

[184] J Castro, P McQuillen, H Gao, and T C Killian. The role of collisions and strong coupling in ultracold plasmas. Journal of Physics: Conference Series, 194(1):012065, November 2009. ISSN 1742-6596. doi: 10.1088/1742-6596/194/1/012065.

[185] Peter Mansbach and James Keck. Monte Carlo trajectory calculations of atomic excitation and ionization by thermal electrons. Physical Review, 181(1):275, 1969.

[186] F. Stumpers. Balth. van der Pol's Work on Nonlinear Circuits. Circuit Theory, IRE Transactions on, 7(4):366–367, 1960.

[187] B. van der Pol. A theory of the amplitude of free and forced triode vibrations. Radio Review, 1:701–710,754–762, 1920.

[188] Bodil Branner and J.H. Hubbard. The iteration of cubic polynomials Part I: The global topology of parameter space. Acta mathematica, 160(1):143–206, July 1988. ISSN 0001-5962. doi: 10.1007/BF02392275.

[189] John Milnor. Remarks on iterated cubic maps. Experimental Mathematics, 1(5), 1992.

[190] J.A.C. Gallas. Dissecting shrimps: results for some one-dimensional physical models. Physica A: Statistical Mechanics and its Applications, 202(1-2):196–223, 1994.

[191] R Mackay. Some Flesh on the Skeleton: the Bifurcation Structure of Bimodal Maps. Physica D: Nonlinear Phenomena, 27(3):412–422, August 1987. ISSN 01672789. doi: 10.1016/0167-2789(87)90040-6.

[192] S. Fraser and R. Kapral. Analysis of flow hysteresis by a one-dimensional map. Physical Review A, 25(6):3223, 1982.

[193] R Gilmore. Lie groups, physics, and geometry: an introduction for physicists, engineers and chemists. Cambridge University Press, 2008. ISBN 9780521884006.

[194] Cristian Bonatto and Jason Gallas. Periodicity Hub and Nested Spirals in the Phase Diagram of a Simple Resistive Circuit. Physical Review Letters, 101(5):2–5, August 2008. ISSN 0031-9007. doi: 10.1103/PhysRevLett.101.054101.

[195] Jason a. C. Gallas. The Structure of Infinite Periodic and Chaotic Hub Cascades in Phase Diagrams of Simple Autonomous Flows. International Journal of Bifurcation and Chaos, 20 (02):197, 2010. ISSN 0218-1274. doi: 10.1142/S0218127410025636.

[196] Gonzalo M. Ramírez-Ávila and Jason a.C. Gallas. How similar is the performance of the cubic and the piecewise-linear circuits of Chua? Physics Letters A, 375(2):143–148, December 2010. ISSN 03759601. doi: 10.1016/j.physleta.2010.10.046.

[197] Joana Freire and Jason Gallas. Non-Shilnikov cascades of spikes and hubs in a semiconductor laser with optoelectronic feedback. Physical Review E, 82(3):3–6, September 2010. ISSN 1539-3755. doi: 10.1103/PhysRevE.82.037202.

[198] Roberto Barrio, Fernando Blesa, Sergio Serrano, and Andrey Shilnikov. Global organization of spiral structures in bi-parameter space of dissipative systems with Shilnikov saddle-foci. Physical Review E, 2011.

[199] A Shilnikov and Leonid Shilnikov. Symbolic dynamics and spiral structures due to the saddle-focus bifurcations. J. Bifurcations and Chaos, pages 1–19, 2011.

[200] Renato Vitolo, Paul Glendinning, and Jason Gallas. Global structure of periodicity hubs in Lyapunov phase diagrams of dissipative flows. Physical Review E, 84(1):1–7, July 2011. ISSN 1539-3755. doi: 10.1103/PhysRevE.84.016216.

[201] Ja Gallas. Structure of the parameter space of the Hénon map. Physical review letters, 70 (18):2714–2717, May 1993. ISSN 1079-7114.

[202] Philip Holmes. Bifurcation sequences in horseshoe maps: infinitely many routes to chaos. Physics Letters A, 104(6):299–302, 1984.

[203] JAC Gallas. Units: remarkable points in dynamical systems. Physica A: Statistical Mechanics and its Applications, 1995.

[204] R Gilmore. Catastrophe theory for scientists and engineers. Dover books on advanced mathematics. Dover Publications, 1993. ISBN 9780486675398.

[205] J. Eidson, S. Flynn, C. Holm, D. Weeks, and RF Fox. Elementary explanation of boundary shading in chaotic-attractor plots for the Feigenbaum map and the circle map. Physical Review A, 33(4):2809, 1986.

[206] E Ott. Chaos in dynamical systems. Cambridge University Press, 2002. ISBN 9780521010849.

[207] R.V. Jensen and C.R. Myers. Images of the critical points of nonlinear maps. Physical Review A, 32(2):1222–1224, 1985.

[208] Krzysztof Stefanski. Universality of Succession of Periodic Windows in Families of 1-D Maps. Open Systems & Information Dynamics, 6(3):309–324, 1999. doi: 10.1023/A:1009666421987.

[209] C Grebogi, E Ott, and J.~A. Yorke. Crises, sudden changes in chaotic attractors, and transient chaos. Physica D Nonlinear Phenomena, 7:181–200, May 1983. doi: 10.1016/0167-2789(83)90126-4.

[210] A. N. SHARKOVSKI. COEXISTENCE OF CYCLES OF A CONTINUOUS MAP OF THE LINE INTO ITSELF (Engl. Translation). International Journal of Bifurcation and Chaos (IJBC), 5(5):1263–1273, 1995. doi: 10.1142/S0218127495000934.

[211] Clewley RH, Sherwood WE, LaMar MD, and Guckenheimer JM. PyDSTool, a software environment for dynamical systems modeling, 2007.

[212] Eusebius J. Doedel and Bart E. Oldeman. AUTO-07P : CONTINUATION AND BIFURCATION SOFTWARE FOR ORDINARY DIFFERENTIAL EQUATIONS. September 2009.

[213] David M. Goldberg, Timothy D. Jones, Fiona Hoyle, Randall R. Rojas, Michael S. Vogeley, and Michael R. Blanton. The Mass Function of Void Galaxies in the Sloan Digital Sky Survey Data Release 2. The Astrophysical Journal, 621(2):643–650, March 2005. ISSN 0004-637X. doi: 10.1086/427679.

[214] BA Huberman and J. Rudnick. Scaling behavior of chaotic flows. Physical review letters, 45(3):154–156, 1980.

[215] H Kantz and P Grassberger. Repellers, semi-attractors, and long-lived chaotic transients. Physica D: Nonlinear Phenomena, 17(1):75–86, 1985.

[216] W Gropp, E Lusk, and R Thakur. Using MPI-2: advanced features of the message-passing interface. Scientific and engineering computation. MIT Press, 1999.

[217] Kais Al-Naimee, Francesco Marino, Marzena Ciszak, Riccardo Meucci, and F Tito Arecchi. Chaotic spiking and incomplete homoclinic scenarios in semiconductor lasers with optoelectronic feedback. New Journal of Physics, 11(7):073022, July 2009. ISSN 1367-2630. doi: 10.1088/1367-2630/11/7/073022.

[218] E B Saff and A D Snider. Fundamentals of complex analysis for mathematics, science, and engineering. Prentice Hall, 1993. ISBN 9780133274615.